

ABSTRACT

Title of Document:

CERAMIC AND COMPOSITE ANODES
FOR HYDROCARBON-FUELED
INTERMEDIATE TEMPERATURE SOLID
OXIDE FUEL CELLS.

Colin M. Gore, Doctor of Philosophy, 2014

Directed By:

Professor Eric D. Wachsman, Director of
University of Maryland Energy Research Center
and William L. Crantz Centennial Chair in
Energy Research, Department of Materials
Science

The operation of solid oxide fuel cells (SOFCs) using hydrocarbon fuels at temperatures from 500-650°C has been studied in this dissertation, with a focus on tailoring the fuel electrode (anode) to overcome challenges at these lower operating temperatures.

The parameter space for SOFC operation on hydrogen and hydrocarbon fuels is calculated using thermodynamic methods to find equilibrium conditions. The interrelation between parameters that determine cell efficiency and stability, such as the Nernst open circuit voltage, fuel utilization, and tendency to form solid carbon as a reaction product are explored. Methane fueling is found to have a more consistent voltage than hydrogen at high fuel utilizations at temperatures below 650 °C, which

correlates with increased theoretical efficiency. Reformed methane and jet fuel compositions that prevent carbon deposition are identified.

SOFCS with nickel - gadolinia-doped ceria (GDC) cermet anodes are fabricated and studied using hydrogen and reformed hydrocarbon fuels to determine the kinetic limitations to SOFC operation at 650 °C and below. Operating SOFCs on reformed hydrocarbons gives comparable performance to using hydrogen as a fuel, with as little as a 5% decrease in maximum power density (MPD). Stable performance of 220 mW/cm² while fueling with reformed jet fuel at 550 °C is observed.

Porous ceramic anodes fabricated from GDC are developed to prevent the mechanical damage caused by volume changes of Ni metal in conventional, randomly-mixed cermet anodes. The mechanical properties of the porous ceramics are extensively characterized, and the electrical properties of the scaffold anode are measured after infiltrating with metals. The porous ceramics attain strengths of >100 MPa, and have similar conductance to Ni-GDC cermet anodes but with ~70% less metal. SOFCs using these anodes have a MPD within 15% of cermet anode cells in H₂, but show stable operation at 120 mW/cm² at 600 °C on methane for >72 hours while cermet anodes are destroyed by solid carbon formation.

A mixed-conducting, single-phase material based on BaCeO₃ was developed for possible use as a metal-free anode. The stability of the material in CO₂ was improved through Zr and Nb doping on the B-site.

CERAMIC AND COMPOSITE ANODES FOR HYDROCARBON-FUELED
INTERMEDIATE TEMPERATURE SOLID OXIDE FUEL CELLS

By

Colin M. Gore

Dissertation submitted to the Faculty of the Graduate School of the
University of Maryland, College Park, in partial fulfillment
of the requirements for the degree of
Doctor of Philosophy
2014

Advisory Committee:

Professor Eric Wachsman, Chair
Professor Lingbing Hu
Professor Isabel Lloyd
Professor Chunsheng Wang
Professor Bryan Eichhorn, Dean's Representative

© Copyright by
Colin M. Gore
2014

Dedication

To my family, for their everlasting support.

Acknowledgements

First and foremost, I would like to thank my advisor Dr. Wachsman for giving me the opportunity to grow as a scientist and engineer in his research group. His guidance and constructive criticism were instrumental in shaping me as a researcher and in preparing the work presented in this dissertation. Dr. Wachsman's endless drive and ambition make him an admirable role model.

The support of Redox Power Systems, LLC has kept my work funded and will be giving me a unique opportunity to put my doctoral research into practice at a startup company focused on making energy generation cleaner and more affordable. Conversations with their CTO Dr. Bryan Blackburn have helped me focus on issues that are critical to scalable performance of SOFCs. I look forward to working with their team starting in January of 2015.

I would like to acknowledge the Metropolitan Washington Chapter of the ARCS Foundation for partial fellowship support for the past 3 years. Their philanthropic group provided me not only with funding, but also with a local network of contacts and acquaintances. In particular I must give my gratitude to Mary Snitch at Lockheed Martin for being my ARCS ambassador for all these years.

I would also like to recognize my coworkers that assisted me with research activities, especially Ashley Lidie Ruth, Kang Taek Lee, and Hee Sung Yoon who joined me in nucleating our research group at UMD after a move from University of Florida and undertaking the monumental task of setting up and moving laboratories... twice. Dr. Karen Gaskell has been incredibly helpful in opening up the world of surface science to

me, and her work ethic at the SAC is humbling. Larry Lai and Dr. Chiou at NISP lab sharpened the electron microscopy skills I learned at Lehigh, which I sincerely appreciate after operating the SEM for 200+ hours in the past 5 years. John Abrahams and the rest of the FabLab crew have been endlessly kind and helpful in assisting with materials characterization as well. I am also grateful for the contributions of the undergraduate students who assisted me with preparation of materials and carrying out testing, especially Luis Correa, Harmanpreet Singh, Matt Reilly, Josh White, Eric Chen, and Teresa Wierzbicki. It has been rewarding to help some of them find jobs and graduate positions in return for their diligence in their lab work on top of class commitments.

Though their contribution is more tangential, I'd like to thank my teammates on the Gamera Human-Powered Helicopter project. They gave me an incentive to stay at peak physical fitness to pilot and power their novel craft, which I found kept me more mentally astute as well. Earning a world record for their team has been one of the proudest achievements of my life. It was a project that also broadened my appreciation for the impact of modern materials on some *very alternative* energy technology.

Finally, on a more personal note, I thank my family for love and support throughout the whole process of earning my PhD. They have all contributed to my personality and well being in their own ways. Though my father passed away before I started this journey through graduate school, it was the curiosity and skepticism he encouraged in me that have helped me get to where I am today. I know he would have been proud and thrilled by this accomplishment.

Table of Contents

Acknowledgements	iii
Table of Contents	v
List of Tables.....	viii
List of Figures	ix
Chapter 1: The Motivation for Developing Hydrocarbon-Fueled Solid Oxide Fuel Cells.....	1
1.1 The Present Need for Solid Oxide Fuel Cells.....	1
1.2 Organization of Dissertation.....	4
Chapter 2: Background and Experimental Procedures.....	6
2.1 Fundamentals of SOFC Operation.....	6
2.1.1 Device Structure and Operation.....	6
2.1.2 Voltage Losses due to Cell Polarizations and Electronic Leakage.....	7
2.1.3 SOFC Efficiency	8
2.1.4 SOFC Anode Material Requirements and Typical Materials	9
2.2 SOFC Material Synthesis and Device Fabrication	11
2.2.1 Solid State Synthesis of Oxides	11
2.2.2 Nitrate Infiltration	11
2.2.3 Tape Casting	12
2.3 Materials Characterization	13
2.3.1 Archimedes Method	13
2.3.2 Scanning Electron Microscopy (SEM)	14
2.3.3 Energy Dispersive X-Ray Spectroscopy (EDS)	14
2.3.4 Three-Point Bend Testing	14
2.4 Electrochemical Characterization of Material and SOFCs.....	15
2.4.1 Potentiostat/Galvanostat Measurements	15
2.4.2 Electrochemical Impedance Spectroscopy (EIS)	16
Chapter 3: Thermodynamic Calculations for Hydrocarbon Fuelling of SOFCs	17
3.1.1 Calculation Methods	18
3.2 The Effect of Hydrogen vs. Hydrocarbon Fueling on Cell Potential	21
3.2.1 Open Circuit Conditions	21
3.2.2 Trends in Nernst Potential vs. Fuel Utilization.....	22
3.3 Formation of Solid Carbon from Hydrocarbons in SOFC Anodes	27
3.3.1 Overcoming Solid Carbon Deposition through External Reforming	30
3.3.2 Specific Examples of Effluent Gas from External Reformers	32
3.3.3 Reforming Exclusively Within the SOFC Anode.....	34
3.4 Conclusions.....	35
Chapter 4: Operation of SOFCs on Reformed Liquid Fuels and Natural Gas	37
4.1 Introduction.....	37
4.2 Experimental:.....	39
4.2.1 Cell fabrication.....	39
4.2.2 Cell Characterization	39

4.3 Results.....	41
4.3.1 The Effect of Fuel Utilization on Performance Using H ₂ as a Fuel.....	41
4.3.2 SOFC Operation on Steam-Reformed Methane	45
4.3.3 Operation on Reformed JP5 Jet Fuel	49
4.4 Discussion:.....	53
4.4.1 Electrochemical Performance	53
4.4.2 Comparison of Observed Results to Thermodynamic Calculations	55
4.5 Conclusions:.....	57
Chapter 5: Development of Porous Ceramic Anode Supports.....	59
5.1 Introduction.....	59
5.2 Experimental	63
5.2.1 Anode Support Fabrication	63
5.3 Characterization	64
5 . 3 . 1 Microstructure Measurement.....	64
5 . 3 . 2 Mechanical Properties Measurement	65
5 . 3 . 3 Electrical Measurements.....	65
5 . 4 Thermodynamic Calculations	66
5.5 Results and Discussion	66
5.5.1 Mechanical Strength vs. Porosity	66
5.5.2 Infiltrated Electronic Conductor/Catalyst	72
5.5.3 Calculated Reoxidation during SOFC Operation	77
5.6 Conclusions.....	78
Chapter 6: Performance of Ceramic Anode Supported SOFCs	80
6.1 Introduction:.....	80
6.2 Experimental:.....	85
6.2.1 Fabrication	85
6.2.2 Cell Characterization	87
6.2.3 Thermodynamic Equilibrium Calculations.....	89
6.3 Results & Discussion:.....	90
6.3.1 Microstructure	90
6.3.2 Electrochemical Impedance	93
6.3.3 Galvanic Sweeps	97
6.3.4 Long term stability while utilizing CH ₄	100
6.4 Conclusions:.....	106
Chapter 7: Development of Mixed Conducting Barium Cerate Ceramics for Metal-Free Anodes.....	107
7.1 Introduction.....	107
7.2 Experimental	109
7.2.1 Preparation, Phase, and Microstructure Studies of BaCe1-(x+y)ZrxNbyO ₃ (x = 0.05, 0.1, 0.15, 0.2; y = 0.05, and 0.1).....	109
7.2.2 AC Impedance Characterizations.	110
7.2.3 Thermogravimetric Measurements.	110
7.3 Results.....	111
7.3.1 PXRD Analysis.....	111
7.3.2 AC Impedance Analysis:	114
7.3.3 SEM Analyses.....	117

7.3.4 Elemental analysis by EDS and XPS.....	127
7.4 Discussion.....	129
7.5 Conclusions.....	134
Chapter 8: Conclusions	135
8.1 Resulting Publications	137
Appendix A: Software and Programming Scripts Used for Thermodynamic Calculations	138
Appendix B: Example Recipes for Ceramic Slurries	141
Appendix C: Gas Chromatograph Calibration	142
Appendix D: Diagnosing SOFC Testing Artifacts	144
Appendix E: Determining Pt Electrode Contributions to Electrochemical Impedance Spectroscopy Measurements of Material Properties	146
Appendix F: Correcting Peak Overlaps in BaCeO ₃ XPS Spectra	148
Bibliography.....	154

List of Tables

Table 2.1: Suppliers of Commercial Materials Used.....	11
Table 3.1: Predominant intermediate reactions in methane utilization.....	19
Table 3.2: Effluent Composition of methane and JP5 external reformers.....	33
Table 4.1: Composition (mol fraction) of the model reformates used in this study	41
Table 4.2: Effect of fuel utilization and flowrate on the properties of a H ₂ fueled SOFC 42	
Table 4.3: Effect of fuel composition and operating temperature on the performance of and SOFC fueled by hydrogen and reformed methane at 650 °C.....	48
Table 4.4: Summary of the electrochemical performance of SOFCs using H ₂ vs. reformed JP5 jet fuel.....	50
Table 5.1: Measured physical parameters for each set of porous material using 5μm PMMA pore former.	68
Table 5.2: Electronic Conductance of Reduced, Infiltrated GDC Electrodes at Room Temperature	76
Table 5.3: Equilibrium PO ₂ below which the metals stay reduced compared to the calculated equivalent PO ₂ of SOFC fuels at 50% and 99% fuel utilization (FU).....	78
Table 6.1: Volume fraction of Ni, GDC, and pore phases and GDC electrolyte thickness in reduced anodes.....	91
Table 6.2: Measured diameter of pores and Ni particles in each anode and calculated TPB density.....	93
Table 6.3: Model circuit component parameters determined by ZSimpWin 3.5 fittings. .	95
Table 6.4: Real components of ASR for cells using each anode support at OCV (from EIS) and under polarization (from galvanic sweeps).....	97
Table 6.5: EDS analysis of deposited carbon on anodes after long-term CH ₄ fueling....	103
Table 7.1 Physical and chemical properties of BaCe _{1-x-y} Zr _x Nb _y O ₃ (x = 0.05; 0.1; 0.15, 0.2; y = 0.05, and 0.1).	126
Table 7.2 Expected Stoichiometry vs. Composition Obtained from EDS and.....	128

List of Figures

Figure 1.1: Specific power vs. power density of energy generation technologies [1].....	1
Figure 1.2: Schematics of (a) proton-conducting and (b) solid oxide fuel cells.....	2
Figure 2.1: Schematic Plot of Voltage Response of and SOFC vs. Current Density, With Individual Contributions to Polarization Labeled, from [2]	8
Figure 2.2: Thermogravimetric profile of $\text{Ni}(\text{NO}_3)_2 \cdot 6\text{H}_2\text{O}$, from [30]	12
Figure 2.3: Schematic of the Tape Casting Process, Including Preparation Steps, from [31]	13
Figure 2.4: Schematic of a 3-point bend test, from [34]	15
Figure 2.5 Example EIS response presented as a) Nyquist and b) Bode plots, from [35].	16
Figure 3.1: Ellingham diagram for oxides of interest. From D.R. Gaskell [39]	19
Figure 3.2: Theoretical OCV using H_2 or CH_4 fuel fed with 3 mol% H_2O	22
Figure 3.3: a) typically the effect of fuel utilization is ignored [4] b) Gas consumption at the anode is taken into account by Ivers-Tiffée and Virkar [2] by assuming a linear contribution versus fuel utilization	23
Figure 3.4: Theoretical Voltage Drop vs. Fuel Utilization for CH_4 and H_2 at 400 °C and 800 °C. Inset table give the magnitude of the Nernst voltage decrease at 95% fuel utilization.	26
Figure 3.5: 2D (top) and 3D (bottom) contour maps of the OCV vs. Fuel Utilization for H_2 (left) and CH_4 (right) fuel. Note that the temperature scales are reversed to show the surface of the 3D contour plot more effectively.....	26
Figure 3.6: Temperature Dependence of Coking Reactions a) Methane cracking b) CO disproportionation c) CO reduction	27
Figure 3.7: Ternary plot of C(s) formation at 650 °C. Red points shows C:H:O ratio of methane (1:4:0) and octane (4:9:0), and green points show fully oxidized C:H:O ratio for methane (1:4:4) and octane (4:9:17).	29
Figure 3.8: Carbon formation vs. fuel utilization for methane fueling	29
Figure 3.9: The effect of SR, CDR, and POX on carbon deposition and OCV at 800, 550, and 300 °C	31
Figure 3.10: The effect of steam concentration in methane on carbon formation	32
Figure 3.11: Nernst OCV of SOFCs operating on hydrogen and reformed methane	33
Figure 3.12: Surface oxygen availability per CH_4 required to prevent carbon deposition	35
Figure 4.1: Cross-section of untested SOFC before reducing of NiO to Ni metal	38
Figure 4.2: a) schematic and b) photograph of the SOFC characterization system used in this study	41
Figure 4.3: The effect of H_2 fuel utilization (FU) and flowrate on the a) current-voltage and b) power density characteristics of an SOFC at 650 °C	44
Figure 4.4: EIS response at H_2 fuel utilization from 0-75% at cell voltages at 650 °C at a) OCV, b) 0.7 V, c) 0.6 V, and d) 0.5 V.....	44
Figure 4.5: The effect of H_2 fuel utilization and flowrate on a) the ASRs and MPD and b) the OCV and temperature of an SOFC at 650 °C	45
Figure 4.6: Current-voltage response and power density of SOFCs operating on reformed methane fuel at a) 650 °C and b) 600 °C	47

Figure 4.7: EIS response at OCV and under polarization for different fuel compositions (H ₂ , 0% Slip, 100% Slip) and potentials from OCV to 0.4 V at 650 °C and 600 °C.	47
a) Comparison of the three fueling conditions at OCV at 650 °C. b) H ₂ at 650 °C,	
c) H ₂ at 600 °C, d) 0% slip at 650 °C, e) 0% slip at 600 °C, f) 100% slip at 650 °C,	
f) 100% slip at 600 °C.....	47
Figure 4.8: SEM micrographs of SOFC after operation on reformed CH ₄ (100% slip) for 100 hours. Bottom surface and electrolyte interface show no carbon deposition.....	48
Figure 4.9: (a) SEM micrograph of cross-sectional view of the SOFC after testing. I–V plots of SOFCs operating on H ₂ (circle) and JP5 reformate (triangle) at (b) 650 °C, (c) 600 °C, (d) 550 °C. (e) OCV (left Y-axis) and total ASR (right Y-axis) of SOFCs operating on H ₂ (circle) and JP5 reformate (triangle) as a function of temperature.	49
Figure 4.10: Nyquist plots (symbols) and fitting results (line) of SOFCs operating on H ₂ (circle) and JP5 model reformate (triangle) at (a) 650 °C, (b) 600 °C, (c) 550 °C. (d) Equivalent circuit for fitting. (e) Total (square), electrode (circle), and Ohmic (triangle) ASRs of SOFCs operating on H ₂ (filled symbols) and JP5 reformate (open symbols) as a function of temperature. (f) Arrhenius plots of electrode ASR of SOFCs operating on H ₂ (circle) and JP5 reformate (triangle) at low (open symbols) and high (filled symbols) frequency regimes.....	51
Figure 4.11: (a) Long -term stability test (500 h at 550 °C) of the SOFC operating on JP5 reformate using a potentiostatic mode with an applied voltage of 0.392 V at which MPD was achieved. (b) I–V and (c) Nyquist plots before (filled triangle) and after (open triangle) the long term stability test (d) SEM image of cross sectional view of the SOFC after the 500 h long term test. (e) EDS spectra of the area marked in (d) as a dotted rectangle.	52
Figure 4.12: Deviation between the theoretical Nernst voltage and the measured OCV for SOFCs using reformed hydrocarbon fuels: JP5 vs. H ₂ (left) and reformed CH ₄ vs. H ₂ (right).....	56
Figure 4.13: Calculated vs. observed OCV for H ₂ and CH ₄ fuel when a YSZ electrolyte is used, from Lin & Barnett [51].....	57
Figure 5.1: Electronic conductivity of pure Cu, Ni, and Co metal vs. T from 0 – 650 °C. Data for Ni and Cu from [20] and data for Co from [61]. Solid lines are a guide to the eye.	60
Figure 5.2: Ionic conductivity at 650 °C vs. flexural strength at room temperature of fluorite oxides GDC and YSZ. Data from [1, 63, 69].....	62
Figure 5.3: Final pore volume percent in sintered samples vs. volume percent of 5μm PMMA pore former added to ceramic powder. Dashed line represents a 1:1 relationship. Solid lines are linear fits, with the slope and intercept for each given in the inset equations.....	67
Figure 5.4: a) Flexural Strength vs. Porosity of GDC10, YSZ8 and YSZ3 with 5μm PMMA pore former. Solid lines show the fitting of Eq. 4, and Table 5.1 gives empirical fitting parameter, n, determined for each material. b) Inset graph shows the relationship between n and the slopes in Figure 5.3.	69
Figure 5.5: a) GDC scaffold strength vs. PMMA pore former diameter for a 50 vol% PMMA addition. Dashed black lines are a guide to the eye. Red dotted line	

indicated sintered GDC grain size. b) Resulting pore diameter (black) and volume percent porosity (blue) for a 50 vol% addition of different diameter PMMA. Dashed line shows a 1:1 $d_{\text{pore}}:d_{\text{PMMA}}$ relationship. c) Difference between pore and PMMA diameters (blue) and ratio between pore size and starting PMMA diameter (red).....	70
Figure 5.6: Unfired GDC powder and resulting sintered scaffolds with 50 vol% PMMA added. a) GDC milled with 1.7 μm PMMA, b) GDC milled with 5 μm PMMA, c) pressed and sintered GDC using $d_{\text{PMMA}} = 1.7 \mu\text{m}$, d) pressed and sintered GDC using $d_{\text{PMMA}} = 5 \mu\text{m}$, e) pressed and sintered GDC using $d_{\text{PMMA}} = 29 \mu\text{m}$, f) tapecast and sintered GDC using $d_{\text{PMMA}} = 5 \mu\text{m}$. The relationship between ceramic-coated PMMA spheres in a and b and the resulting pores in c and d are outlined and emphasized with arrows.....	71
Figure 5.7: Effect of processing on porous GDC scaffold strength using 5 μm PMMA pore former. Tapecasting (green) gives higher strength than uniaxial pressing (red). Orange triangle represents literature value from Atkinson [66].	72
Figure 5.8: Volume percent of metal (Ni, Cu, or Co) in a porous GDC scaffold after each deposition and decomposition of the metal nitrate solution. Solid lines are a guide to the eye.....	73
Figure 5.9: SEM micrographs of the metal-infiltrated GDC scaffolds after 4, 8, and 12 infiltrations showing the distribution of metal (darker deposits) on the GDC (lighter scaffold) after reduction in 10% H ₂ /N ₂ . Scale bar is 10 μm	75
Figure 5.10: a) Specific conductance of infiltrated GDC vs. volume percent loading of metal. b) Ratio of measured conductance to intrinsic conductivity for each metal vs. volume percent metal. Solid lines are a guide to the eye.	77
Figure 6.1: Volume percent Ni metal loading after each Ni nitrate infiltration into the porous GDC anode scaffold for GS54. Lines are to guide the eye.....	91
Figure 6.2. Comparative micrographs of SOFCs fabricated with identical GDC electrolytes and LSCF-GDC cathodes, but different anode supports: a) 50:50 vol% Ni-GDC <u>cermet</u> anode b) Ni infiltrated scaffold from 50:50 vol% GDC-PMMA (<u>GS40</u>) c) Ni infiltrated scaffold from 40:60 vol% GDC-PMMA (<u>GS54</u>).	92
Figure 6.3: Backscattering electron images (2kx magnification) of reduced anode supports for a) cermet anode and b) GS54, a GDC (light phase) scaffold infiltrated with 11.7 vol% Ni (dark gray phase). Black areas are open porosity.....	93
Figure 6.4: Fittings of charge transfer and mass transfer constant phase element (CPE) components to EIS data collected at 650 °C in H ₂ for a) cermet, b) GS40 and c) GS54 anodes. Charge transfer fits are blue, mass transfer fits are red, total fits lines are black, and the experimental data points are marked.....	94
Figure 6.5. a) Nyquist and b) Bode plots of EIS response of the scaffold anode cells compared to the cermet anode cell at 650 °C in H ₂ . Data points are marked with circles, and the solid lines represent the results of the model circuit fitting.	95
Figure 6.6. Ohmic, charge transfer, and mass transfer components of ASR for each cell, from EIS fittings at 650°C in H ₂	97
Figure 6.7. Galvanic sweep plots comparing SOFCs with the 3 anode types at 650 °C in H ₂ : a) Voltage vs. current density b) Power density vs. current density c) Tafel plot of the electrode overpotentials and extrapolated Tafel slope used to find exchange current density.....	99

Figure 6.8: Exchange current density from galvanic sweep vs. charge transfer resistance determined by EIS fittings. Black circles are experimental data points, and the dashed line is the expected slope from the first principles relationship between R_{CT} and i_0	100
Figure 6.9. a) Long-term performance of cells after switching from 30 ccm H ₂ to 15 ccm CH ₄ fuel. b) Current-voltage relationships for H ₂ (solid lines) and CH ₄ (dashed lines) fueling.....	101
Figure 6.10. SEM micrograph and EDS spectrum of a) cermet anode with severe coking [>70 mol% C(s)] after 24 hours and b) GS54 anode with no carbon deposition after fueling with methane for 72 hours.....	103
Figure 6.11. Calculated mol% of C(s) in the reaction products of CH ₄ in the anode vs. temperature and available O ²⁻ ions at the reaction site. The grayscale gradient is in 10 mol% increments. Red and green points show the calculated O ²⁻ :CH ₄ ratio in the cermet and GS54 anode atmosphere, respectively.....	104
Figure 6.12. Schematic of the microstructural factors contributing to enhanced oxygen spillover in the GDC scaffold anode: a) smaller Ni particles have shorter surface diffusion paths for oxygen ions b) there is no continuity of ionic conductor from the electrolyte to many Ni surfaces of the cermet anode c) every Ni particle in the scaffold anodes is constrained on a continuous network of ionic conductor, providing a pathway for oxygen ions to be replenished from the electrolyte.....	105
Figure 7.1 Powder XRD diffractograms and lattice parameters of as-prepared (a) BaCe _{0.9} Zr _{0.05} Nb _{0.05} O ₃ (I), (b) BaCe _{0.8} Zr _{0.1} Nb _{0.1} O ₃ (II), (c) BaCe _{0.75} Zr _{0.15} Nb _{0.1} O ₃ (III) and (d) BaCe _{0.7} Zr _{0.2} Nb _{0.1} O ₃ (IV) sintered at 1450-1600 °C in air. For clarity, only the reflections used to calculate the lattice parameters are indexed. The formation of a single-phase orthorhombic perovskite-type phase was observed for all the investigated compounds.....	112
Figure 7.2 (a) Selected area powder XRD diffractograms showing the (040), (224), and (040) reflections and calculated tolerance factor of BaCe _{0.9} Zr _{0.05} Nb _{0.05} O ₃ (I), BaCe _{0.8} Zr _{0.1} Nb _{0.1} O ₃ (II), BaCe _{0.75} Zr _{0.15} Nb _{0.1} O ₃ (III), BaCe _{0.7} Zr _{0.2} Nb _{0.1} O ₃ (IV), and BaCeO ₃ sintered at 1600 °C. (b) Variation of lattice volume as a function of B-site average ionic radius. A reference point for BaCeO ₃ lattice volume by neutron diffraction (□) is given based on measurements by Jacobson et al ²⁸ . The linear shift in the diffraction peaks and decrease in cell volume versus B-site radius support Zr and Nb -cosubstitution for Ce in the perovskite-type structure, confirming solid solution. Note that most error bars are smaller than symbols.....	113
Figure 7.3 Typical AC impedance plots obtained at 400 °C in air, using Pt electrodes, for BaCe _{0.9} Zr _{0.05} Nb _{0.05} O ₃ , BaCe _{0.8} Zr _{0.1} Nb _{0.1} O ₃ , BaCe _{0.75} Zr _{0.15} Nb _{0.1} O ₃ , and BaCe _{0.7} Zr _{0.2} Nb _{0.1} O ₃ (a) sintered 1500 °C and (b) sintered 1600 °C. An example of intercepts used for bulk and total resistance measurements and the characteristic peak frequency are indicated for BaCe _{0.8} Zr _{0.1} Nb _{0.1} O ₃ (red circles) in each plot.	118
Figure 7.4 Typical AC impedance plots obtained at 700 °C in air, using Pt electrodes, for BaCe _{0.9} Zr _{0.05} Nb _{0.05} O ₃ , BaCe _{0.8} Zr _{0.1} Nb _{0.1} O ₃ , BaCe _{0.75} Zr _{0.15} Nb _{0.1} O ₃ , and BaCe _{0.7} Zr _{0.2} Nb _{0.1} O ₃ (a) sintered 1500 °C and (b) sintered 1600 °C. An example of intercepts used for bulk and total resistance measurements and the characteristic peak frequency are indicated for BaCe _{0.8} Zr _{0.1} Nb _{0.1} O ₃ (red circles) in each plot.	119

Figure 7.5 Grain-boundary real capacitance vs. temperature increases with sintering temperature, following an improvement in densification for all compositions. Nanofarad-range capacitances suggest grain boundary conduction processes.....	120
Figure 7.6 Arrhenius plots for (a) bulk, (b) grain-boundary, and (c) total conductivity of BaCe _{0.9} Zr _{0.05} Nb _{0.05} O ₃ , BaCe _{0.8} Zr _{0.1} Nb _{0.1} O ₃ , BaCe _{0.75} Zr _{0.15} Nb _{0.1} O ₃ , and BaCe _{0.7} Zr _{0.2} Nb _{0.1} O ₃ sintered at 1450°C, 1500 °C, 1550 °C and 1600 °C.	123
Figure 7.7 Variation of conductivity (■) and bulk activation energy (○) as a function of average B-site ionic radius for BaCe _{0.9} Zr _{0.05} Nb _{0.05} O ₃ (I), BaCe _{0.8} Zr _{0.1} Nb _{0.1} O ₃ (II), BaCe _{0.75} Zr _{0.15} Nb _{0.1} O ₃ (III), BaCe _{0.7} Zr _{0.2} Nb _{0.1} O ₃ (IV).	124
Figure 7.8 Representative 10 kx SEM images of BaCe _{0.9} Zr _{0.05} Nb _{0.05} O ₃ (I), BaCe _{0.8} Zr _{0.1} Nb _{0.1} O ₃ (II), BaCe _{0.75} Zr _{0.15} Nb _{0.1} O ₃ (III) and BaCe _{0.7} Zr _{0.2} Nb _{0.1} O ₃ (IV) sintered 1450, 1500, 1550 and 1600 °C.....	125
Figure 7.9 Expected stoichiometry of A and B site cations vs. bulk composition by EDS and surface composition by XPS.....	128
Figure 7.10 In-situ TGA analysis showing the chemical stability of BaCe _{0.9} Zr _{0.05} Nb _{0.05} O ₃ , BaCe _{0.8} Zr _{0.1} Nb _{0.1} O ₃ , BaCe _{0.75} Zr _{0.15} Nb _{0.1} O ₃ and BaCe _{0.7} Zr _{0.2} Nb _{0.1} O ₃ in 30 % CO ₂ balanced by N ₂ atmosphere. For comparison, chemical stability of benchmark high temperature proton conductor Y-doped BaCeO ₃ is included. Carbonates are driven off >1040°C, in agreement with thermodynamic equilibrium calculations [10].	132
Figure 7.11 In-situ TGA plot showing the enhanced stability in CO ₂ of the Nb enriched surface of BaCe _{0.9} Zr _{0.05} Nb _{0.05} O ₃ (I) powder (dashed line, SSA = 0.56 m ² /g) compared to a powder of its bulk composition (solid line, SSA =0.51 m ² /g).	133

Chapter 1: The Motivation for Developing Hydrocarbon-Fueled Solid Oxide Fuel Cells

1.1 The Present Need for Solid Oxide Fuel Cells

The energy landscape in the United States and abroad is transitioning in response to several driving forces. Increased concern about anthropogenic climate change has motivated governments and industry to more closely monitor and curtail energy-related CO₂ emissions. At the same time, the world population is continually increasing and as more nations develop more advanced infrastructure, more power generation is required to meet the increasing demand. As it stands, much of that demand is met using coal or natural gas fired power plants, which release large amounts of CO₂, SOx, NOx, and particulates, polluting the atmosphere. There is a burgeoning need for alternative energy generation technologies that can more efficiently and cleanly utilize available hydrocarbon fuels such as natural gas, gasoline, and coal. Fuel cells are a promising technology to play that role due to their high energy and power density (Figure 1.1).

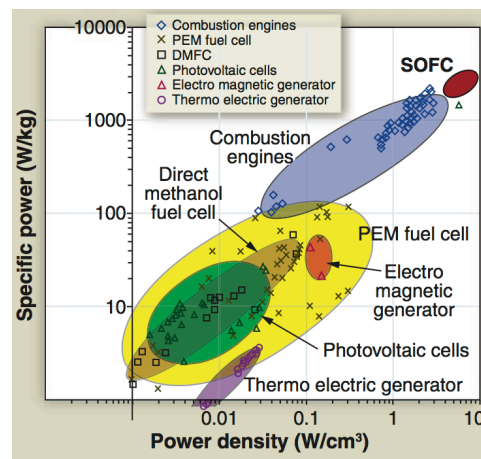


Figure 1.1: Specific power vs. power density of energy generation technologies [1]

Fuel cells are electrochemical devices used to convert the chemical energy in a fuel directly into electrical energy in an external circuit [1]. They are not limited by Carnot or Otto efficiency like internal combustion engines (ICEs) that have <30% electrical efficiency in a generator. Fuel cells have demonstrated >60% electrical efficiency for primary power applications and >90% overall efficiency in combined heat and power applications [2, 3]. Their lack of moving components makes them inherently quiet, making them ideal for military and residential applications alike, and prevents energy losses from friction.

Fuel cell technologies are typically classified by the type of electrolyte they use. Though fuel cells with liquid electrolytes such as alkaline and molten carbonate fuel cells have been demonstrated with success, their slow response times, corrosion issues, and restriction to stationary applications limit them to niche markets [4]. Fuel cells with all solid-state components are poised for broader penetration into transportation and stationary power markets. Solid-state fuel cells fall into two categories, defined by their electrolyte materials. Proton-conducting fuel cells (Figure 1.2a) use a membrane that conducts protons from the fuel at the anode to the cathode where they combine with O₂ in air to form water.

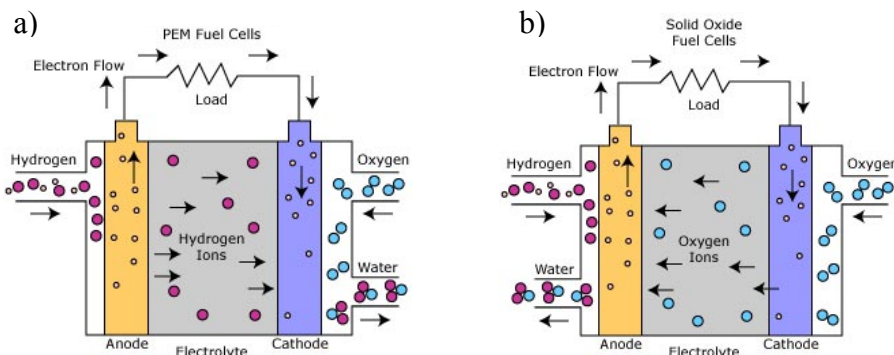


Figure 1.2: Schematics of (a) proton-conducting and (b) solid oxide fuel cells

Polymeric proton-exchange membranes (PEMs), such as Nafion are used as electrolytes at relatively low temperatures, <100 °C since they must remain hydrated to function. Promising results have also been demonstrated more recently with ceramic high-temperature proton conducting (HTPC) membranes based on doped barium cerate between 400 °C to 700 °C [5-8]. Both of these membrane types currently require very pure hydrogen as a fuel. PEM cells suffer from CO poisoning of their Pt-based catalysts, and BaCeO₃-based HTPC cells degrade in CO₂ to form insulating BaCO₃ and CeO₂ [5, 9, 10]. Currently most H₂ is produced from natural gas, so both CO and CO₂ are initially present in high concentrations and the gas requires extensive cleaning to be used with these cells. Fuel cells that can run directly on the available hydrocarbon fuels that H₂ is separated from will be cheaper and more efficient.

Solid oxide fuel cells (SOFCs), on the other hand, conduct oxygen ions from the cathode to the fuel at the anode (Figure 1.2b). This unique property allows them to be used with essentially any fuel that will oxidize, including natural gas, gasoline, biogas, etc. This fuel-flexibility makes SOFCs the most broadly useful variety of fuel cell because they can seamlessly integrate with the existing hydrocarbon infrastructure, as well as with future renewable fuels [11]. They are not dependent on the development of a hydrogen economy like PEM cells are. For decades, the primary limitation for SOFCs had been that the conventional electrolyte material, yttria-stabilized zirconia (YSZ), requires temperatures of ~800-1000 °C in order to operate with adequate power density. Ionic conductivity is thermally activated, so electrolyte conductivity decreases with decreasing temperature and overall cell resistance increases concurrently. Recent

advances in electrolyte materials and cell design have significantly lowered cell resistance, allowing operation temperatures of SOFCs to the 450-700 °C range [12-16]. Lower temperature decreases balance-of-plant (BOP) costs and inhibits the degradation of components that occurs at high operating temperatures. Gadolinia-doped ceria (GDC) and lanthanum-strontium gallate-magnesite (LSGM) have oxygen-ion conductivities of ~10 times that of YSZ, and erbium-stabilized bismuth oxide (ESB) has a conductivity of ~100 times that of YSZ, lowering electrolyte Ohmic resistance accordingly [1, 16, 17]. Also, since electrolytes have a higher Ohmic resistance than the electrodes, using thick anodes (100's of μm) to support thin electrolytes (10's of μm) has also helped lower overall cell resistance. These enabling advances in lower temperature SOFCs encourage focused development of complimentary electrodes that are ideal for the cooler operating temperatures. Development of new anodes for hydrocarbon fuels is a primary need since their mechanisms for catalysis and conductivity are highly temperature dependent.

1.2 Organization of Dissertation

The objective of this dissertation is to better understand the requirements of SOFCs operating at intermediate temperatures (500 – 650 °C) on hydrocarbon fuels. This work is organized into sections as follows. The background information on the principles of SOFC operation and the material synthesis, device fabrication, and characterization techniques are presented in Chapter 2. Original thermodynamic calculations of the parameter space for SOFC operation on hydrogen and hydrocarbon fuels are detailed in Chapter 3. Collected data for SOFC operation on reformed fuels is presented in Chapter 4 and compared to the calculated equilibrium values determined in Chapter 3. Development and characterization of a ceramic scaffold anode tailored to hydrocarbon

fueling is disseminated in Chapter 5, and test results from SOFCs using those anodes are explored in Chapter 6. The development of a single-phase anode material with mixed conduction for hydrocarbon fueled SOFCs is described in Chapter 7. Conclusions of this work and suggestions for future research are presented in Chapter 8.

Chapter 2: Background and Experimental Procedures

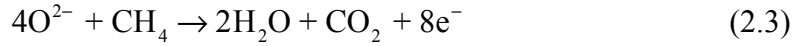
2.1 Fundamentals of SOFC Operation

2.1.1 Device Structure and Operation

SOFCS are composed of a cathode and anode separated by a solid, O²⁻ ion conducting electrolyte, as previously shown in Figure 1.2b. The cathode is the positive electrode at which oxygen in air is reduced to oxygen ions according to the reaction:



The ion-conducting electrolyte conducts these oxygen ions to the anode, the negative electrode where the ions combine with a fuel and release electrons according to the reactions for hydrogen and hydrocarbons (in this case CH₄), respectively:



Higher hydrocarbons will have different reactions depending on their C:H ratios. The electrolyte material is an electronic insulator, so the chemical potential between the low PO₂ reducing atmosphere in the fuel at the anode (PO_{2,fuel}) and the oxidizing atmosphere, typically air, at the cathode (PO_{2,air}) drives those electrons through an external circuit where they are then used to reduce oxygen, which completes the circuit.

The reversible open-circuit voltage (OCV) of the fuel cell is determined using the Nernst equation (Eq. 2.4), which is affected by the operating temperature (T) and the difference in oxygen partial pressure across the electrolyte. R is the universal gas constant and F is Faraday's constant.

$$OCV = \frac{RT}{4F} \ln\left(\frac{PO_{2,\text{air}}}{PO_{2,\text{fuel}}}\right) \quad (2.4)$$

2.1.2 Voltage Losses due to Cell Polarizations and Electronic Leakage

As the O²⁻ current density through an SOFC increases, several irreversible polarization mechanisms diminish the cell voltage from its OCV value. A schematic of the typical voltage response of a SOFC is given in Figure 2.1. The measured voltage during operation is a function of OCV as well as Ohmic (η_{Ohmic}), activation (η_{act}), and concentration (η_{conc}) polarizations associated with the electrolyte and electrodes.

$$E = OCV - \eta_{\text{Ohmic}} - \eta_{\text{act}} - \eta_{\text{conc}} \quad (2.5)$$

Ohmic polarization is the voltage drop determined by Ohms law from the sum of the resistances of the anode, cathode, and electrolyte. Typically, the electrolyte is the most resistive component of an SOFC by several orders of magnitude, so it dominates the Ohmic polarization. Activation polarization is caused by charge transfer limitations for oxygen reduction and fuel oxidation at low current density, but has less of an effect as the current density increases. At the high operating temperatures of SOFCs, activation polarization typically has minimal measurable influence, but it increases in magnitude as the operating temperature decreases. Concentration polarization is caused by mass transfer limitations at high current densities. The fuel or oxygen at the electrode-electrolyte interface becomes depleted faster than it can be replenished by diffusion, so the concentration of the species at the interface is diluted.

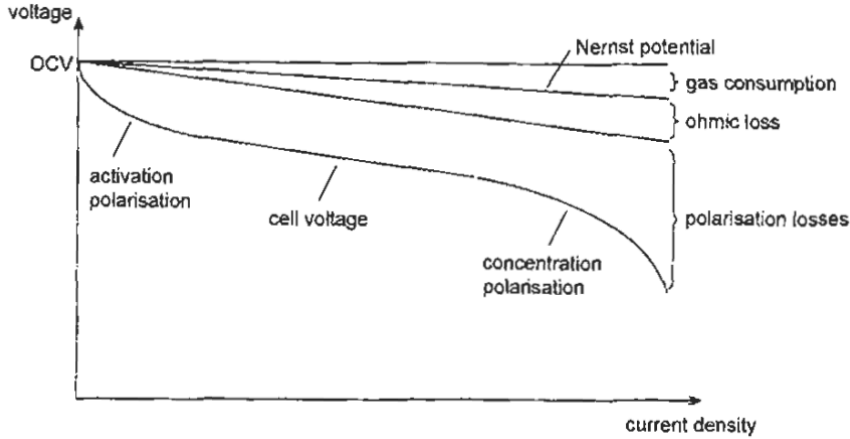


Figure 2.1: Schematic Plot of Voltage Response of an SOFC vs. Current Density, With Individual Contributions to Polarization Labeled, from [2]

The measured OCV will be lower than the expected Nernst OCV if the electrolyte materials has any electronic leakage. This is characterized by the electrolyte materials ionic transference number (t_i), which is the ratio of oxygen ionic conductivity to total electrical conductivity of all species in the material:

$$t_i = \frac{\sigma_i}{\sigma_{total}} \quad (2.6)$$

For materials such as YSZ, which are purely ionic conductors, $t_i = 1$. If $t_i < 1$, like it is in GDC, the electrolyte will exhibit a leakage current that diminishes the cell OCV compared to the theoretical value.

2.1.3 SOFC Efficiency

The overall free-energy conversion efficiency (ϵ_{total}) of an SOFC is given by the product of the voltage efficiency (ϵ_V), the Faradaic efficiency (ϵ_F), and the fuel utilization (U_f) of the cell.

$$\epsilon_{total} = \epsilon_V \cdot \epsilon_F \cdot U_f \quad (2.7)$$

The voltage efficiency accounts for irreversible losses in the cell and is dependent on the Nernst open circuit voltage of the cell and the operating voltage (V_{oper}) used during operation:

$$\epsilon_v = \frac{V_{oper}}{OCV_{Nernst}} \quad (2.8)$$

The faradaic efficiency takes into account the parasitic losses due to electronic leakage of an electrolyte with $t_i < 1$ or any gas crossover in the cell that lower measured OCV, and is given by:

$$\epsilon_f = \frac{OCV_{meas.}}{OCV_{Nernst}} \quad (2.9)$$

The fuel utilization is the fraction complete oxidation of the fuel that is achieved by the SOFC. The interplay between the fuel utilization and OCV parameters that determine cell efficiency is investigated in more detail in Chapter 3 of this work.

2.1.4 SOFC Anode Material Requirements and Typical Materials

Ideal SOFC anodes must be engineered to meet several key requirements at the desired operating temperature of the cell they are incorporated into [18]:

1. High electronic conductivity ($>1000 \text{ S/cm}^2$ for anode-supported cells)
2. Catalytic activity toward fuel oxidation
3. Adequate interconnected porosity for fuel diffusion to the active TPB ($\geq 30\%$)
4. Matching CTE with electrolyte material ($13.4 \cdot 10^{-6} \text{ K}^{-1}$ for GDC)
5. Adequate mechanical strength to support the electrolyte and cathode
6. Ionic conductivity to extend active TPB region
7. Long-term stability with adjacent components at elevated temperatures

To date, no single material fulfills all of these requirements simultaneously, so composites must be used. Nickel-ceramic composites (cermets) have been the industry standard for decades [19] ; Ni meets requirements 1-3, and the ceramic meets 4-7. Nickel has a very high electrical conductivity, $>10^6$ S/cm at 650 °C [20], so including >30 vol% Ni in the cermet provides a percolated electrically-conductive network in the anode to deliver electrons generated by fuel oxidation (Eqn. 5-6) at the TPB to a current collector. Rossmeisl and Bessler recently identified Ni, using DFT calculations, as the ideal metal for fuel oxidation catalysis due to the intermediate strength of its metal-oxygen bonds [21]. Using NiO as a starting material helps create adequate porosity in the cermet because it undergoes a 40.9% decrease in volume when reducing to Ni metal in the reducing fuel atmosphere, leaving interconnected pores behind [22]. This volume change is problematic when structural Ni is reoxidized or coarsens, however, because the electrodes and electrolyte are damaged by the induced strain. For this reason, among others, ceramic supports are developed and demonstrated in Chapters 5-6 that do not require Ni to be a structural component.

The ceramic component of the anode is generally the same material used in the electrolyte, ensuring a reasonable TEC match and ionic conductivity. Ceramic materials also have a greater compressive strength than metals at high temperature, and are less prone to coarsening. Mixed conducting ceramic materials are being developed for use in metal-free anodes for SOFCs as well [23-29]. The development of a barium cerate based material for this purpose is detailed in Chapter 7.

2.2 SOFC Material Synthesis and Device Fabrication

Where possible, commercial powders of SOFC materials were obtained to ensure consistency and repeatability of materials properties, device fabrication, and testing results. Commercial products used in this study are listed in Table 2.1.

Table 2.1: Suppliers of Commercial Materials Used

Material	Abbreviation	Supplier	Product Number	Notes
$\text{Ce}_{0.9}\text{Gd}_{0.1}\text{O}_{1.95}$	GDC	Rhodia	GDC10	nanopowder
$\text{Ce}_{0.9}\text{Gd}_{0.1}\text{O}_{1.95}$	GDC	Fuel Cell Materials	GDC10-TC	larger diameter
$(\text{ZrO}_2)_{0.92}(\text{Y}_2\text{O}_3)_{0.08}$	YSZ8	Tosoh	TZ-8Y	
$(\text{ZrO}_2)_{0.97}(\text{Y}_2\text{O}_3)_{0.03}$	YSZ3	Tosoh	TZ-3Y	nanopowder
$\text{La}_{0.4}\text{Sr}_{0.4}\text{Co}_{0.2}\text{Fe}_{0.8}\text{O}_3$	LSCF	Praxair	LSCF-6428	
Ni	Ni	Alfa Aesar	12359	>1 μm diameter
Ni	Ni	JT Baker	1313-99-1	<1 μm diameter

2.2.1 Solid State Synthesis of Oxides

Oxides developed for this study that are not available commercially are synthesized using the solid-state reaction (SSR) method. Appropriate amounts of metal oxides, metal nitrates, and metal carbonates are milled together in ethanol. The specific amounts of each constituent are calculated to yield an oxide with the desired final stoichiometry. The mixture is dried and subsequently calcined by heating to a temperature (generally >1000 °C) that yields a single phase from the mixed materials.

2.2.2 Nitrate Infiltration

In order to deposit metal in porous materials, a nitrate infiltration method is used. The desired metal nitrate is dissolved in water until a saturated concentration is reached. Triton X-100 surfactant (Dow) is added to the mixture to improve wetting of the solution on the substrate. The infiltrated material is heated to a temperature high enough to decompose the nitrate and crystalline water, leaving behind a metal oxide, then cooled. For Ni deposition from Ni nitrate hexahydrate, the required temperature is >300 °C, as

shown by the thermogravimetric plot in Figure 2.2. The process is repeated to achieve the desired metal loading in the sample.

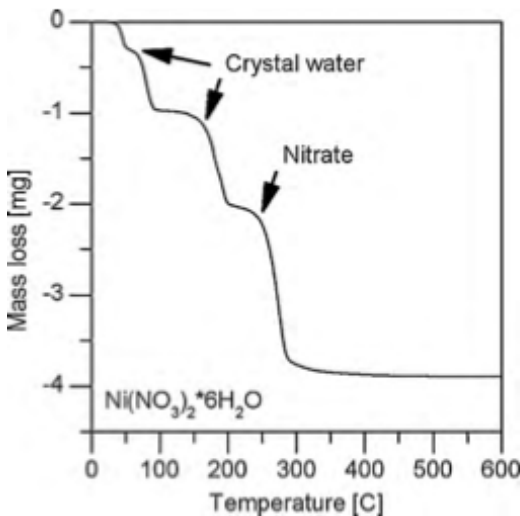


Figure 2.2: Thermogravimetric profile of $\text{Ni}(\text{NO}_3)_2 \cdot 6\text{H}_2\text{O}$, from [30]

2.2.3 Tape Casting

The anode and electrolyte layers for SOFCs used in this study are fabricated by tape casting, as depicted in the schematic in Figure 2.3. The ceramic powder and any pore former are milled together with dispersants and polymeric binders and plasticizers. The resulting slurry is ball milled for 1-3 days to disperse the particle and break up agglomerates. The slurry is then degassed in a vacuum chamber to remove any air bubbles that will create pinholes in the tape. The slurry is then cast using a doctor blade to define the film thickness on a moving carrier tape. The resulting film (or tape) of ceramic and polymer is then dried. Further processing of the tape can include lamination with other tapes to create a multilayer, or burnout of the polymer and sintering to make a porous or dense ceramic monolith.

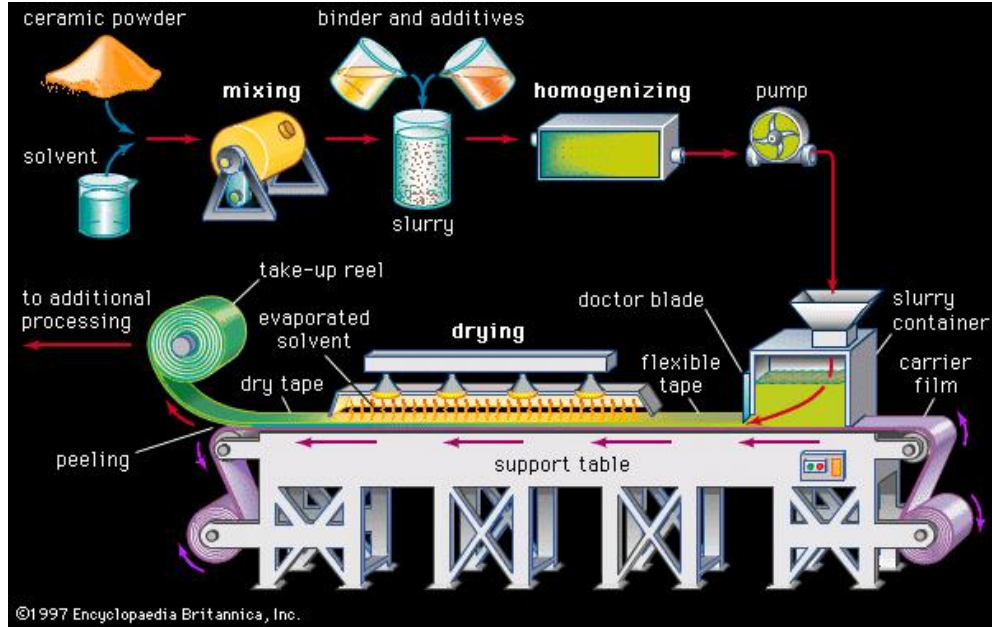


Figure 2.3: Schematic of the Tape Casting Process, Including Preparation Steps, from [31]

2.3 Materials Characterization

2.3.1 Archimedes Method

The density and porosity of ceramic monoliths are determined using Archimedes method. The dry sample weight (W_{Dry}) is measured and then the sample is submerged in water under a vacuum (~20 mTorr) to ensure that all the pores are filled with water. The saturated sample weight (W_{Sat}) and the weight while submerged under water (W_{Sub}) are then measured. The density of water is 1 g/cc, which simplifies the relevant equations. The porosity and density are computed using the relationships:

$$\text{Porosity \%} = \frac{W_{Sat} - W_{Dry}}{W_{Sat} - W_{Sub}} \quad (2.10)$$

$$\text{Density} = \frac{W_{Dry}}{W_{Sat} - W_{Sub}} \quad (2.11)$$

2.3.2 Scanning Electron Microscopy (SEM)

Microstructural properties of the anodes and multilayer SOFC devices fabricated in this study are investigated both qualitatively (absence of pores or cracks in dense electrolyte, etc.) and quantitatively (grain sizes, pore diameters, layer thicknesses) using SEM. A Hitachi SU-70 scanning electron microscope is used to collect the micrographs. For porous anode images, a long working distance of ~15mm is used to enhance the depth of field, since the intentionally introduced pores in the anodes are often \gg 1um deep. For greater phase contrast in other images, a shorter working distance is used with the detector in backscattering mode. Ceramic samples are carefully fractured to expose a fresh, roughly planar surface for imaging. Note that when ductile metal is supported on a brittle substrate, some elastic deformation may occur, so observed morphologies may be slightly altered. Quantification of microstructural details is performed in the software FIJI [32].

2.3.3 Energy Dispersive X-Ray Spectroscopy (EDS)

Compositional analysis of sample bulk is carried out by EDS using a Bruker XFlash silicon drift detector. For all materials studied, the X-ray sampling depth is $> 1\mu\text{m}$ [33]. An accelerating voltage of 15 kV is used to ensure good resolution of the K and L lines used for quantification by the Bruker ESPRIT software.

2.3.4 Three-Point Bend Testing

Mechanical testing is performed using 3-point bend tests (Figure 2.4) in a Tinius Olsen H25K-T benchtop universal testing machine at room temperature.

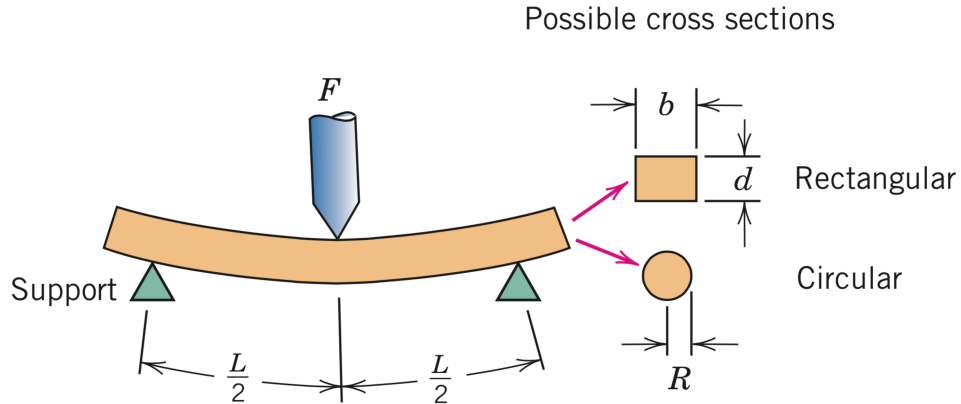


Figure 2.4: Schematic of a 3-point bend test, from [34]

Flexural strength (σ_f) is determined using Eq. 2.12, where F is force at fracture in Newtons, L is the spacing between the supports in mm, b is width of the sample, and d is its thickness.

$$\sigma_f = \frac{3FL}{2bd^2} \quad (2.12)$$

2.4 Electrochemical Characterization of Material and SOFCs

2.4.1 Potentiostat/Galvanostat Measurements

Galvanic sweeps are collected using a ParStat 2273 or Solartron 1470E. The resulting plots of voltage vs. current (see Figure 2.1) are used to determine the total area-specific resistance (ASR) and maximum power density (MPD) of the cells. Potentiostatic or galvanostatic tests are used to determine the stability of SOFC operation vs. time.

2.4.2 Electrochemical Impedance Spectroscopy (EIS)

The real and imaginary impedance response of SOFCs or single materials with Pt electrodes were collected using a Solartron 1425A or ParStat 2273 frequency response analyzer. Measurements were collected from 0.1 Hz to 0.1 MHz at 10 steps per decade. Bode plots and Nyquist plots (Figure 2.5) are used to deconvolute the individual contributions to total ASR. For SOFCs, these are Ohmic, activation, and concentration overpotentials, as previously mentioned. For single materials, the bulk and grain boundary resistivity is determined by EIS. Semicircles in Nyquist plots or peak in Bode plots related to each of these contributions are differentiated by their capacitance values and frequency range.

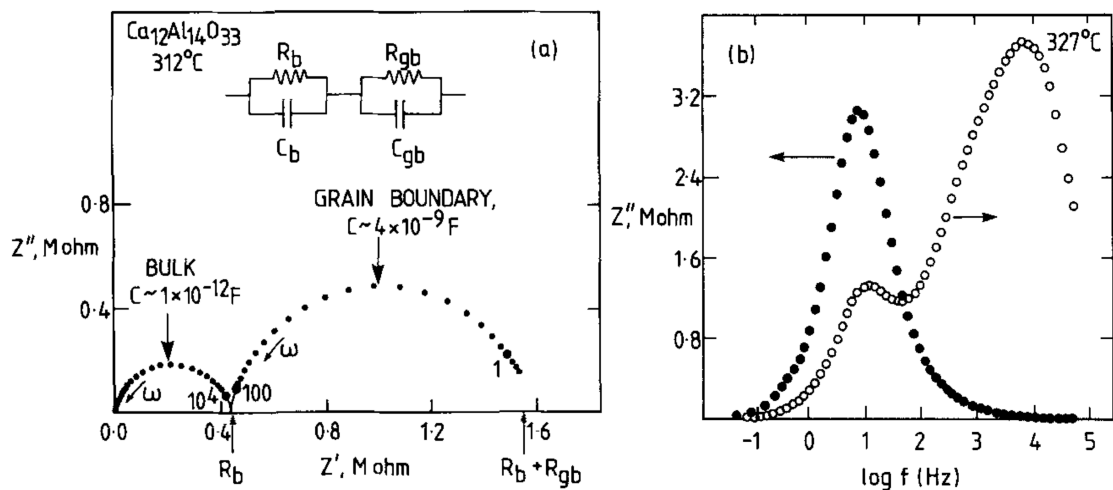


Figure 2.5 Example EIS response presented as a) Nyquist and b) Bode plots, from [35].

Chapter 3: Thermodynamic Calculations for Hydrocarbon Fuelling of SOFCs

Most SOFC studies to date that investigate hydrocarbon fueling focus on operating temperatures above 700 °C, primarily because zirconia-based electrolyte materials (i.e. YSZ, ScSZ) or thick electrolyte-supported cell geometries limit their cell operation to high temperatures to maintain acceptably low cell resistances. Utilizing natural gas and other hydrocarbons at lower temperatures, 500-650 °C introduces unique thermodynamic conditions that are not present at higher temperature due the change of several key reactions from spontaneous to non-spontaneous, and vice-versa, between 650-710 °C. As electrolytes and cathodes are improved and enable high power operation at lower temperatures, SOFC anodes will need to be tailored to operate effectively at these conditions.

In this chapter, thermodynamic calculations are used to describe the parameter space for the utilization of hydrogen, methane (the main component in natural gas) and jet fuel. Both internal and external reforming scenarios are described. Though the operating temperatures of interest are lower than conventional SOFC operating temperatures, they are still high enough that the gas phase is not kinetically limited, which justifies a thermodynamic study. The effect of parameters that determine efficiency (fuel composition, fuel utilization, and Nernst voltage) and tendency for carbon deposition is determined using thermodynamic calculations. The implications of these effects for SOFC operation are also discussed. Comparison of these calculations

with experimental data, in which kinetic limitations could be revealed, is conducted in Chapter 4.

3.1.1 Calculation Methods

The OCV of H₂-H₂O mixtures is relatively simple to calculate due to the single equilibrium reaction ($H_2 + O_2 \leftrightarrow H_2O$) with only 3 species that is used to determine the effective PO₂ at the anode. The equilibrium when using methane and other hydrocarbon fuels is more complex. With multiple species and several reactions possible, a system of multiple equations with multiple unknowns is required. The open-source thermodynamics and chemical kinetics software Cantera [36] is used in this study to calculate equilibrium molar concentrations in the anode atmosphere. The thermodynamic parameters used with Cantera are NASA polynomials from the GRI 3.0 mechanism for combustion of methane [37] developed by the Gas Research Institute at UC Berkeley, Stanford, and SRI. The Gibbs free energy of the reaction products of an initial fuel composition is minimized to find the equilibrium values using a non-stoichiometric method for enhanced computation speed [38]. Predominant reactions relevant to H₂ and CH₄ oxidation are listed in Table 3.1 for reference.

The equilibrium PO₂ determined by this method is used to calculate theoretical OCVs for different fueling conditions using the Nernst equation. It is also used to determine the tendency for metal in the anode to reoxidize during operation (presented in Chapter 5). An Ellingham diagram [39], shown in Figure 3.1, is used to determine equilibrium PO₂ of the metal-metal oxide equilibria of interest. The anode PO₂ must remain below this equilibrium PO₂ of the metal-metal oxide for the metal to remain as a base metal. The molar concentration of solid carbon in the calculated system equilibrium

indicates what conditions will cause problematic coking. Only temperatures and fuel compositions that yield zero solid carbon can be expected to have no deleterious effects from carbon deposition over time.

Table 3.1: Predominant intermediate reactions in methane utilization

	Reaction	$\Delta G^\circ @ 25^\circ C$ (kJ/mol)	$T_{\Delta G=0}$ (°C)	ΔG 650 °C	ΔG 700 °C	ΔG 710 °C
1	$CO + \frac{1}{2} O_2 \leftrightarrow CO_2$	-257.2	-270	-	-	-
2	$H_2 + \frac{1}{2} O_2 \leftrightarrow H_2O$	-228.6	-268	-	-	-
3	$CH_4 + 2O_2 \leftrightarrow CO_2 + 2H_2O$	-800.9	-119	-	-	-
4	$CH_4 + \frac{1}{2} O_2 \leftrightarrow CO + 2H_2$	-86.5	-63	-	-	-
5	$CH_4 \leftrightarrow 2H_2 + C(s)$	50.7	653	+	-	-
6	$CO + H_2O \leftrightarrow CO_2 + H_2$	-55.3	682	-	+	+
7	$CH_4 + H_2O \leftrightarrow CO + 3H_2$	142.1	687	+	-	-
8	$CH_4 + CO_2 \leftrightarrow 2CO + 2H_2$	170.7	690	+	-	-
9	$2CO \leftrightarrow CO_2 + C(s)$	-120.5	707	-	-	+
10	$CO + H_2 \leftrightarrow H_2O + C(s)$	-91.4	708	-	-	+

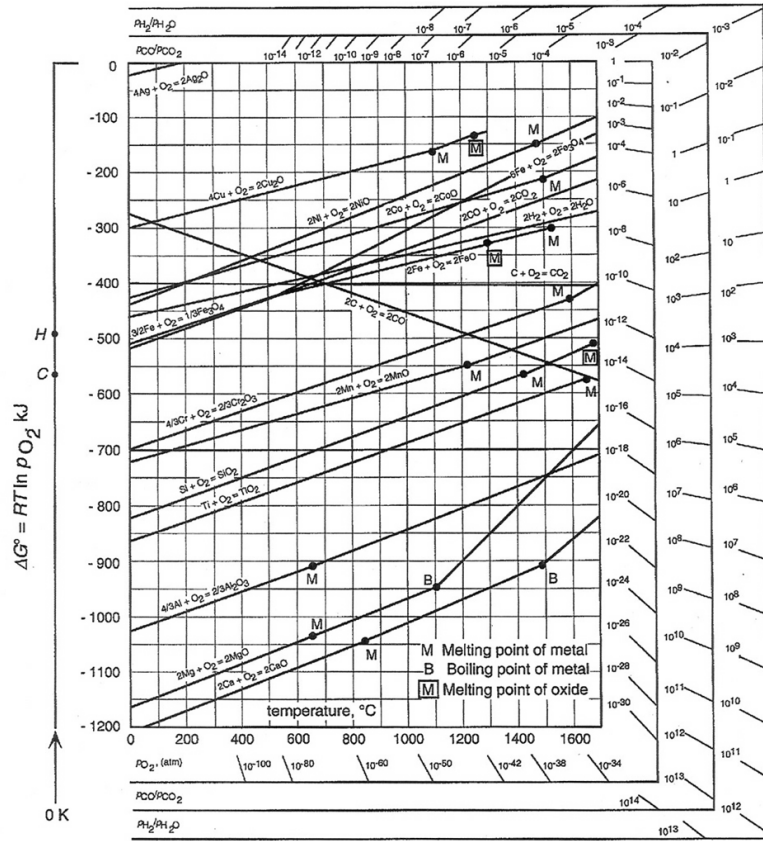


Figure 3.1: Ellingham diagram for oxides of interest. From D.R. Gaskell [39]

A SOFC must be able to achieve high fuel utilization efficiency and have high voltage efficiency to have good overall operation efficiency. The voltage efficiency can suffer at high fuel utilization, however, because the anode PO_2 increases as the fuel is oxidized, and the Nernst voltage subsequently decreases. Fuel utilization is modeled by adding an amount of oxygen to the fuel according to Eq. 1 the Faradaic O^{2-} current through the SOFC electrolyte.

$$F_{\text{o}^{2-}} = \frac{I}{zF} = \frac{I}{96,485 \frac{\text{C}}{\text{mol}} * 2} \quad [1]$$

The correlation between Faradaic current and fuel utilization is dependent on the fuel flowrate of the fuel and the geometry of the SOFC microstructure, so the calculations presented will simply be in terms of fuel utilization percentage. This is the fraction of oxygen ions added to the system through the SOFC electrolyte compared to the total number of oxygen ions required to completely oxidize all hydrogen and carbon species in the fuel to CO_2 and H_2O . Initial compositions of pure H_2 and pure CH_4 are humidified by bubbling through water to establish a starting PO_2 in the fuel, which is a standard practice in the operation of SOFCs. The vapor pressure of water at room temperature is approximately 0.03 atm, so the fuel feeds used in this study have 3 mol% water added to humidify pure fuels.

3.2 The Effect of Hydrogen vs. Hydrocarbon Fueling on Cell Potential

3.2.1 Open Circuit Conditions

A high open circuit voltage is necessary for high voltage and Faradaic efficiency of an SOFC. The theoretical voltage of an SOFC is found using the Nernst equation:

$$\text{OCV} = \frac{RT}{4F} \ln\left(\frac{0.2095}{\text{PO}_{2,\text{fuel}}}\right) \quad [2]$$

Since the cathode is exposed to a stream of excess air, its PO_2 is fixed at 0.2095 atm, which leaves operation temperature and anode PO_2 (highlighted in red) as the only free variables in determining the OCV of the SOFC. The theoretical OCV profiles versus temperature for methane and hydrogen in Figure 3.2 exhibit opposite trends as operating temperature lowers. This trend is due the different endothermic and exothermic properties of different chemical reactions in each fuel equilibrium, resulting in transitions in spontaneity of the reactions. H_2 fueling increases the achievable OCV as temperature lowers, but for CH_4 OCV decreases with decreasing temperature. Below 542 °C, the OCV using CH_4 is less than that of using H_2 , but the magnitude of the effect is small. At 200 °C, a temperature lower than any hydrocarbon fueled SOFC has ever been operated at, the OCV for CH_4 fueling is only 7.5% lower, so natural gas fueling of SOFCs at very low temperatures is possible without excessive thermodynamic limitations on the cell's OCV. Kinetic limitations on the oxidation of hydrocarbon fuels will be limiting at reduced temeratures before the thermodynamic differences become problematic.

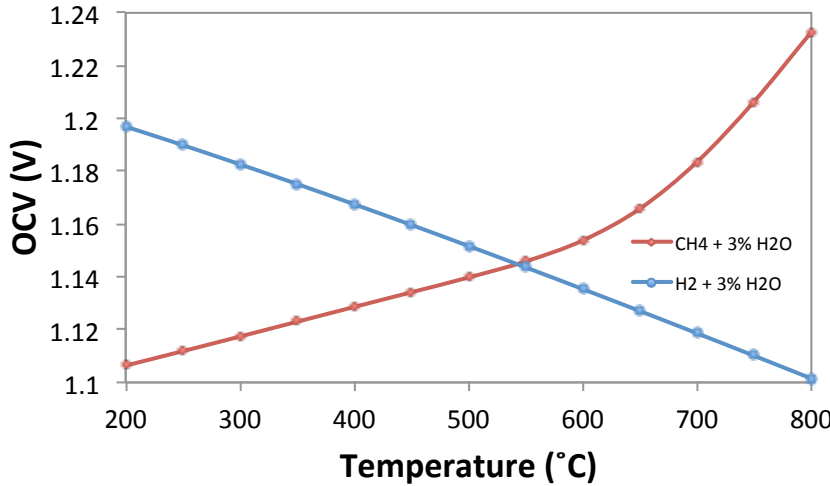


Figure 3.2: Theoretical OCV using H₂ or CH₄ fuel fed with 3 mol% H₂O

3.2.2 Trends in Nernst Potential vs. Fuel Utilization

The effect of fuel utilization is often overlooked in the interpretation of the current-voltage response of tested SOFCs. The canonical *Fuel Cell Handbook* [4] published by the US Department of Energy provides a typical example of this interpretation in Figure 3.3a. The total overpotential measured as the current density of the cell is attributed only to activation, Ohmic, and concentration polarization of the fuel cell itself. This interpretation ignores the change in anode atmosphere that occurs as the fuel is utilized (oxidized) and increases in effective PO₂, thereby decreasing the Nernst potential serving as the driving force. Ignoring this change in driving force may not lead to significant error when very low fuel utilizations (<5%) are used in typical laboratory tests on button cells, but it is critical to account for when scaling up SOFCs to the stack level where high fuel utilization is necessary for high efficiency.

Ivers-Tiffée and Virkar, in *High Temperature Solid Oxide Fuel Cells* [2], explicitly acknowledge this contribution of fuel utilization on the Nernst potential across the cell, as shown in Figure 3.3b in a model case for hydrogen fueling. The increasing partial pressure of the products dilutes the remaining reactants, causing a subsequent decrease in Nernst potential, which leads to the voltage loss labeled as “gas consumption” in the figure. In a sense, concentration polarization is caused by a similar fuel dilution, but is kinetically limited by fuel diffusion through the microstructure rather than by an equilibrium effect like overall fuel utilization is.

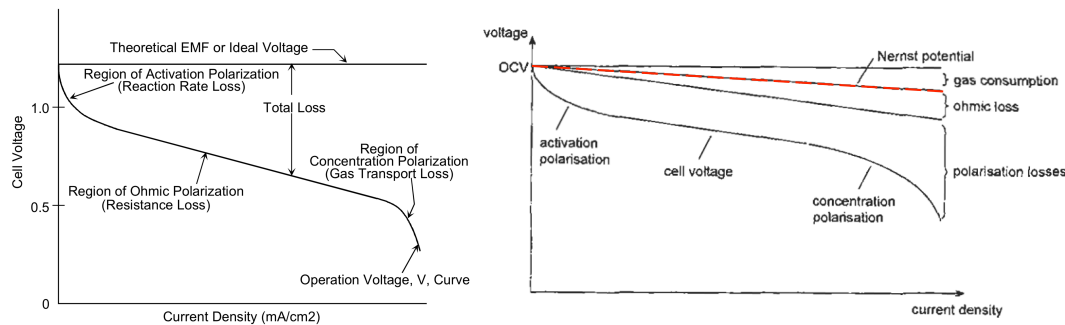


Figure 3.3: a) typically the effect of fuel utilization is ignored [4] b) Gas consumption at the anode is taken into account by Ivers-Tiffée and Virkar [2] by assuming a linear contribution versus fuel utilization

Since the voltage loss due to fuel utilization can have a meaningful impact on SOFC operation, the equilibrium effects have been calculated for conditions relevant to this study. The effect of fuel utilization on Nernst potential is a function of temperature and initial fuel composition, with the change in effective PO_2 of the fuel being the critical variable. Plots for hydrogen and methane fueling are presented and interpreted as follows.

The decrease in Nernst voltage as both CH_4 and H_2 are utilized at 400 °C and 800 °C, from 0% to 100% fuel utilization is plotted in Figure 3.4. An interesting effect that is

not immediately apparent from the OCV trend in Figure 3.2 is that lower temperature operation has the advantage of more consistent Nernst voltage as the fuel is oxidized at the anode of the SOFC. The voltage drop between OCV and 95% fuel utilization is lower at 400 °C than at 800 °C for both fuels, and CH₄ has the lowest voltage decrease overall at that temperature (see inset table). Furthermore, though the OCV trend observed in Figure 3.2 shows that the OCV decreases with temperature for CH₄ fueling, the cell voltage at fuel utilizations experienced in the SOFC is actually higher than that at higher temperature. Comparing 400 °C (solid lines) to 800°C operation (dotted lines), the lower operation temperature has a higher cell voltage for all fuel utilizations >35%. This indicates that under equilibrium conditions, lower operating temperatures using hydrocarbon fuels are desirable because the voltage profile through a SOFC stack will be more consistent.

Contour plots are presented in Figure 3.5 to convey the full parameter space of temperature, fuel utilization, and Nernst potential relationships at temperatures from 300 °C -1000 °C. The OCV plots in Figure 3.2 are equivalent to the trace of the 3D contour plots at 0% fuel utilization, and Figure 3.4 is composed of the traces of the 3D contour plots along 400 °C and 800 °C. Using the contour plots, the full complexity of the interplay between temperature, fuel utilization, and Nernst voltage can be visualized without creating hundreds of individual XY plots. The 2D contour plots are merely a plan view along the z-axis of the 3D plots to serve as an additional visual reference for the parameter space.

Several key relationships are observed in these contour plots. For hydrogen fueling, the relationships are straightforward because there is only one reaction

equilibrium to satisfy (Reaction 2 in Table 3.1), which is spontaneous ($\Delta G < 0$) over the entire temperature range of interest. The OCV, which is the Nernst voltage at 0% fuel utilization, linearly decreases with temperature as a result. The Nernst potential also decreases with fuel utilization, but it follows an S-curve rather than a direct linear relationship. This suggests that, when fueling with hydrogen, the shape of the theoretical gas consumption contribution in Figure 3.3b should match this profile, rather than the linear case that was presented by Ivers-Tiffée and Virkar. The exact shape of that contribution depends on temperature. Furthermore, the difference in Nernst voltage between OCV and high fuel utilization is consistently less as temperature decreases.

The case of CH₄ fueling is more complex because more reactions are involved in establishing the equilibrium PO₂ (Reactions 1-10 in Table 3.1). The OCV increases with temperature, matching the profile seen in Figure 3.2. The effect of fuel utilization on Nernst voltage is affected by the change in spontaneity (sign of ΔG) of Reaction 5-10 (Table 3.1) as temperature increases from 650 °C to 710 °C. The result is that a discontinuity in curvature is observed at $U_f \approx 25\%$ at 1000 °C (Figure 3.5) that extends to higher U_f at lower temperature. The point of discontinuity reaches $U_f = 50\%$ and disappears below 650 °C, leaving a continuous curve for the Nernst voltage profile vs. fuel utilization down to 400 °C. At low temperature, the Nernst voltage is even more stable vs. fuel utilization for CH₄ than for H₂, which suggests that methane fueling at these temperatures may enable more stable power output from a large-scale stack than hydrogen fueling does.

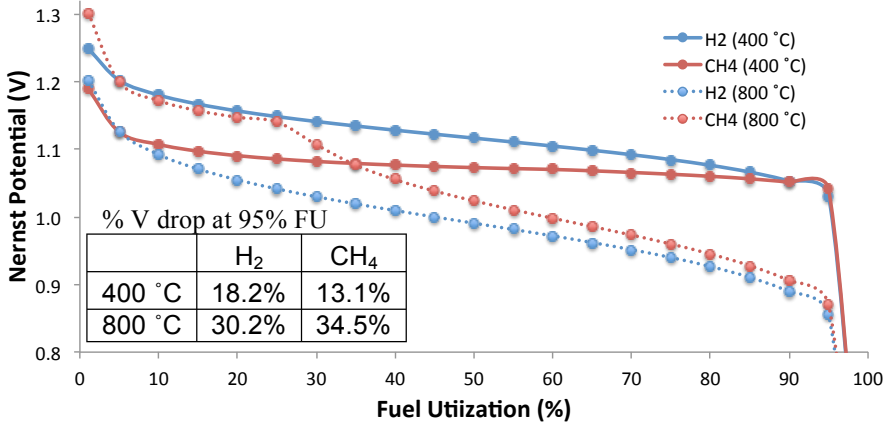


Figure 3.4: Theoretical Voltage Drop vs. Fuel Utilization for CH₄ and H₂ at 400 °C and 800 °C. Inset table give the magnitude of the Nernst voltage decrease at 95% fuel utilization.

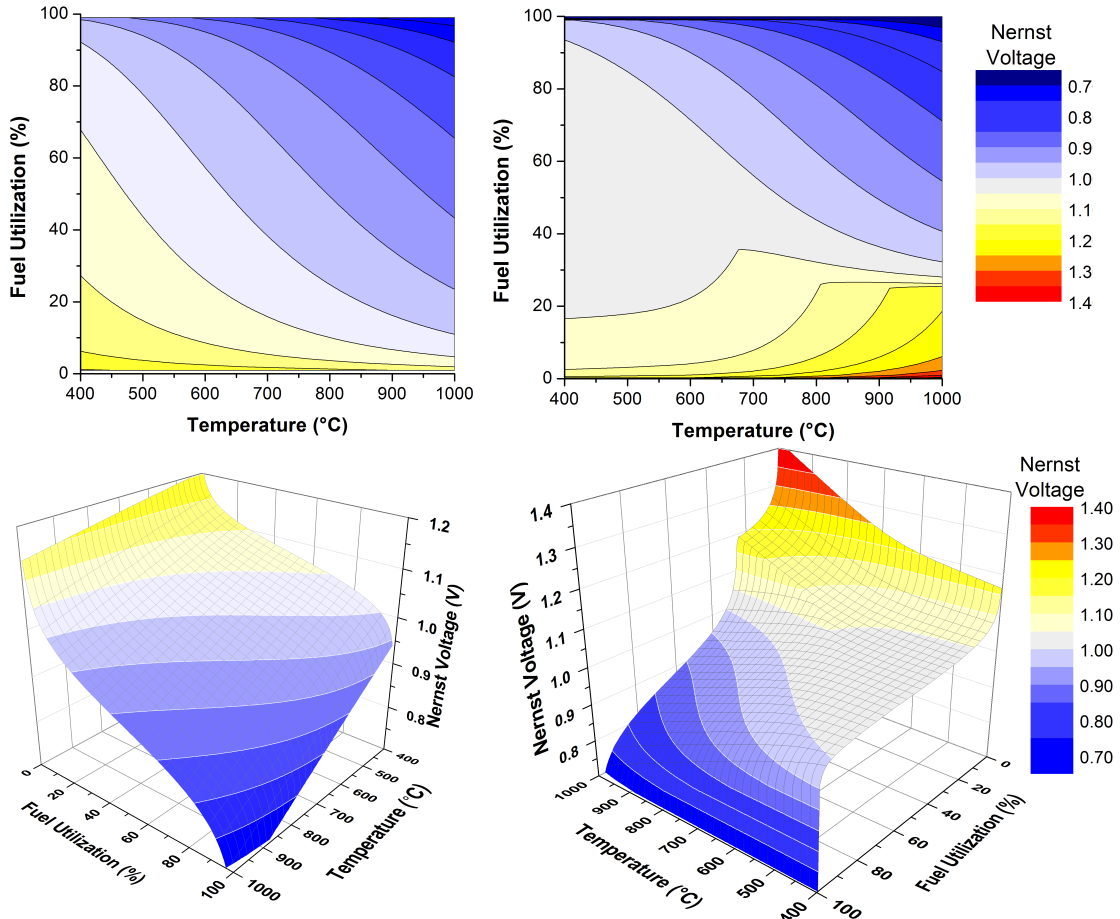


Figure 3.5: 2D (top) and 3D (bottom) contour maps of the OCV vs. Fuel Utilization for H₂ (left) and CH₄ (right) fuel. Note that the temperature scales are reversed to show the surface of the 3D contour plot more effectively.

3.3 Formation of Solid Carbon from Hydrocarbons in SOFC Anodes

One of the key challenges when using hydrocarbon fuels is preventing the formation of solid carbon, or coke, within the anode [29, 40-43]. The solid material blocks the pores necessary for fuel transport to the electrolyte and deactivates the cell. It can cause mechanical damage to the SOFC as well [43-45]. Several reactions can lead to carbon deposition (Reactions 5, 9, & 10 in Table 3.1). Methane cracking (Reaction 5) is favored at higher temperatures, while CO disproportionation (Reaction 9) and CO reduction (Reaction 10) are favored at lower temperatures. The equilibrium of methane cracking, CO disproportionation, and CO reduction are plotted in Figure 3.6a, b, and c, respectively.

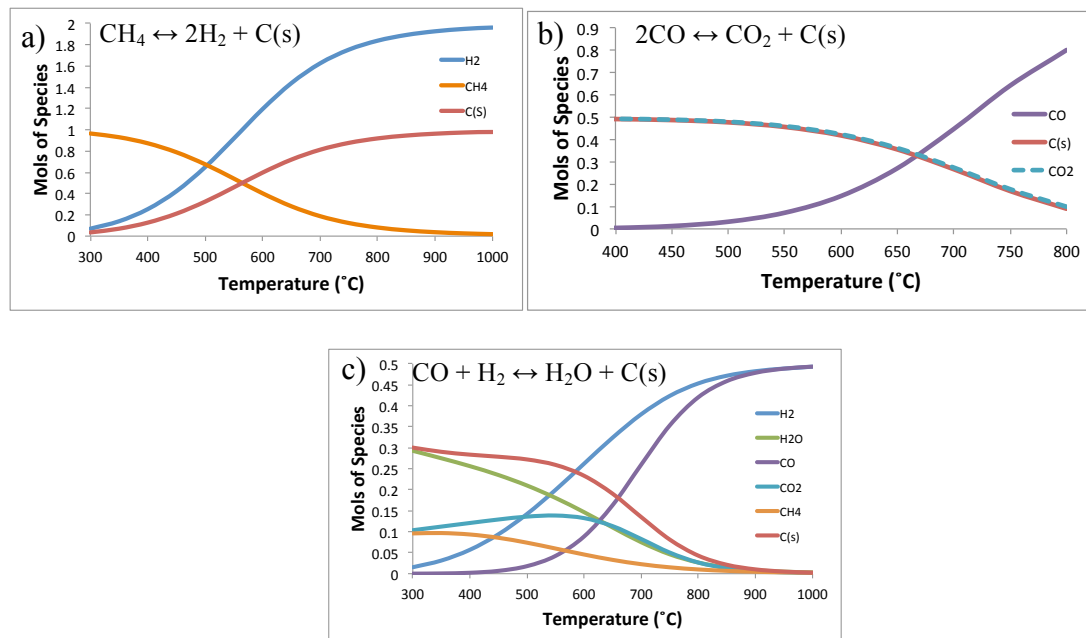


Figure 3.6: Temperature Dependence of Coking Reactions a) Methane cracking b) CO disproportionation c) CO reduction

The operating temperature and fuel composition determines the reactions that occur and the resulting morphology of any solid carbon that may form. Carbon can deposit as an amorphous surface film, or as ordered carbon fibers [46]. Generally, the carbon deposition is more graphitic at higher SOFC operating temperatures. Additionally, carbon can form a solid solution with transition metals at high temperatures. All of these deposition types are deleterious to SOFC structure and performance. The formation of solid carbon for different fueling and operating conditions can be calculated using the same methods as in the previous section, using graphite as the solid carbon phase. The parameters for graphite were used for all C(s) species because it is the most thermodynamically favorable species of solid carbon during SOFC operation at the temperatures studied. Amorphous carbon or carbon nanofibers deposit kinetically but are energetically unfavorable and will form graphite over time, as confirmed by both theory and experiments [47, 48]. Graphite will form at the largest range of fuel compositions of any C(s) species, so is the most critical to look for.

For equilibrium analysis in its most basic form, only the relative carbon, hydrogen, and oxygen molar ratios are needed to determine the conditions for solid carbon formation. For example, the mol fraction of C(s) formation at 650 °C is given in a C-H-O ternary diagram in Figure 3.7. The fuel utilization required to prevent C(s) formation can be determined using the diagram by tracing from the starting stoichiometry of the fuel (all hydrocarbons will lie on the C-H tie line) to its fully oxidized stoichiometry, as shown for CH₄ and C₈H₁₈. This process is tedious, and a ternary plot must be used for each temperature, so for practical purposes contour plots are useful once again, with starting fuel composition held constant in each case.

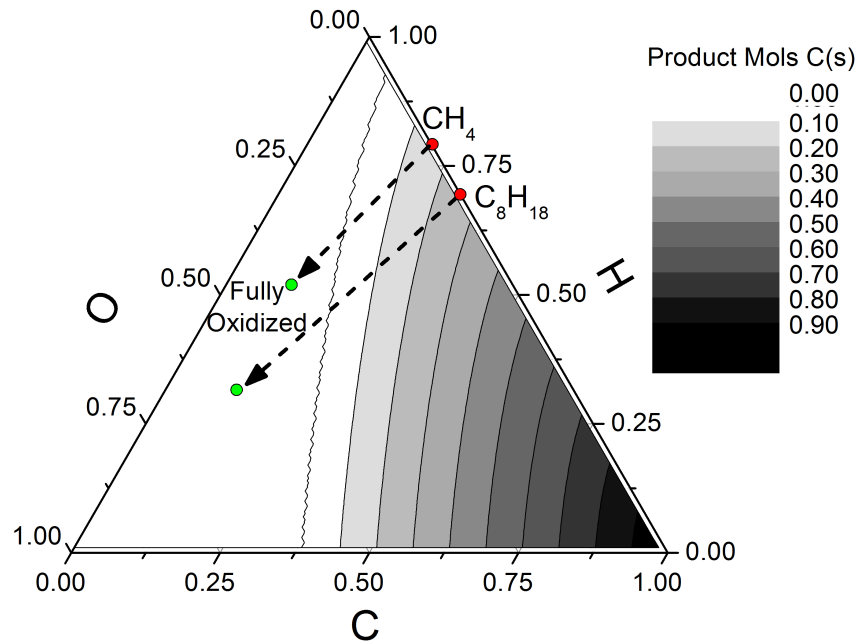
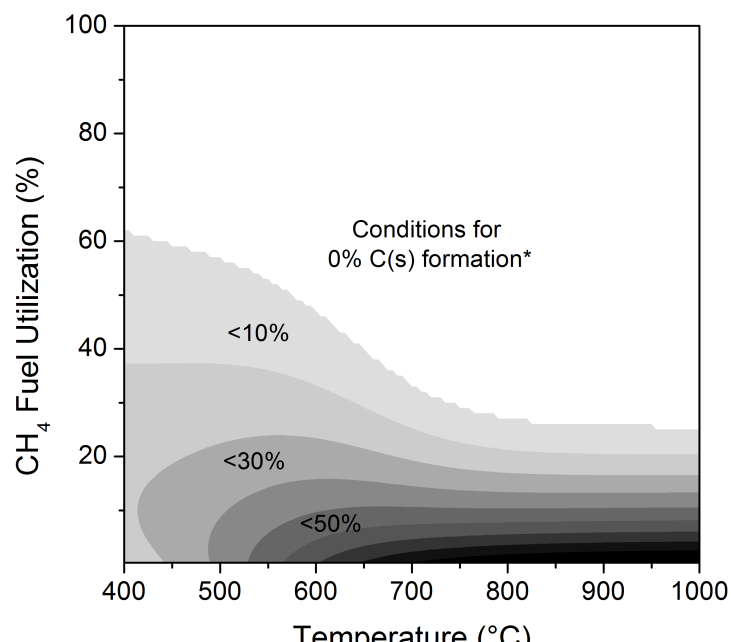


Figure 3.7: Ternary plot of C(s) formation at 650 °C. Red points shows C:H:O ratio of methane (1:4:0) and octane (4:9:0), and green points show fully oxidized C:H:O ratio for methane (1:4:4) and octane (4:9:17).



*Solid carbon percent of total carbon in system

Figure 3.8: Carbon formation vs. fuel utilization for methane fueling

A contour plot for the effect of methane fuel utilization on the formation of carbon at temperatures from 400 – 1000 °C is given in Figure 3.8. This plot is more immediately instructive than the more generalized ternary plot. It shows that at 1000 °C, only ~25% fuel utilization is required to prevent C(s) formation, while below 750 °C the required fuel utilization rapidly increases to ~ >60%. Note that the position of the onset of C(s) formation at each temperature in Figure 3.8 matches the conditions where there is a discontinuity in the Nernst voltage for the 3D contour plot in Figure 3.5, so the effects are related.

3.3.1 Overcoming Solid Carbon Deposition through External Reforming

The typical method of preventing coking is reforming the hydrocarbon fuel externally into syngas, a mixture of CO and H₂ that is more rapidly oxidizable, before it enters the SOFC. Three approaches to reforming are used to suppress C(s) formation: dry reforming (CDR) using CO₂, steam reforming (SR) using H₂O, and partial oxidation (POX) using pure O₂ or air [2, 4]. CDR proceeds by Reaction 8, SR by Reaction 7, and POX by Reaction 4. Combinations of these reforming methods can also be used, but are not investigated for the time being to minimize the computational complexity of this study. Furthermore, when the resulting syngas is oxidized at the triple phase boundary in the anode, the water-gas shift (WGS) reaction (Reaction 6) takes place in the bulk gas to make H₂. The WGS produced H₂ is electrochemically oxidized 2-10 times faster than CO on SOFC anode surfaces [49], while oxidizing CO to CO₂ in the gas phase.

Plots of the C(s) formation versus extent of external reforming are given for 800 °C, 550 °C, and 300 °C for SR, CDR, and POX in Figure 3.9. The effect of reformation on the theoretical OCV of a cell utilizing that fuel is also plotted in order to highlight the

decreased performance that the external reformation may cause. As can be seen from the figures, of the three reformation techniques, only steam reforming remains effective at the lowest temperature (300 °C). CDR cannot prevent C(s) formation at low temperature. At the temperatures and flow rates studied, POX does not prevent C(s) formation until most of the fuel is exhausted, which is counterproductive because little fuel is left for the SOFC to oxidize, and hence the OCV goes to zero. Thus, for external reforming, SR is the most reliable method to produce syngas that prevents coking but has minimal negative impact on OCV. Water content in the fuel is required to be $\geq 30\%$ to ensure no coking, depending on the operating temperature. This steam content will dilute the fuel, which may lead to fuel diffusion limitations during SOFC operation. The amount of steam required for effective reforming is plotted in the contour map in Figure 3.10.

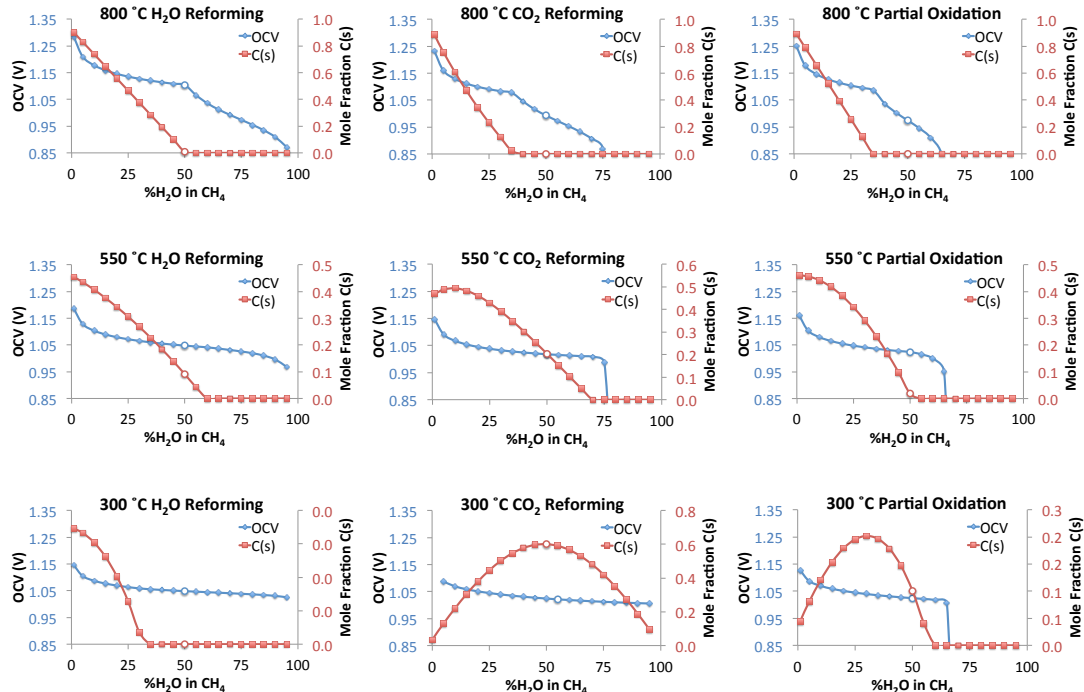


Figure 3.9: The effect of SR, CDR, and POX on carbon deposition and OCV at 800, 550, and 300 °C.

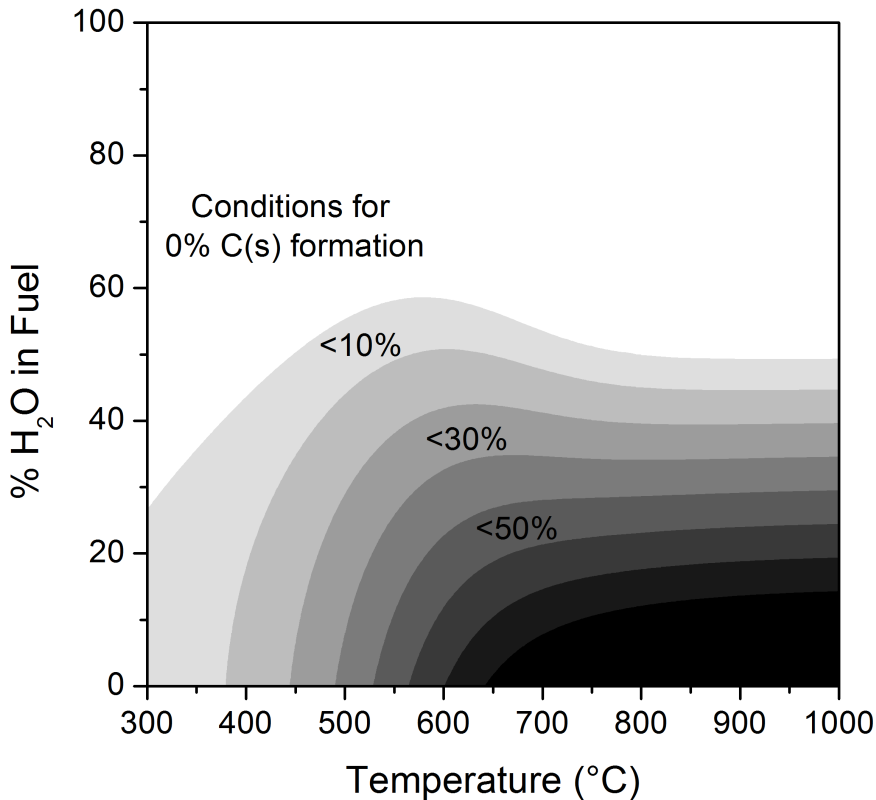


Figure 3.10: The effect of steam concentration in methane on carbon formation

3.3.2 Specific Examples of Effluent Gas from External Reformers

The effluent from a commercial fuel reformer depends on the conditions under which it is run and the catalysts used. Furthermore, the specific composition of liquid fuels such as kerosene-based JP5 or gasoline can vary and thus are difficult to model. For the purpose of this dissertation, the actual effluent concentration from SR and POX reformers are used as a starting point for analysis. The reformatte concentration of a JP5 reformer, provided by the Office of Naval Research, and of different methane reforming conditions are given in Table 3.2. The slip percentage of the methane reformatte is the molar ratio of unreformed methane mixed with the reformed gas effluent, on an inlet flow

ratio basis; the 0% slip has only reformate (0:1 bypassed to reformed ratio, = 0%), whereas the 100% slip case has equal molar amounts of methane fed to the reformer and bypassed (1:1 bypassed to reformed ratio, = 100%). None of the reformate compositions studied form C(s) at SOFC operation temperatures between 300 – 1000 °C. The Nernst OCV for each fuel vs. operation temperature is plotted in Figure 3.11 and compared to H₂ and CH₄ fueling. The drop in OCV for reformed fuels at >700°C is partly due to the conversion of CH₄ (positive slope vs. T) to H₂ (negative slope vs. T). Actual SOFC button cell performance using these reformates is presented in Chapter 4.

Table 3.2: Effluent Composition of methane and JP5 external reformers

	Reformed CH4, 0% Slip (mole fraction)	Reformed CH4, 100% Slip (mole fraction)	Reformed JP5 (mole fraction)
H2	0.461	0.389	0.307
H2O	0.352	0.296	0.245
CO	0.044	0.037	0.094
CO ₂	0.083	0.07	0.092
CH4	0.061	0.209	0.0082
N2	0	0	0.2538
Steam:Carbon	3:1	1.5:1	2.35
Air:Carbon	0	0	1.65

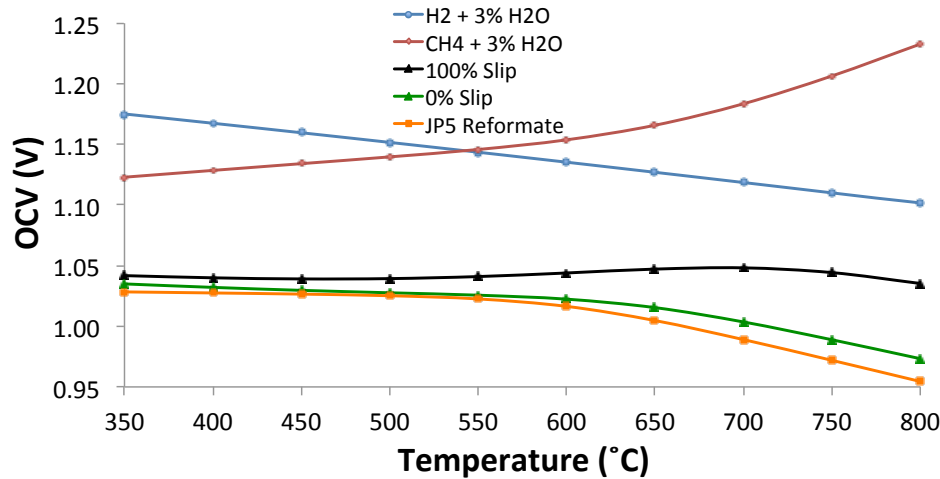


Figure 3.11: Nernst OCV of SOFCs operating on hydrogen and reformed methane

3.3.3 Reforming Exclusively Within the SOFC Anode

The primary consequence of relying on external fuel reforming is the reforming apparatus itself. The added components required for the reformer impacts the overall volumetric power density of a deployed SOFC unit. They add component cost and a parasitic load required to vaporize water used in steam reforming. For these reasons, it is beneficial to design an SOFC that can accomplish all necessary fuel reforming within its anode support, often referred to as *direct internal reforming* [45, 50]. An SOFC of this type could be directly fed with natural gas or other hydrocarbons in order to operate.

There are two ways to achieve this without depositing carbon in the anode. The first is to operate at very high current densities, so that the flux of products dilutes the fuel enough to prevent the formation of solid carbon [51]. This approach has only ever been demonstrated in button cells where the fuel feed location is unrealistic. It is difficult to achieve a similar effect near the fuel inlet of a large planar SOFC, however, since the utilization is inherently low in this region where fresh fuel is continuously supplied. As seen earlier in this chapter, the minimum fuel utilization required to prevent carbon deposition is >25%. It is therefore unlikely for this approach to be successful for long periods of SOFC operation for cells large enough to be implemented in commercially viable products.

The second, more promising approach that becomes apparent after this thermodynamic investigation is to ensure that the metal surfaces (where the solid carbon initially deposits) have higher oxygen activity than the bulk gas. This situation ensures that no C(s) forms kinetically, even though it is favored thermodynamically in the bulk gas compositions. The required oxygen availability required at the metal surfaces (i.e.

Ni, Cu, etc) to ensure that no accumulation of solid carbon forms is plotted in Figure 3.12. SOFC anodes that utilize this strategy are presented in Chapter 5-6.

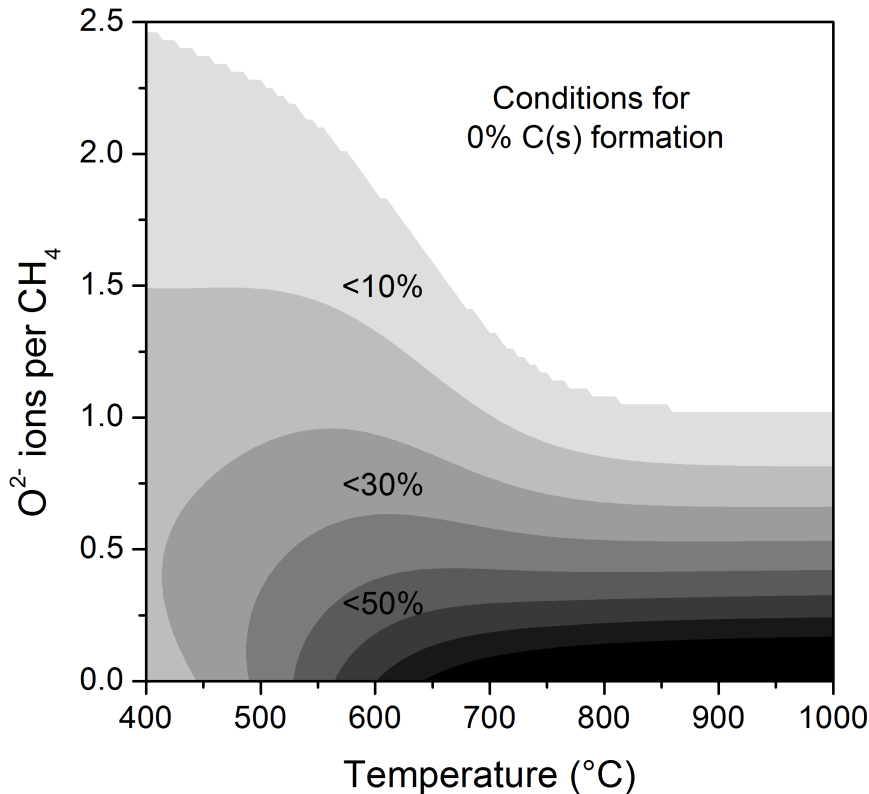


Figure 3.12: Surface oxygen availability per CH_4 required to prevent carbon deposition

3.4 Conclusions

In this chapter, thermodynamic considerations of hydrocarbon fueling of SOFCs have been discussed. The change in Nernst OCV versus temperature with fueling is dependent on the reactions involved in the equilibrium. They also affect how the Nernst voltages decreases with increasing fuel utilization. Depending on the spontaneity of several key reactions, a condition with high OCV may exhibit a rapidly decreasing Nernst

voltage as the fuel is oxidized. Fuels and operating conditions that result in a flatter voltage profile, on the other hand, should allow for a more reliable potential distribution within large SOFC stacks.

Coking mechanisms and the effects of reforming have been discussed. External reforming via CDR, SR, and POX is the standard approach, but only SR prevents C(s) formation at the desired operation temperatures without causing a large corresponding loss of Nernst potential. Internal reforming relying on a high current density is not feasible for large planar SOFCs, but anodes engineered to ensure high oxygen availability on transition metal surfaces are a promising alternative. They deliver a high surface coverage of oxygen on metal surfaces that disrupts C(s) formation.

Chapter 4: Operation of SOFCs on Reformed Liquid Fuels and Natural Gas

4.1 Introduction

Steam reforming is the most effective option for externally reforming hydrocarbon fuels for intermediate temperature SOFCs without diminishing Nernst voltage, as discussed in the previous chapter. Though the reforming process prevents expected formation of solid carbon in the anode in thermodynamic equilibrium, it must be verified kinetically. Accumulated carbon deposits are still possible if the reaction rate for carbon formation is significantly faster than for the reverse reaction. Furthermore, the oxidation kinetics of the reformed fuels at the SOFC anode affect the power density of the cells, so those must be investigated as well. Kinetic studies on patterned electrodes with well defined active triple phase boundary (TPB) densities and geometries exist for many common SOFC materials and fueling conditions [49, 52-54]. The geometry of manufactured SOFC anodes are not as tightly controlled, so the kinetics are difficult to model with much accuracy. Experimental validation remains the most reliable way to confirm the effects of fuel reforming on SOFC anode performance.

In this chapter, the kinetics-dominated parameters of interest are the maximum achievable power density (MPD), the overpotentials caused by charge and mass transfer limitations, and the possible accumulation of solid carbon in the anode. Hydrogen fueling is used as a baseline to investigate the effects of fuel utilization (equivalent to H₂:H₂O ratio in that case) on SOFC performance. Operation on reformed methane and

JP-5, a Naval jet fuel, is extensively characterized as well. Finally, the impact of hydrocarbon fuel reforming on SOFC performance and long-term stability is presented.

SOFCs with a Ni-GDC cermet anode with a Ni-GDC anode functional layer (AFL) [55], a GDC electrolyte, and an LSCF-GDC cathode are used for this study (Figure 4.1). Cells of this type deliver high power density during intermediate temperature operation using hydrogen as a fuel [12, 55-57], and thus are used to establish a reliable baseline for SOFC performance on reformed fuels at those temperatures. Furthermore, SOFCs of this type are manufactured using scalable processing techniques and have been implemented in kW-sized stacks, so they are well-poised to use reformed hydrocarbon fueling.

The reformed JP5 portion of this study is adapted from Lee, Gore, and Wachsman, *Feasibility of low temperature solid oxide fuel cells operating on reformed hydrocarbon fuels, J. Mater. Chem., 22, 22405 (2012)*. - Reproduced by permission of The Royal Society of Chemistry.

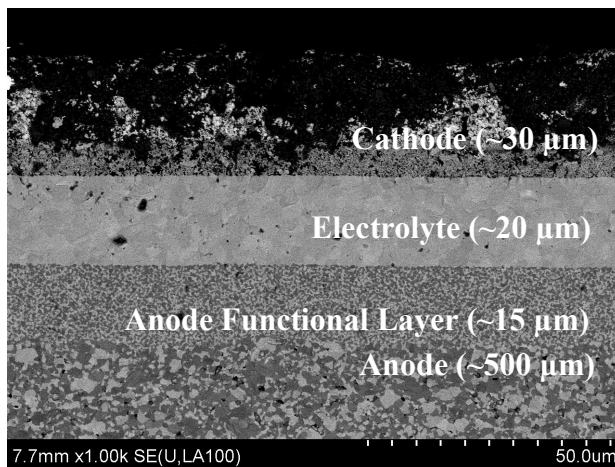


Figure 4.1: Cross-section of untested SOFC before reducing of NiO to Ni metal

4.2 Experimental:

4.2.1 Cell fabrication

NiO–GDC anode supports were fabricated by tapecasting. Micron-scale NiO particles (Alfa Aesar) were mixed with nano-scale $\text{Ce}_{0.9}\text{Gd}_{0.1}\text{O}_{1.95}$ (GDC) particles from Rhodia in a 65:35 wt% ratio with a polymeric binder system based on an ethanol and toluene solvent. The prepared slurry was tapecast with a Procast tape casting system (DHI, Inc.). The dried tape was pre-sintered at 900 °C for 2 h. For the AFL deposition, a 60:40 wt% mixture of submicron diameter NiO powder (JT-Baker) and nano-sized GDC powder (Rhodia) was used. The AFL slurry was colloidally deposited on the anode surface by spin coating and pre-sintered at 900 °C. The GDC electrolyte slurry was spin coated on the AFL surface and the multilayer anode/AFL/electrolyte structure was sintered at 1450 °C for 4 h. A composite cathode consisting of a 50:50 wt% mixture of LSCF (Praxair) and GDC (Rhodia) was prepared and applied on the GDC electrolyte surface by brush painting with an active area of 0.4 cm². The cathode was fired at 1100 °C for 1 h.

4.2.2 Cell Characterization

A schematic of the SOFC characterization system is presented in Figure 4.2. The SOFC anodes were reduced for 10 hours with dry air and humidified H₂ to the cathode and anode side, respectively. The 3 mol% H₂O in H₂ was generated by bubbling the gas through water. For simulating fuel utilization in H₂ and simulating reformed hydrocarbon feeds, appropriate mixtures of H₂, CO, CO₂, N₂, and CH₄ were mixed with

steam vaporized through a coil heated to 150 °C. The liquid H₂O flowrate, before vaporization, was controlled by a syringe pump (KD Scientific, KDS270), and the flowrate of each gas was controlled by calibrated mass flow controllers (MKS 647C). The fuel composition for each fueling condition is given in Table 4.1. To ensure consistency within each data set, multiple fueling conditions were tested on the same SOFC so differences are directly comparable. Data from cells that did not exhibit repeatable performance using H₂ fueling before and after a set of measurements was recorded, indicating microstructural degradation or seal leakage, were discarded. Open circuit voltage and galvanic sweep measurements were evaluated with a Solartron 1287 potentiostat. EIS with a two-point probe configuration was measured at OCV and applied potentials using a ParStat 2273 (Princeton Applied Research) over a frequency range of 100 kHz to 100 mHz. For the JP5 reformate fueled SOFC, a long-term potentiostatic test was carried out at 550°C at the conclusion of other tests. The CH₄ reformate fueled SOFC was held in 100% slip fueling condition for 100 hours. The temperature of the gas in the SOFC anode chamber near the surface of each anode was measured using a K-type thermocouple. The SOFC microstructures before and after testing were observed using SEM (Hitachi SU-70), and the presence of carbon deposition was determined by elemental analysis of the anodes using EDS. Thermodynamic comparisons are made with the Nernst voltages and solid carbon deposition conditions calculated in Chapter 3.

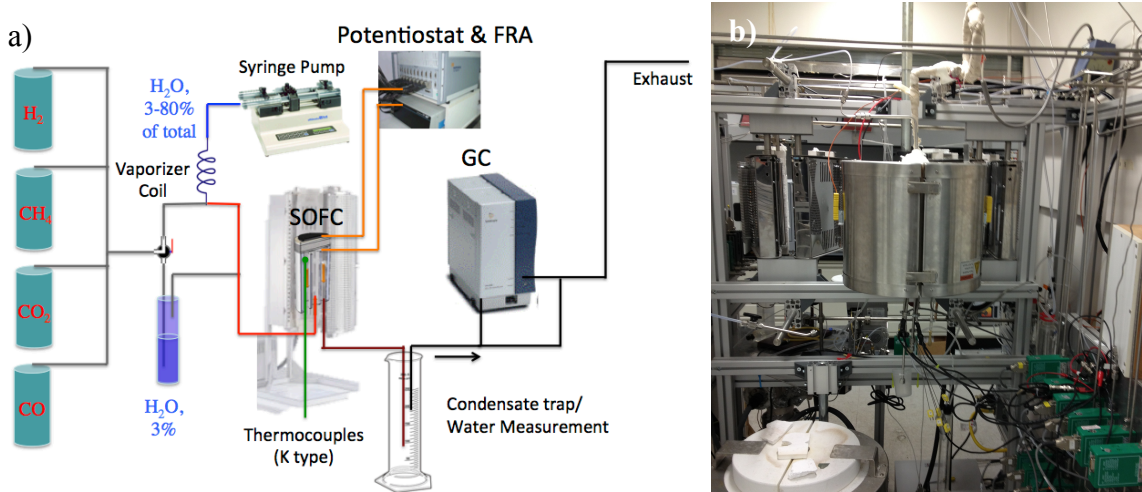


Figure 4.2: a) schematic and b) photograph of the SOFC characterization system used in this study

Table 4.1: Composition (mol fraction) of the model reformates used in this study

	Reformed CH ₄ , 0% Slip (mole fraction)	Reformed CH ₄ , 100% Slip (mole fraction)	Reformed JP5 (mole fraction)
H ₂	0.461	0.389	0.307
H ₂ O	0.352	0.296	0.245
CO	0.044	0.037	0.094
CO ₂	0.083	0.07	0.092
CH ₄	0.061	0.209	0.0082
N ₂	0	0	0.2538
Steam:Carbon	3:1	1.5:1	2.35
Air:Carbon	0	0	1.65

4.3 Results

4.3.1 The Effect of Fuel Utilization on Performance Using H₂ as a Fuel

The fuel utilization (U_f) of pure hydrogen fuel is equivalent to the molar concentration of steam in the fuel stream. The current-voltage response and resulting power density of the SOFC at 650 °C is plotted in Figure 4.3 for hydrogen fuel utilizations of up to 75%. The maximum power density (MPD) at $U_f = 50\%$ is within \pm

2% of that of the $U_f = 0\%$ case, but then decreases as the U_f increases further to 75%. At 50 ccm and $U_f = 75\%$, the MPD decreases by 44%. As the fuel flow rate is increased from 50 ccm to 100 ccm, the MPD at each U_f increases by 2- 21%. The values for change in MPD are given in the final row of Table 4.2. The improvement is greater at greater U_f .

Table 4.2: Effect of fuel utilization and flowrate on the properties of a H₂ fueled SOFC

50 ccm flowrate, $U_f =$	0%	50%	62.5%	75%
Meas. OCV (mV)	0.764	0.768	0.769	0.749
Nernst Voltage (V)	1.127	0.989	0.968	0.945
Anode T (°C)	658.3	655	653.8	652.9
ASR Ohmic ($\Omega \text{ cm}^2$)	0.142	0.144	0.152	0.167
ASR Total ($\Omega \text{ cm}^2$)	0.342	0.351	0.390	0.456
ASR Electrode ($\Omega \text{ cm}^2$)	0.200	0.207	0.238	0.289
MPD (W/cm ²)	0.463	0.454	0.350	0.260
$\Delta \text{MPD vs. } 0\% \text{ FU}$	0.0%	-1.8%	-24.5%	-43.9%
100 ccm,flowrate $U_f =$	0%	50%	62.5%	75%
OCV (mV)	0.757	0.766	0.77	0.77
Anode T (°C)	659.1	658.2	657	655.6
ASR Ohmic ($\Omega \text{ cm}^2$)	0.139	0.139	0.146	0.152
ASR Total ($\Omega \text{ cm}^2$)	0.329	0.325	0.374	0.421
ASR Electrode ($\Omega \text{ cm}^2$)	0.190	0.186	0.228	0.269
MPD (W/cm ²)	0.471	0.483	0.406	0.313
$\Delta \text{MPD vs. } 0\% \text{ FU}$	0.0%	2.4%	-13.9%	-33.6%
$\Delta \text{MPDvs.50 ccm}$	1.8%	6.2%	16.0%	20.6%

Nyquist plots of the EIS response at cell potentials from OCV to 0.5 V are plotted in Figure 4.4 for U_f from 0 – 75%. The real impedance for the Ohmic (high frequency x intercept) and total ASR (low frequency x intercept) are nearly identical for $U_f = 0\text{-}50\%$, and then increase with increasing U_f above 50%. The electrode ASR, equal to total ASR minus Ohmic ASR, increases significantly more than the Ohmic ASR. Also, as the cell potential is decreased by the increasing DC current density, the magnitude of the electrode ASR increases in each case. The change in total ASR at each voltage matches

the change in slope of the I-V curve in Figure 4.3 at each voltage, as expected from Ohms law. At high U_f and low cell potential, the EIS signal gets very noisy and obscures the total ASR intercept, but the total ASR value can be determined from the slope of the IV curve in those cases.

The cause of the onset of MPD loss at $U_f > 50\%$ is clarified by Figure 4.5, which plots the total, Ohmic, and electrode area specific resistances (ASRs) and the MPD versus the U_f and fuel flowrate. Above $U_f = 50\%$, the electrode ASR increases significantly, and is inversely proportional to the MPD.

In most cases, a slight increase in OCV was observed as the U_f increased, which is counterintuitive. Oxidizing the fuel increases the PO_2 at the anode, decreasing the ΔPO_2 across the electrolyte, which causes a drop in the Nernst potential that the SOFC can theoretically achieve at OCV. The calculated Nernst potential of a cell drops from 1.127 V at $U_f = 0\%$ to 0.945 V at $U_f = 75\%$. This is expected to correlate with a drop in the observed OCV on the order of 0.182 V, but instead an increase is observed. This discrepancy is partially explained by Figure 4.5b, which shows that the temperature of the anode atmosphere decreases as the U_f increases. The temperature likely decreases because the volumetric heat capacity of steam is >2 times that of hydrogen, so an identical flowrate of the gas removes more heat from the system at higher U_f . The increase in Ohmic ASR with increasing U_f may be attributed to the temperature decrease, since conductivity is thermally activated. Interfacial resistance due to H_2O coverage of active catalytic sites could also contribute to this increase in Ohmic ASR. Additionally, the increased anode PO_2 may be decreasing the electronic conductivity in the GDC. The increased PO_2 at the anode caused by the additional water puts GDC closer to its

electrolytic domain, decreasing the amount of Ce^{4+} that forms from Ce^{4+} in strongly reducing atmospheres and causes electronic conduction by small polaron hopping. This will diminish the electronic conductivity of the GDC in addition to the thermal effects on its ionic conductivity. Keeping the anode temperature constant between different fueling conditions will help clarify the separate effects of temperature and fuel composition.

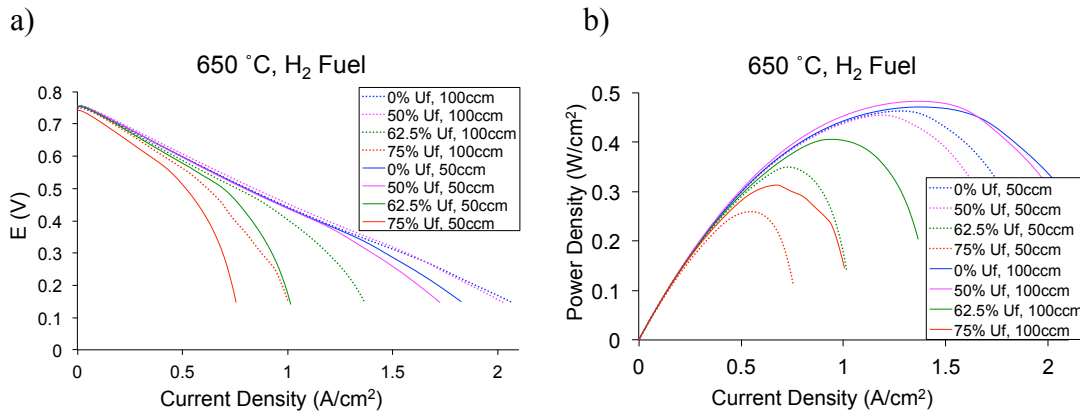


Figure 4.3: The effect of H₂ fuel utilization (FU) and flowrate on the a) current-voltage and b) power density characteristics of an SOFC at 650 °C

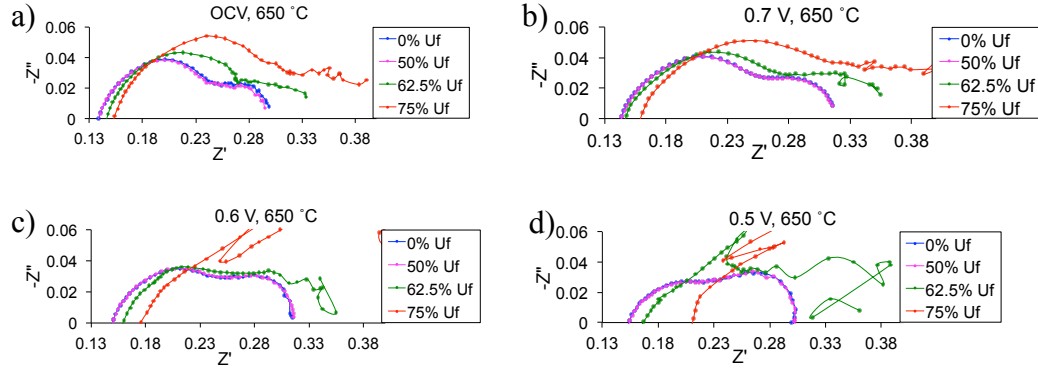


Figure 4.4: EIS response at H₂ fuel utilization from 0-75% at cell voltages at 650 °C at a) OCV, b) 0.7 V, c) 0.6 V, and d) 0.5 V.

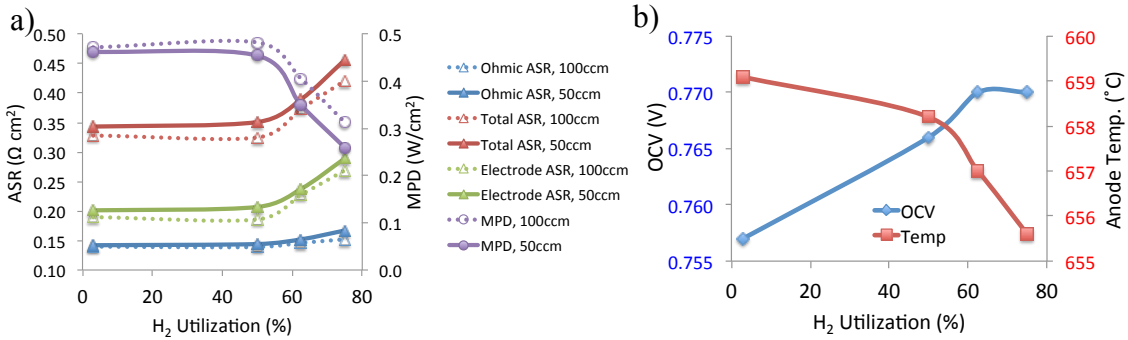


Figure 4.5: The effect of H₂ fuel utilization and flowrate on a) the ASRs and MPD and b) the OCV and temperature of an SOFC at 650 °C.

4.3.2 SOFC Operation on Steam-Reformed Methane

The furnace temperature was adjusted to keep the anode temperature at 600 ±0.4 °C or 650 ±0.3 °C for the reformed methane fueling tests. This compensation was to counteract the cooling effect observed during high U_f of hydrogen fuel, since the temperature change convolutes the effects of fuel composition on OCV, ASR, and MPD. The resulting current-voltage responses of the SOFC for each fueling condition are plotted in Figure 4.6, and the EIS response for each is plotted in Figure 4.7. The OCV remains effectively constant for each fueling case, with <0.5% variation between the three conditions. This is again unexpected because the calculated Nernst voltage for reformed methane fueling is 0.08 – 0.11 V lower than that of hydrogen fueling, as presented in Table 4.3.

The Ohmic ASR increases with changing fuel composition from H₂ to reformed methane as well, despite the furnace adjustment to ensure constant anode temperature. The effect is less severe (5.9–9.3% increase) than that observed in H₂ fuel utilization experiments (≤17.6% increase), suggesting that the temperature compensation had a measurable effect on the observed Ohmic ASR. This suggests that surface coverage of

catalytic sites at the triple phase boundary (TPB) become partially blocked by the H₂O or CO₂ and increase the interfacial resistance of the anode. At 650 °C, the increase in electrode ASR at 0.7 V when using reformed methane is 2-3 times greater than the increase in Ohmic ASR. Furthermore, the electrode ASR for all three fuels increases with increasing current density (decreasing voltage). This indicates that the increase in electrode ASR dominates the increase in total ASR in each case at this temperature. At 600 °C, the increase in both ASR contributions is similar, and the electrode ASR is less drastically increased when the cell is pushed to lower potentials. The total ASR is inversely proportional to the MPD in each fueling condition at each temperature, just like it was with hydrogen at U_f>50%.

After testing for 100 hours in the 100% slip composition of steam- reformed CH₄, the SOFC anodes showed no indication of carbon deposition. The anode-fuel and anode-electrolyte interface is shown in Figure 4.8, confirming that the anode morphology is homogeneous and free from visible carbon deposition. EDS measurements were consistent with this observation, showing no carbon signal above typical background signals.

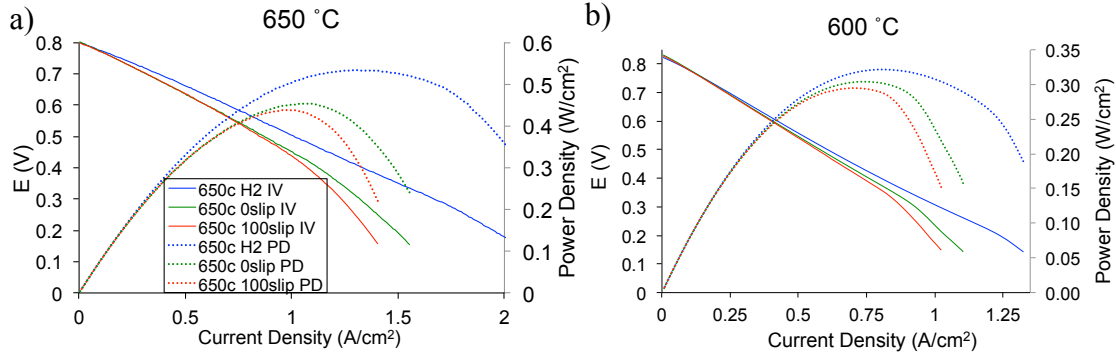


Figure 4.6: Current-voltage response and power density of SOFCs operating on reformed methane fuel at a) 650 °C and b) 600 °C

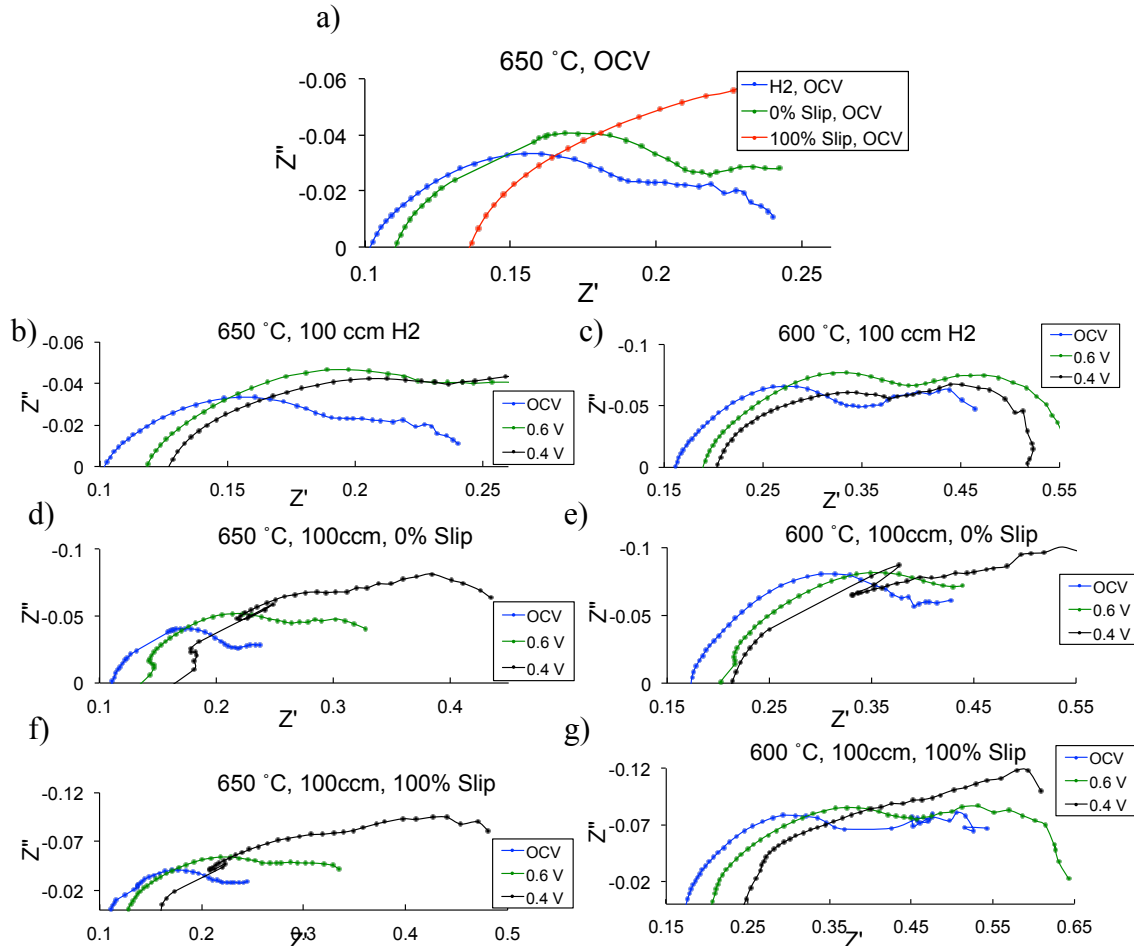


Figure 4.7: EIS response at OCV and under polarization for different fuel compositions (H₂, 0% Slip, 100% Slip) and potentials from OCV to 0.4 V at 650 °C and 600 °C. a) Comparison of the three fueling conditions at OCV at 650 °C. b) H₂ at 650 °C, c) H₂ at 600 °C, d) 0% slip at 650 °C, e) 0% slip at 600 °C, f) 100% slip at 650 °C, f) 100% slip at 600 °C.

Table 4.3: Effect of fuel composition and operating temperature on the performance of and SOFC fueled by hydrogen and reformed methane at 650 °C.

	H₂	0% Slip	100% Slip
Measured Temp (°C)	650	650.1	650.3
Furnace Temp. (°C)	646	647	648
Measured OCV	0.799	0.802	0.799
Nernst OCV	1.127	1.015	1.047
MPD (W/cm ²)	0.533	0.453	0.438
Δ MPD vs. H ₂	n/a	-15.1%	-18.0%
Δ Ohmic ASR @ 0.7 V vs. H ₂	n/a	7.0%	9.3%
Δ Electrode ASR @ 0.7 V vs. H ₂	n/a	24.4%	21.6%
Measured Temp (°C)	600.1	600.4	599.6
Furnace Temp. (°C)	600	600	600
Measured OCV	0.825	0.833	0.829
Nernst OCV	1.135	1.022	1.044
MPD (W/cm ²)	0.322	0.304	0.295
Δ MPD vs. H ₂	n/a	-5.5%	-8.3%
Δ Ohmic ASR @ 0.7 V vs. H ₂	n/a	5.9%	6.6%
Δ Electrode ASR @ 0.7 V vs. H ₂	n/a	6.9%	7.7%

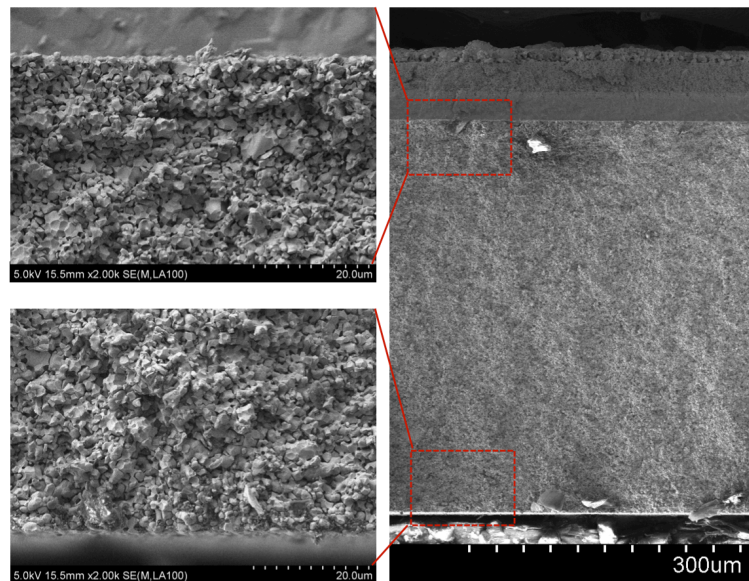


Figure 4.8: SEM micrographs of SOFC after operation on reformed CH₄ (100% slip) for 100 hours. Bottom surface and electrolyte interface show no carbon deposition.

4.3.3 Operation on Reformed JP5 Jet Fuel

Figure 4.9a shows the cross section of the SOFC fueled with JP5 reformat after a long-term potentiostatic test that lasted 500 hours. No obvious degradation of the components was observed. The current-voltage response of an SOFC using reformed JP5 jet fuel at 550, 600, and 650 °C is plotted in Figure 4.9. The OCV does not change appreciably between the H₂ and JP5 reformat fueling, with the maximum difference being 0.01 V at 650 °C where the calculated decrease in Nernst potential is 0.122 V. The MPD decreases when switching to JP5 reformat in each case, as shown in Table 4.4. Similar to the steam-reformed methane, the decrease in MPD is less severe at lower temperatures: ~14% at ≤ 600 °C, but 28.4% at 650 °C.

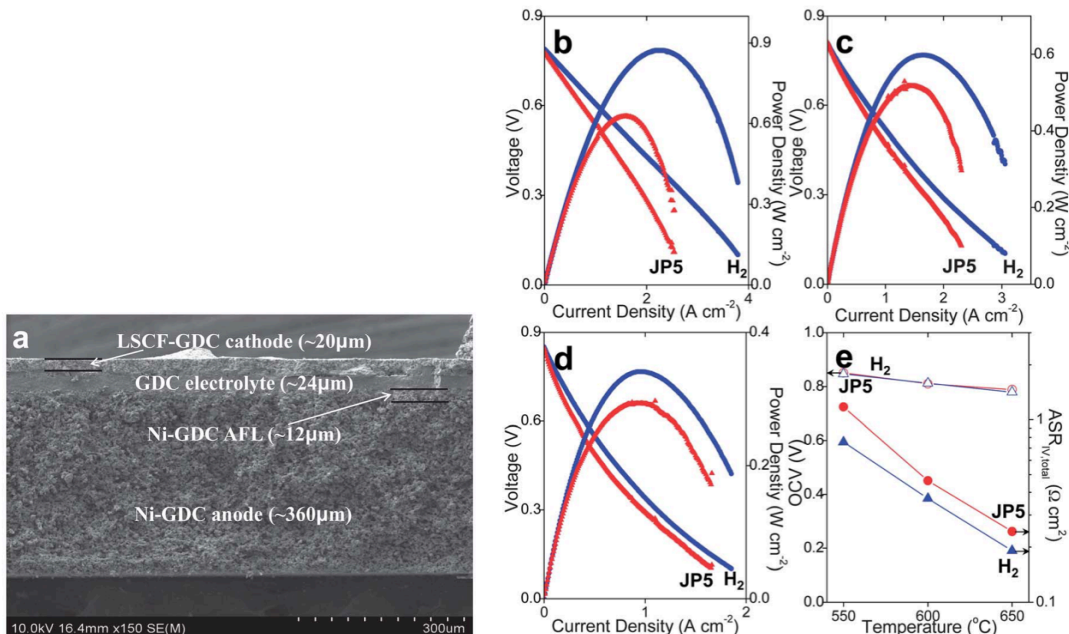


Figure 4.9: (a) SEM micrograph of cross-sectional view of the SOFC after testing. I-V plots of SOFCs operating on H₂(circle) and JP5 reformat (triangle) at (b) 650 °C, (c) 600 °C, (d) 550 °C. (e) OCV (left Y-axis) and total ASR (right Y-axis) of SOFCs operating on H₂(circle) and JP5 reformat (triangle) as a function of temperature.

Table 4.4: Summary of the electrochemical performance of SOFCs using H₂ vs. reformed JP5 jet fuel.

T (°C)	Fuel Type	Calc. Nernst (V)	OCV (V)	Total ASR (Ω cm ²)	Ohmic ASR (Ω cm ²)	Electrode ASR (Ω cm ²)	MPD (mW/cm ²)	Δ MPD (%)
650	H ₂	1.127	0.789	0.191	0.08	0.111	872	
	JP5	1.005	0.779	0.244	0.089	0.155	624	-28.4
600	H ₂	1.135	0.81	0.369	0.116	0.253	598	
	JP5	1.016	0.812	0.464	0.129	0.335	517	-13.5
550	H ₂	1.143	0.851	0.755	0.185	0.57	341	
	JP5	1.023	0.847	1.175	0.243	0.932	293	-14.1

Nyquist plots of the corresponding EIS at OCV for each condition are plotted in Figure 4.10a-c, and the model circuit used for fitting the results is given in Figure 4.10d. The electrode ASR dominates the total ASR for each fuel at each temperature, and all ARS components increase with decreasing temperature. A pronounced increase in electrode ASR is observed with JP5 reformate fueling compared to hydrogen fueling in each case, with only a minor increase in Ohmic ASR, as depicted in Figure 4.10e. The apparent activation energies are calculated for the Arrhenius relationships of the fitted high and low frequency resistive components used in the model circuit that are plotted in Figure 4.10f. The apparent activation energy of the high frequency process is similar (0.5 eV for JP5 vs. 0.51 eV for H₂), suggesting that it is unaffected by the fuel, but the apparent activation energy for the low frequency process is 22% greater.

The power density of the SOFC operating on JP5 reformate for > 500 hours at 550 °C is plotted in Figure 4.11a. The noise in the data is caused by periodic transience in steam flow during the withdraw/infuse cycle of the syringe pump used to deliver the water to the vaporizer coil. An initial power density of 300 mW/cm² is observed, which decays to 220 mW/cm² over the first 100 hours of operation. After that initial decay,

however, the performance stabilized for the remaining 400 hours. The current-voltage response of the SOFC before and after the long-term test is plotted in Figure 4.11b. The MPD is 17% lower after the long-term test, which is related to the increase in total ASR observed in Figure 4.11d.

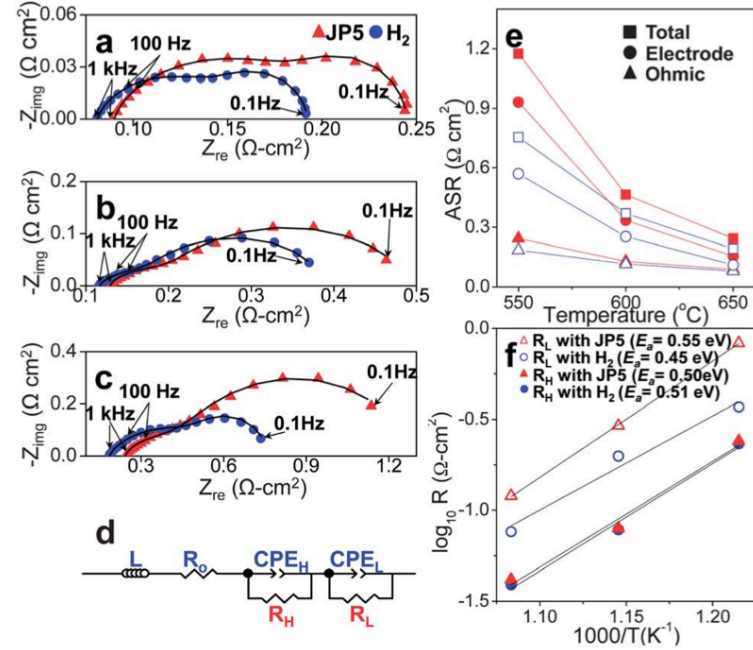


Figure 4.10: Nyquist plots (symbols) and fitting results (line) of SOFCs operating on H_2 (circle) and JP5 model reformate (triangle) at (a) $650\text{ }^\circ\text{C}$, (b) $600\text{ }^\circ\text{C}$, (c) $550\text{ }^\circ\text{C}$. (d) Equivalent circuit for fitting. (e) Total (square), electrode (circle), and Ohmic (triangle) ASRs of SOFCs operating on H_2 (filled symbols) and JP5 reformate (open symbols) as a function of temperature. (f) Arrhenius plots of electrode ASR of SOFCs operating on H_2 (circle) and JP5 reformate (triangle) at low (open symbols) and high (filled symbols) frequency regimes.

After the cell testing was complete, SEM analysis revealed slight coarsening of the Ni particles in the anode, particularly in the submicron Ni particles in the AFL. A magnified cross section of the anode-electrolyte interface is shown in Figure 4.11d. No carbon deposition was observable within the microstructure or using elemental analysis

via EDS. Only a negligible carbon background signal was detected according to the spectra in Figure 4.11e.

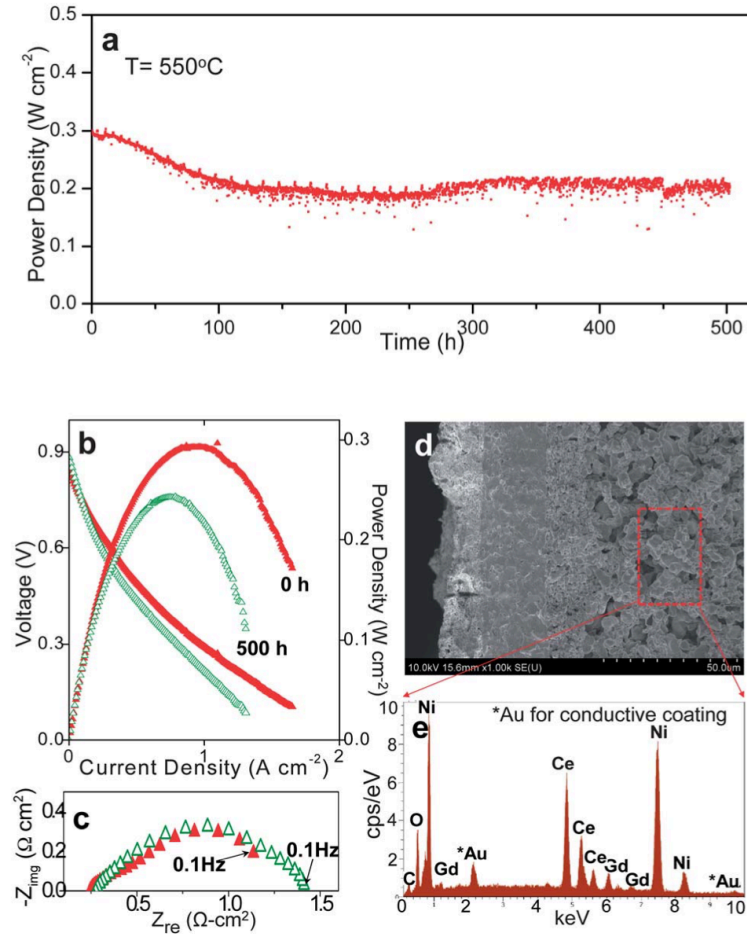


Figure 4.11: (a) Long -term stability test (500 h at 550 °C) of the SOFC operating on JP5 reformate using a potentiostatic mode with an applied voltage of 0.392 V at which MPD was achieved. (b) I-V and (c) Nyquist plots before (filled triangle) and after (open triangle) the long term stability test (d) SEM image of cross sectional view of the SOFC after the 500 h long term test. (e) EDS spectra of the area marked in (d) as a dotted rectangle.

4.4 Discussion:

4.4.1 Electrochemical Performance

Each fueling scenario studied in this chapter exhibits several similar traits. The electrode ASR increases significantly under high H₂ fuel utilization and for reformed hydrocarbon fuels (JP5, CH₄) compared to that of pure H₂ fueling. This effect is attributable to concentration polarization, fuel diffusion limitations in the anode when the fuel is diluted. This is observable by a characteristic increase in low frequency (<100 Hz) polarization in the EIS data in Figure 4.4, Figure 4.7, and Figure 4.10, as well as the increase in slope at high current densities in the current-voltage plots in Figure 4.3, Figure 4.6, and Figure 4.9. As the molar concentration of oxidizable reactants decreases in the fuel atmosphere, the available fuel at the active TPB can be consumed under high current densities faster than it can be replenished by diffusion through the anode pores. Using pure H₂ as a fuel establishes a reliable baseline because it has the smallest molar mass of any fuel and diffuses the fastest. The concentration polarization appears to decrease at lower temperature, as indicated by an apparent activation energy in Figure 4.10f, but in reality this temperature change does not substantially affect the rate of diffusion of the fuel. The temperature does affect the maximum current density that the cell is capable of, however, which is the driving force for fuel depletion at the electrolyte surface. In the reformate fueling cases, this effect of current density is what causes the electrode ASR increase at 650 °C (22-40%) to be more significant than at 600 °C (7-32%) when compared to H₂. The 22% increase in apparent activation energy of concentration

polarization (R_L) in Figure 4.10f when switching from H_2 to JP5 fueling is caused by the higher molecular weight components and dilution of oxidizable species in the JP5 reformate, in conjunction with the current density effect just described.

The change in MPD in each case is inversely proportional to the change in the electrode ASR. The added electrode overpotential causes a corresponding decrease in power at any given voltage. Since the effect of concentration polarization is lower at the lower current densities at lower temperatures, the decrease in MPD when using reformed fuels or high fuel utilizations is less severe as well. In the case of reformed JP5 at 650 °C, the MPD is 28.4% lower than when fueled with H_2 , but it is only 13.5% lower at 600 °C. For steam-reformed methane, the MPD is only 5.5% lower than H_2 fueling at 600 °C, whereas it is up to 18% lower at 650 °C. This indicates that for low temperature SOFCs, the effect of concentration polarization on the performance when using reformed hydrocarbon fuels will be less limiting than it is for high temperature SOFCs. The trends observed in this study are true for the button cells tested, but the effect of anode geometry and fuel fluid dynamics in larger SOFCs will likely introduce additional crucial variables that affect the relative performance on different fuels.

A consistent effect of fueling on Ohmic ASR was observed as well, though it is smaller in magnitude than the effect on electrode ASR. The Ohmic resistance of an SOFC is typically dominated by the resistivity of its electrolyte, the least conductive component. An increase in Ohmic resistance is observed in the EIS studies presented when reformed fuel or a high H_2O content is introduced. The rationale for this is clarified by Figure 4.5b. As the H_2O content is increased in that case, there is a corresponding decrease in cell temperature. The lower temperature increases the

resistance of the electrolyte material, thus appears as an increase in Ohmic ASR in the EIS plots. The only case where no increase in Ohmic polarization was observed was the increase from $U_f = 0\%$ to $U_f = 50\%$ of H_2 , where there was no difference in total ASR either.

Once the temperature was compensated for, however, an increase in Ohmic ASR was still observed with reformate fuels, and the Ohmic ASR increased with increasing current density in every case. The increase is larger when more H_2O or CO_2 are present in the anode, either because they are added initially, or because they are created as reaction products under high current density. This increase in Ohmic polarization is likely due to surface coverage of TPB sites with those species, which are already fully oxidized, that block and inhibit the activity of those TPB sites.

4.4.2 Comparison of Observed Results to Thermodynamic Calculations

The measured OCV of cells for each fuel revealed another consistent, albeit unexpected, phenomena. Though the calculated Nernst OCV for a cell using H_2 as a fuel is >0.1 V higher than any of the reformed fuels, there was no significant observable change in measured OCV when the fuel is switched (Figure 4.12). This is not the case in other studies using YSZ electrolytes (Figure 4.13), where the measured OCV follows the theoretical OCV trends. The anode surfaces in the GDC cells may have significant oxygen surface coverage that affects the measured PO_2 difference between the anode and air under OCV conditions. If the surface saturation is approximately the same at open circuit regardless of fuel concentration, then the measured gradient and resulting OCV will remain the same.

An alternative explanation of the OCV trend is that the mixed conductivity of the GDC electrolyte plays a role in the relatively consistent OCV observed. It is possible that the increased PO_2 of the reformed hydrocarbon fuels causes a decrease in the concentration of small polarons in the GDC by reoxidizing Ce^{3+} , causing an increase in OCV due to a decrease in electronic leakage through the electrolyte that counteracts the decrease in OCV expected.

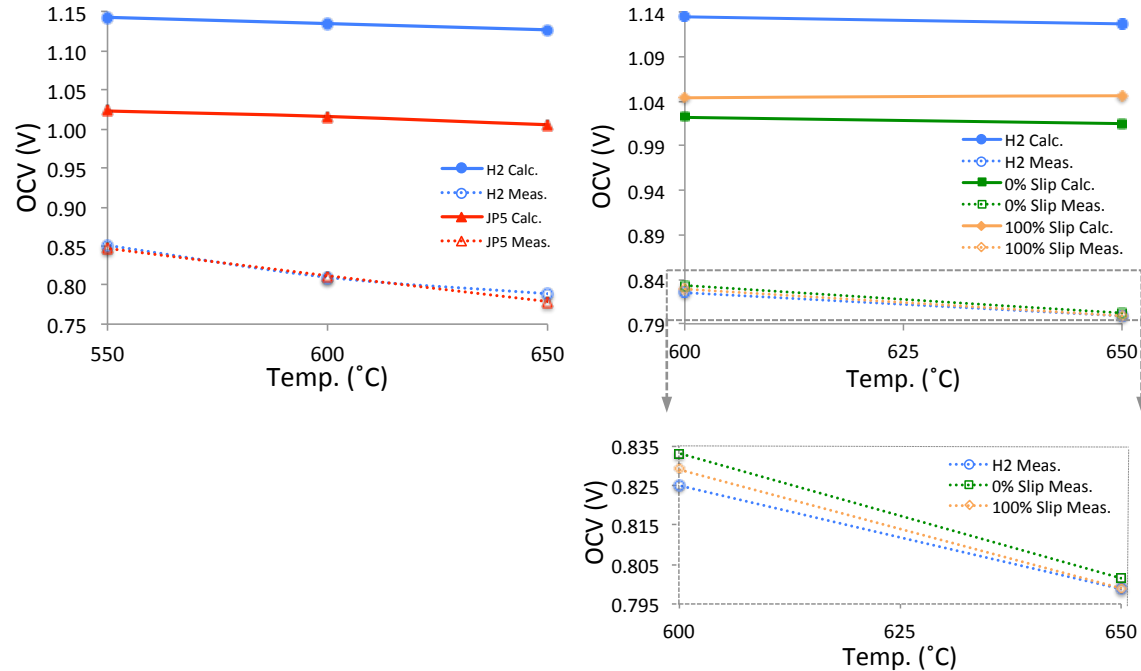


Figure 4.12: Deviation between the theoretical Nernst voltage and the measured OCV for SOFCs using reformed hydrocarbon fuels: JP5 vs. H₂ (left) and reformed CH₄ vs. H₂ (right)

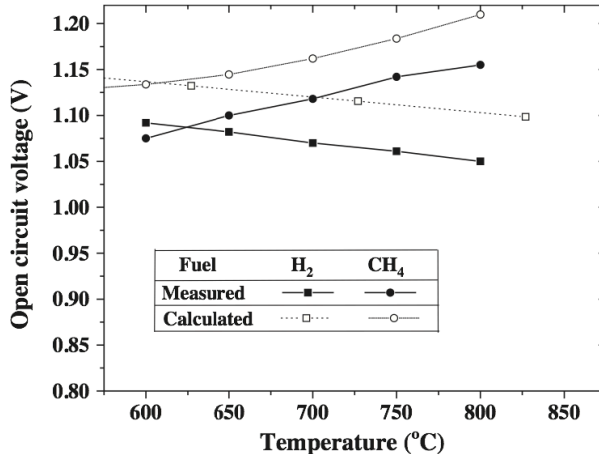


Figure 4.13: Calculated vs. observed OCV for H₂ and CH₄ fuel when a YSZ electrolyte is used, from Lin & Barnett [51]

In the reformate-fueled SOFCs, no carbon deposition was observed within the anodes. The reformate compositions were not expected to form solid carbon in equilibrium, as calculated in Chapter 2, but equilibrium conditions assume that the forward and reverse reactions proceed at the same rate. Realistically, Ni surfaces can catalyze the formation of solid carbon and may disrupt equilibrium conditions and deposit carbon even when it is not predicted by thermodynamics. This is not the case for the fuel compositions studied, however, confirming that thermodynamic calculations are a useful tool that can be realistically applied to SOFC operating conditions. The stable operation of and SOFC on reformed JP5 for over 500 hours is promising for the application of SOFCs in the field using reformed liquid fuels.

4.5 Conclusions:

Operating on reformed fuel is comparable to operating on hydrogen under certain conditions, but more dilute fuel with higher molecular weight components cause greater

concentration polarization. Resulting decreases in MPD compared to H₂ fueling in this study are as large as 28% with reformed liquid fuel (JP5) at higher temperatures (650 °C), and as low at 5% for reformed CH₄ at 600 °C. Even hydrogen fueling suffers from high concentration polarization at high fuel utilizations due to the H₂O generated diluting the remaining fuel, so the problem is not unique to reformed hydrocarbon fuels.

Thermodynamic calculations are useful in determining reformate compositions that do not form solid carbon in the anodes. Even with reformed jet fuel, no coking was observable after >500 hours at 550 °C, which is consistent with calculated equilibrium conditions. This confirms that the kinetics in the relatively hot anode environment (500-650 °C) are fast enough to reach approximately equilibrium conditions, so relatively simple thermodynamic analysis is adequate for the investigated cases. The OCV does not follow the expected change in Nernst voltage based on the equilibrium PO₂ of the fuel used, so a more sophisticated model is required for capturing the OCV behavior of GCD electrolyte cells.

Chapter 5: Development of Porous Ceramic Anode Supports

5.1 Introduction

Solid oxide fuel cells (SOFCs) operate efficiently on both hydrogen and hydrocarbon fuels [1]. Their fuel flexibility makes them desirable energy conversion devices; they can integrate immediately into the current hydrocarbon infrastructure and can utilize renewable fuels in the future once that infrastructure exists [50, 57]. SOFC anodes still require development in order to ensure stable operation on conventional hydrocarbons like methane, gasoline, or diesel, however. Carbon deposition, or coking, due to the CO disproportionation reaction (Eq. 5.1) or CH₄ cracking (Eq. 5.2) can occur when using hydrocarbon fuels, which will block the anode gas channels and diminish SOFC lifetime.



Typical nickel-based cermets used for anode-supported cells exacerbate coking problems because Ni surfaces catalyze solid carbon deposition and can deform upon forming a solid solution with the carbon [46]. Furthermore the ~60% expansion of Ni upon reoxidation complicates its use as supporting material [22]. Many researchers have suggested and demonstrated ceramic anodes as supports for SOFCs to avoid the coking and mechanical problems of conventional cermet anode supports [23, 45, 58-60], but relying on them for electronic conductivity and fuel oxidation catalysis has been a challenge. Transition metals like Ni, Cu, and Co have an electronic conductivity $>10^3$

times that of fuel-stable ceramics (Figure 5.1), however, and are still attractive as electronic conductors that are supported by a ceramic scaffold. The transition metals can also serve as necessary fuel oxidation catalysts at the electrochemically active triple phase boundary (TPB) at the interface between the anode and electrolyte.

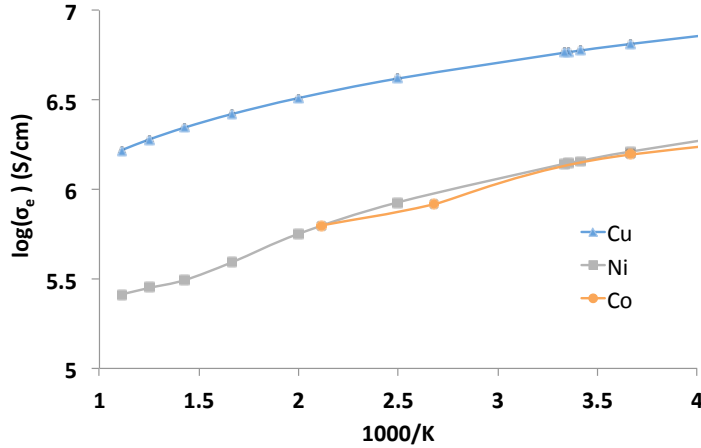


Figure 5.1: Electronic conductivity of pure Cu, Ni, and Co metal vs. T from 0 – 650 °C. Data for Ni and Cu from [20] and data for Co from [61]. Solid lines are a guide to the eye.

Anodes must be >30% porous to have a well-percolated pore network to enable diffusion of gaseous reactants through the supporting anode bulk to the active TPB near the electrolyte, so the properties of porous ceramics for anodes must be well characterized. Unfortunately, the properties of porous ceramics used as anode supports are not as well characterized as the dense materials used for electrolytes or the cermet composites used for supporting anodes, which have been extensively covered by Atkinson, Corbin, and others [62-67]. It is imperative to better understand the relationships between porosity and the electronic and mechanical properties of anode materials in order to employ ceramic materials as structural supports for SOFCs.

Eq. 5.3 and Eq. 5.4 describe general empirical relationships between the elastic modulus (E) and flexural strength (σ_f) of ceramics, respectively, where n is an

empirically-derived fitting parameter relating to pore geometry, P is the porosity volume fraction in the material, and E_o and σ_o are the elastic modulus and strength of the dense material, respectively [68].

$$E = E_o(1 - nP + nP^2) \quad (5.3)$$

$$\sigma_f = \sigma_o e^{-nP} \quad (5.4)$$

Pores lower the strength of brittle ceramic materials under tension by acting as stress concentrators.

The effect of a single, critical flaw or void on strength can be understood using the relationship in Eq. 5.5, where c is the flaw length and ρ is the radius of curvature at the tip of the flaw [68]. Pores with large radii of curvature will diminish the strength of a material less than pores with sharp edges. It follows that spherical voids have the ideal geometry to minimize stress concentration, and for this reason spherical polymethyl methacrylate (PMMA) pore formers are used in this study. Graphite, starches, and other common pore forming agents leave irregular pores that will act as more severe stress concentrators and diminish the strength of the supporting anode material when compared with spherical voids.

$$\sigma_f = \frac{\sigma_o}{2} \sqrt{\frac{\rho}{c}} \quad (5.5)$$

This work explores characterization of porous ceramic electrode scaffolds from commercially available powders. Frequently-used fluorite oxides were selected: 10% gadolinia doped ceria (GDC10) and both 8% and 3% yttria-stabilized zirconia (YSZ8 and YSZ3). Data from dense samples in literature supports an inverse relationship between

the ionic conductivity (σ_i) and the flexural strength (σ_f) of these fluorites, which is depicted in Figure 5.2. Both properties relate to the metal-oxygen bond strength in the lattice: weak bonding allows high oxygen conductivity, but causes low strength. This tradeoff makes it important to understand the strength of these materials with different porosity fractions so that anode materials can be chosen to ensure desired strength at desired porosity. In this work, the strengths of porous GDC10 and YSZ8, cubic fluorites commonly used as electrolytes, as well as YSZ3, a stronger YSZ with tetragonal fluorite structure, are measured. The empirical parameters that relate the flexural strength of the materials to their porosity are determined from the collected data.

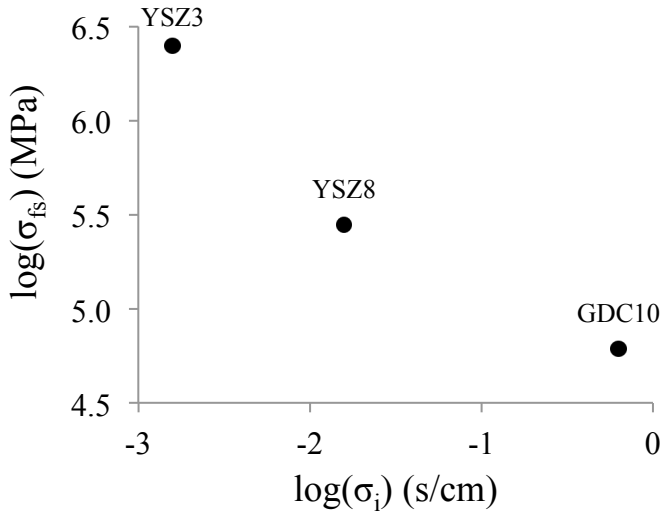


Figure 5.2: Ionic conductivity at 650 °C vs. flexural strength at room temperature of fluorite oxides GDC and YSZ. Data from [1, 63, 69]

Electrical properties of the anodes are measured after the addition of conductive and catalytic materials to the scaffolds. Thermodynamic calculations of the equilibrium PO_2 of the metals used are compared to the effective PO_2 of anode gas environments under H_2 and CH_4 fueling to ensure they remain reduced during SOFC operation.

Calculations are performed for operating temperatures of 300-700 °C at fuel utilizations of 50% to 99%.

5.2 Experimental

5.2.1 Anode Support Fabrication

The ceramic powder (GDC10 from Fuel Cell Materials, YSZ8 and YSZ3 from Tosoh) was ball milled with 0 - 70 vol% PMMA spheres (Soken Chemical, Japan) as pore former, 1 wt% polyvinyl butyral (Tape Casting Warehouse) as binder, and 0.5 wt% Menhaden fish oil (Tape Casting Warehouse) as a dispersant in ethanol for 12 hours. The PMMA diameter was varied from 1.7 to 30 µm in GDC samples with 50 vol% PMMA to investigate the effect of pore size, but 5 µm diameter PMMA was used in all other samples investigated. Each size of PMMA spheres has a very narrow distribution of diameters of < ±5%. Each milled slurry was dried in an oven at 100 °C, loosely ground into an even powder, and pressed at 50 MPa in a uniaxial press (Carver) into 2 mm thick bars. A custom 10 x 30 mm rectangular die was used to give proper geometry for bend test bars. Grinding and pressing pressures were kept low to prevent deformation of the PMMA. Porous GDC scaffolds were also fabricated using a more scalable tape casting procedure for comparison. These scaffolds were prepared by tape casting a slurry of GDC10 and 5 µm diameter PMMA spheres as a pore former using a laboratory-scale tape caster (Pro-Cast, HED International). The slurry rheology was controlled using Menhaden fish oil, polyvinyl butyral, benzyl butyl phthalate (Tape Casting Warehouse) and polyethylene glycol (Fisher Scientific) as plasticizers, and ethanol as solvent. A

volume fraction of 60% PMMA relative to the ceramic was used. The slurry was cast into flexible tapes with thicknesses of 400 μm , and 4 layers were laminated under minimal pressure to give a thickness of 1.6 mm. Bar samples were cut from the tape. Both pressed and tapecast samples were fired with holding steps at 200 $^{\circ}\text{C}$ and 400 $^{\circ}\text{C}$ for 1 hour to remove polymeric components, then sintered at 1450 $^{\circ}\text{C}$ for 4 hours to densify the ceramic matrix while leaving templated pores intact.

Nickel, copper, or cobalt metal was infiltrated into a set of the tapecast GDC anode supports to enhance their electrical conductivity and oxidation catalysis. These transition metals were selected because they reduce at a relatively high PO_2 and have exceptional electronic conductivity at SOFC operating temperatures. A heated 4.5 M solution of metal nitrate was deposited on the anode face until the pores were saturated. The scaffolds were placed in a vacuum chamber to remove any air trapped in pores beneath the solution, then subsequently heated to 400 $^{\circ}\text{C}$ to decompose the nitrate into NiO , CuO , or CoO . This process was repeated several times to achieve the desired metal loading in the anode.

5.3 Characterization

5 . 3 . 1 Microstructure Measurement

The open porosity of the anode supports after final sintering was measured by Archimedes method using a procedure detailed previously [58]. The mass gain after each nitrate decomposition step was recorded, indicating the mass of deposited NiO , CuO , or CoO . The volume percent of the reduced metal in the scaffold was calculated by normalizing to the initial GDC mass and correcting for the density difference. Anode

microstructure was investigated using a Hitachi SU-70 scanning electron microscope after reduction of the metal oxides in hydrogen. Grain and pore sizes were measured using the image processing software FIJI [32]. Specific surface area of the bare and infiltrated GDC scaffolds were tested using BET N₂ adsorption.

5.3.2 Mechanical Properties Measurement

The flexural strengths of sample bars of the GDC10, YSZ3, and YSZ8 were measured using 3-point bend tests. Bars were loaded into a Tinius Olsen H25K-T benchtop universal testing machine and loaded at a rate of 0.1 mm/min until failure. Five samples were tested for each condition to ensure reliable statistical analysis. Flexural strength was determined using Eq. 5.6, where F is force at fracture in Newtons, L is the spacing between the supports in mm, b is width of the sample, and d is its thickness. The strength vs. porosity was fit using Eq 5.4.

$$\sigma_f = \frac{3FL}{2bd^2} \quad (5.6)$$

5.3.3 Electrical Measurements

The conductances of GDC anodes infiltrated with different amounts of metal were evaluated with 4-point probe tests using a Keithley 2400 Sourcemeter. Porous Pt contacts were painted onto the ends of the samples, they were wired with Pt leads, and they were then heated in a furnace. The metal oxides were reduced to conductive metal in a 10% H₂/bal N₂ atmosphere at 700 °C for 1 hour prior to recording resistance values at room temperature. The specific conductance was calculated by normalizing the conductance to the sample geometry, and the connectivity of the percolated network of

metal was determined by normalizing the measured conductance to the intrinsic conductivity of the metal at room temperature.

5.4 Thermodynamic Calculations

To ensure that the metals used in the anodes will not reoxidize during SOFC operation due to the O²⁻ flux through the electrolyte, the PO₂ of the anode atmosphere was compared to the equilibrium PO₂ for NiO, Cu₂O, and CoO reduction at SOFC operating temperatures. Though CuO is deposited during infiltration, the oxide Cu₂O has a lower equilibrium PO₂ and will form first, thus is used for these calculations. The effective PO₂ in the anode atmosphere with CH₄ or H₂ as a fuel was calculated using Cantera, a chemical thermodynamics and kinetics package [36]. The thermodynamic parameters for methane oxidation used were obtained from GRI Mech 3.0 [37], which contains 325 reactions among 53 species. The effective PO₂ was determined as a function of temperature and fuel utilization. Equilibrium PO₂ for metal oxide reduction was determined using an Ellingham diagram [39]. The metals are expected to remain reduced as long as the PO₂ in the anode atmosphere remains lower than the equilibrium PO₂ of the metal oxidation reaction.

5.5 Results and Discussion

5.5.1 Mechanical Strength vs. Porosity

The total volume percent of porosity after sintering introduced in each sample by 5 μm diameter PMMA is plotted in Figure 5.3. Each material has a strong linear fit ($R^2 > 0.99$), indicating that GDC10, YSZ3, and YSZ8 reliably retain porosity matching 85%,

75%, and 67%, respectively, of the initial PMMA volume under identical sintering conditions. Measured grain (d_{grain}) and pore (d_{pore}) diameter for each material are presented in Table 5.1. There is a correlation between d_{grain} and d_{pore} after sintering; larger grains support larger pores. There is no single parameter that clearly dominates pore volume loss, however. GDC10 and YSZ8 have similar grain sizes and pore diameters, but have the largest difference in pore volume loss. YSZ8 has smaller pores and grain sizes after sintering, but has an intermediate value of retained porosity. The slopes observed in Figure 5.3 must therefore be determined by a culmination of several microstructural factors.

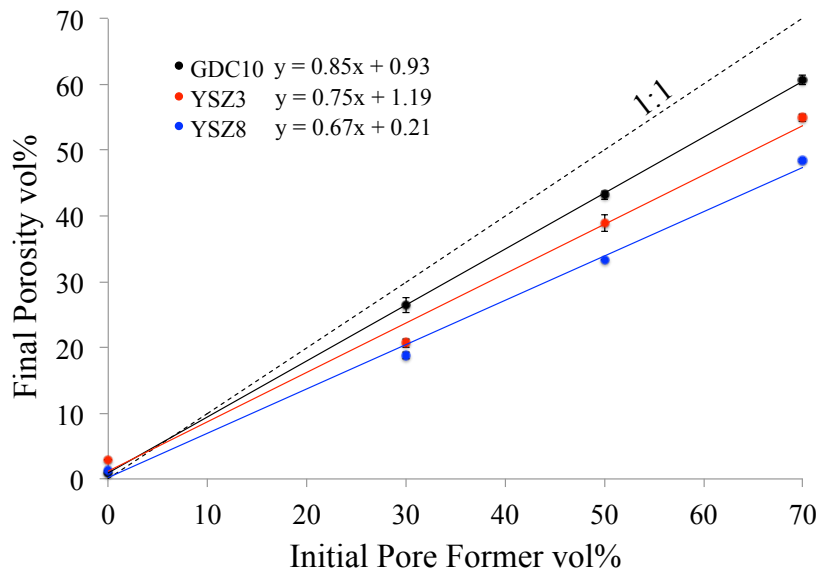


Figure 5.3: Final pore volume percent in sintered samples vs. volume percent of $5\mu\text{m}$ PMMA pore former added to ceramic powder. Dashed line represents a 1:1 relationship. Solid lines are linear fits, with the slope and intercept for each given in the inset equations.

Table 5.1: Measured physical parameters for each set of porous material using 5 μ m PMMA pore former.

Material	d_{pore} (μm)	d_{grain} (μm)	n	Pore:PMMA volume ratio
YSZ3	3.4 \pm 0.2	0.4 \pm 0.1	5.3	0.75
YSZ8	3.8 \pm 0.3	1.3 \pm 0.3	5.7	0.67
GDC10	3.9 \pm 0.1	1.2 \pm 0.4	4.7	0.85

The strength of the tested ceramic samples is plotted in Figure 5.4a for each material at different porosities with 5 μm diameter PMMA as pore former. The empirical fitting parameter, n, from Eq. 4 is given in Table 5.1 and varies from 4.7 – 5.7. Higher n values indicate a greater relative loss of strength with porosity: GDC maintains 15% of its original strength at 40 vol% porosity, while YSZ8 retains only 10% of its dense strength. The observed n parameter has a strong inverse correlation (Figure 5.4b) with the pore volume shrinkage seen in Figure 5.3. This may be because n is an empirical adjustment factor that accounts for pore geometry and other microstructural details that also relate to the pore volume retention. While these correlations are good for the materials and processing studied, more data is needed to evaluate the scope and limitations of the observed relationship.

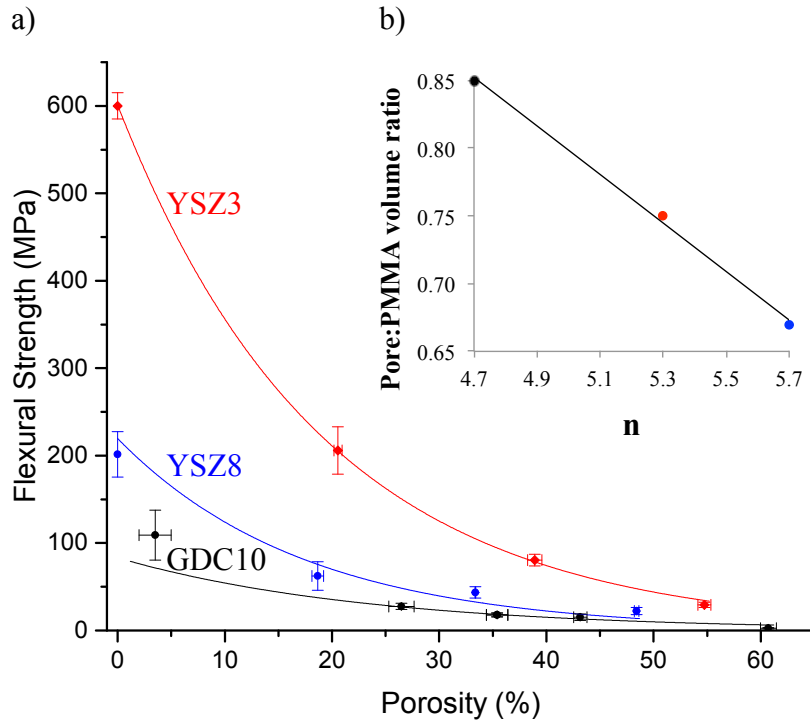


Figure 5.4: a) Flexural Strength vs. Porosity of GDC10, YSZ8 and YSZ3 with 5 μ m PMMA pore former. Solid lines show the fitting of Eq. 4, and Table 5.1 gives empirical fitting parameter, n, determined for each material. b) Inset graph shows the relationship between n and the slopes in Figure 5.3.

The effect of PMMA diameter (d_{PMMA}) on strength in GDC is detailed in Figure 5.5a for samples uniaxially pressed with 50 vol% PMMA. The maximum strength was observed when $d_{\text{PMMA}} = 5 \mu\text{m}$ was used. Microstructural analysis in SEM reveals the reasons for this trend, depicted in Figure 5.6a-d. For $d_{\text{PMMA}} = 1.7 \pm 0.1 \mu\text{m}$ (Figure 5.6a & d), the smallest size used, the pore former size is similar to the sintered grain size of the GDC ($1.4 \pm 0.4 \mu\text{m}$), so the spherical structure of the porosity is lost as GDC grains grow during sintering. The smaller resulting pores act as more severe stress concentrators with a smaller radius of curvature (Figure 5.5b & c). When $d_{\text{PMMA}} = 5 \pm 0.2 \mu\text{m}$ is used, the spherical voids with large radius of curvature are maintained (Figure 5.6b & d).

When a much larger d_{PMMA} is used ($29 \pm 0.7 \mu\text{m}$), the loose GDC at the walls of the pores partially collapses between polymer burnout and GDC sintering, leaving a reduced pore diameter (Figure 5.5b & c) and introducing additional stress concentrators to the microstructure (Figure 5.6e).

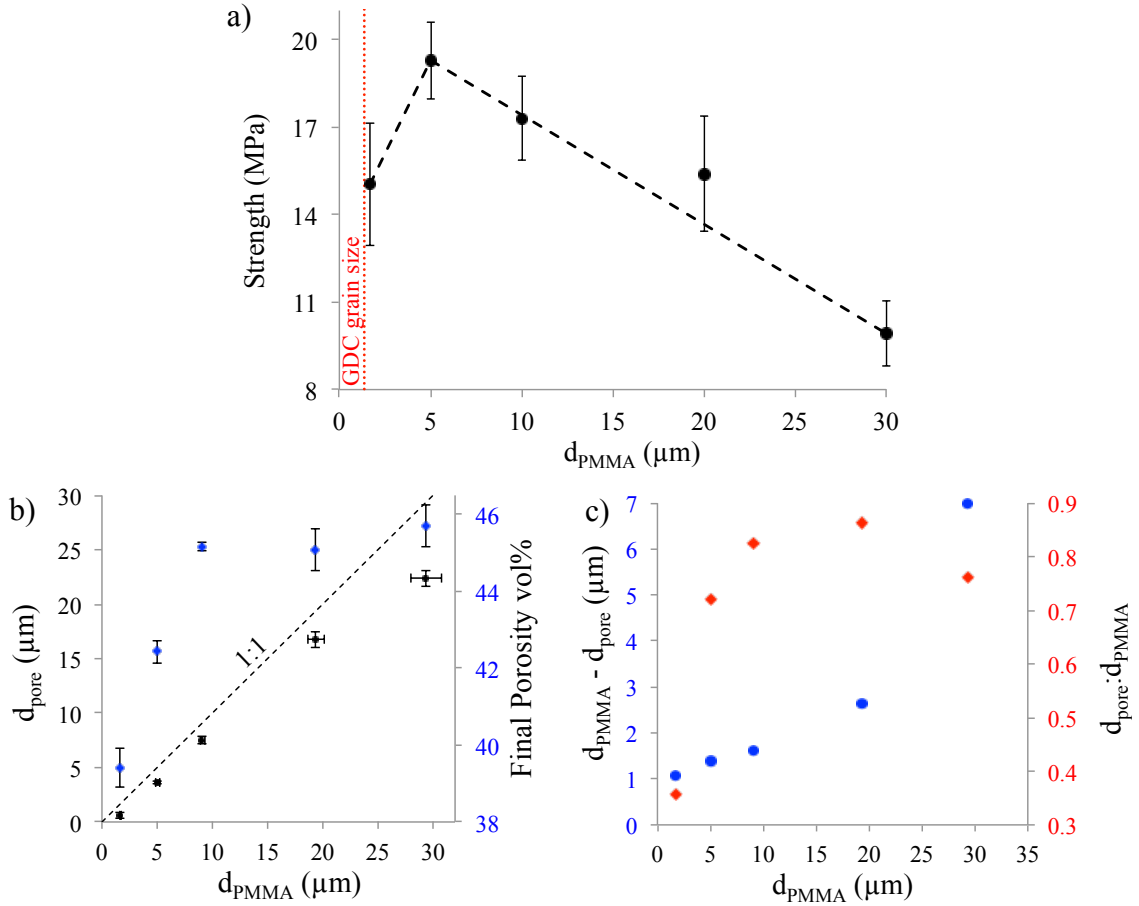


Figure 5.5: a) GDC scaffold strength vs. PMMA pore former diameter for a 50 vol% PMMA addition. Dashed black lines are a guide to the eye. Red dotted line indicated sintered GDC grain size. b) Resulting pore diameter (black) and volume percent porosity (blue) for a 50 vol% addition of different diameter PMMA. Dashed line shows a 1:1 $d_{\text{pore}}:d_{\text{PMMA}}$ relationship. c) Difference between pore and PMMA diameters (blue) and ratio between pore size and starting PMMA diameter (red).

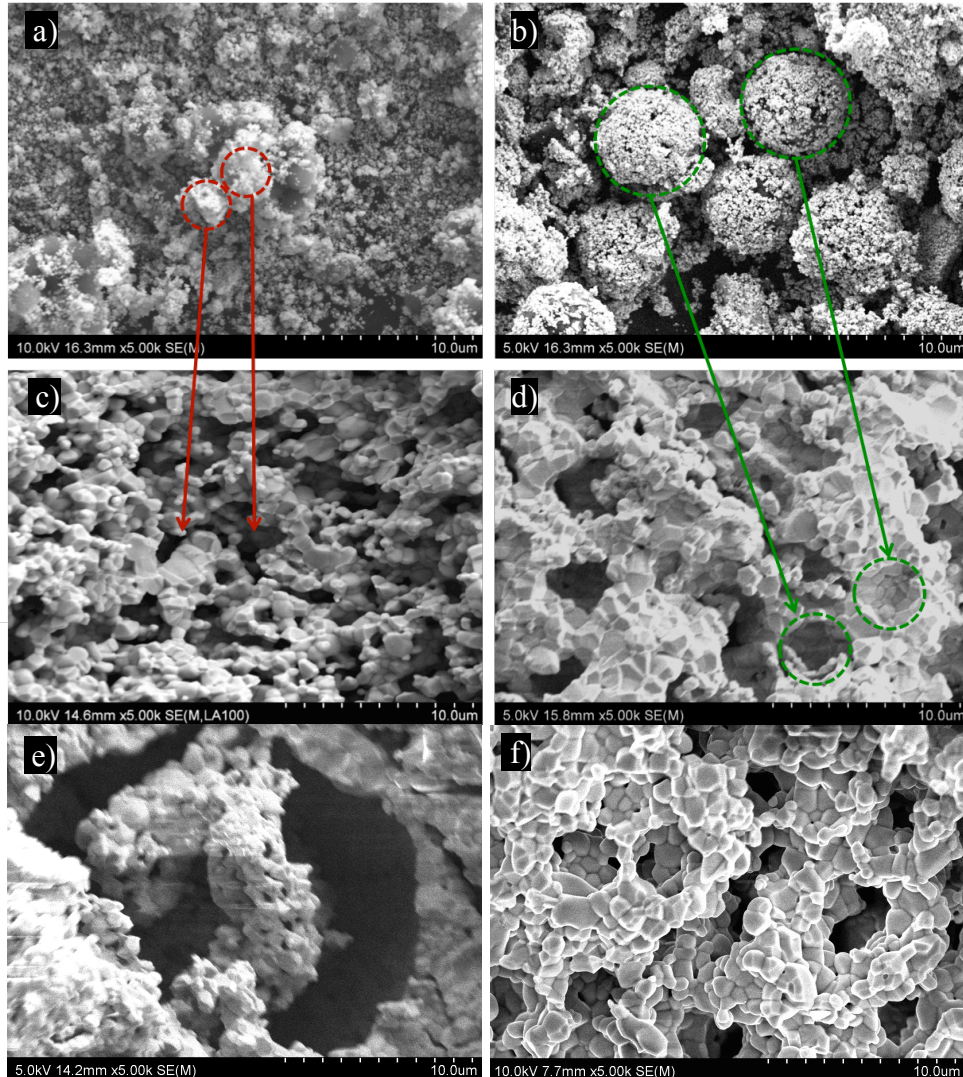


Figure 5.6: Unfired GDC powder and resulting sintered scaffolds with 50 vol% PMMA added. a) GDC milled with $1.7 \mu\text{m}$ PMMA, b) GDC milled with $5 \mu\text{m}$ PMMA, c) pressed and sintered GDC using $d_{\text{PMMA}} = 1.7 \mu\text{m}$, d) pressed and sintered GDC using $d_{\text{PMMA}} = 5 \mu\text{m}$, e) pressed and sintered GDC using $d_{\text{PMMA}} = 29 \mu\text{m}$, f) tapecast and sintered GDC using $d_{\text{PMMA}} = 5 \mu\text{m}$. The relationship between ceramic-coated PMMA spheres in a and b and the resulting pores in c and d are outlined and emphasized with arrows.

The effect of processing method on strength is shown in Figure 5.7. GDC bars with 50% $5 \mu\text{m}$ PMMA prepared by uniaxial pressing are significantly weaker than those formed by tapecasting, which have an n value of only 2.9. The difference relates to the better green body density resulting from tapecasting [70] that gives the scaffold a

smoother microstructure (Figure 5.6f) compared to the pressed scaffold (Figure 5.6d). This suggests that the strength of porous ceramics anodes is influenced more heavily by processing than by material choice. This is an important consideration; GDC has greater catalytic activity for the oxidation of fuel and coke [45, 59], so is beneficial as a catalytic support if it can be made durable enough.

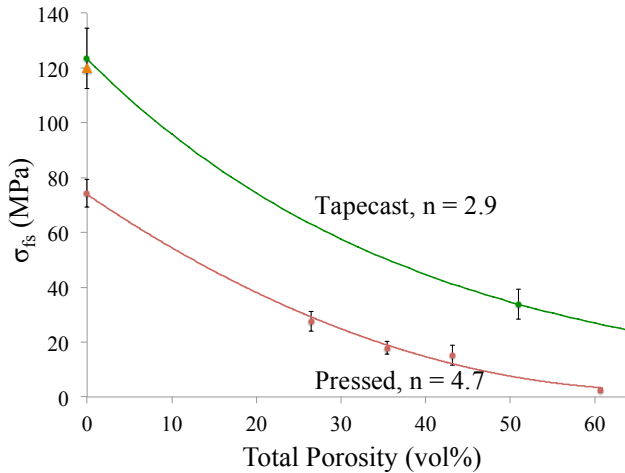


Figure 5.7: Effect of processing on porous GDC scaffold strength using 5 μm PMMA pore former. Tapecasting (green) gives higher strength than uniaxial pressing (red). Orange triangle represents literature value from Atkinson [66].

5.5.2 Infiltrated Electronic Conductor/Catalyst

The volume loading of metal after Ni, Cu, and Co infiltrations is plotted in Figure 5.8. The deposition rate of Ni and Cu from a nitrate solution is relatively consistent, but Co deposits ~20% more metal volume per infiltration step. The loading rate decreases as the pores of the sample are filled and less nitrate solution can penetrate them in subsequent steps. Since the conductive and catalytic metal is constrained to the surfaces of the porous ceramic support, less total metal loading is required than in randomly-mixed cermet anodes where >30% is required for percolation [59]. Reports in

other porous ceramics suggest that approximately 10 vol% conductive metal is required for good percolation [65], so metal loading volumes in that range were selected.

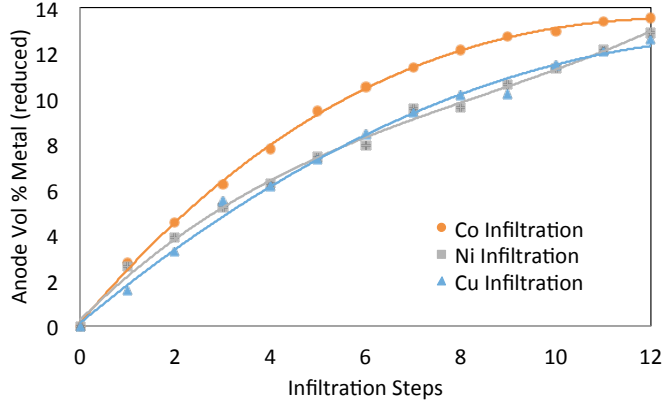


Figure 5.8: Volume percent of metal (Ni, Cu, or Co) in a porous GDC scaffold after each deposition and decomposition of the metal nitrate solution. Solid lines are a guide to the eye.

Microstructural analysis in SEM reveals that the morphology of metal deposition is not identical between the Ni, Cu, and Co (Figure 5.9), likely due to differences in wetting properties of the nitrates and the surface energy of the metals in a reducing atmosphere. The volume fraction of metal in each micrograph, calculated by the mass gain, is listed in Table 1. Ni initially forms small, angular Ni crystals within 4 infiltrations that coalesce into an interconnected network of rounded metal particles within 8 infiltrations. Cu forms rounded deposits that are difficult to visually differentiate from the underlying GDC scaffold, though clearly fill the large spherical voids in the scaffold. Co forms a more conformal layer on the pore walls, nearly saturating the GDC surface after 12 infiltrations despite only filling only 13.5 vol% of the scaffold. To achieve this extent of surface wetting, the surface energy of Co must be lower than that of GDC, according to the Young-Laplace equation [71]. Presumably Ni

and Cu must have higher surface energies than Co, which drives their dewetting into particles on the GDC surface. This effect is counterintuitive because the surface energy of bulk Co [72] is higher compared to Cu and Ni [73] in an inert atmosphere, but the trend must reverse under the reducing conditions in the H₂ atmosphere. Elsewhere, solid-state dewetting has been used to pattern Pt electrodes on YSZ substrates [74], but limited information is available about the relative surface and interfacial energies of anode materials to predict their behavior. Additional research on this topic by the SOFC community is necessary.

Specific surface area (SSA) analysis by BET revealed that the morphology of the deposited metal has a pronounced effect. A sintered GDC scaffold with 51 vol% open porosity has a SSA of 0.264 m²/g. Deposition of 13.5 vol% Co reduced the SSA to 30% of that value, 0.078 m²/g, as a consequence of its conformal deposition. Cu and Ni increased the SSA to 269% and 292%, respectively, of that of the bare scaffold, which correlates with the microstructures observed in Figure 5.9. The enhanced surface area and smaller particle size for Ni and Cu increase the density of one-dimensional TPB sites that can exist along the interface of the metal, ceramic, and gas phase. The sheets of Co have a lower surface area to volume ratio and will have a lower density of TPB sites, limiting the catalytic activity of Co infiltrated anodes.

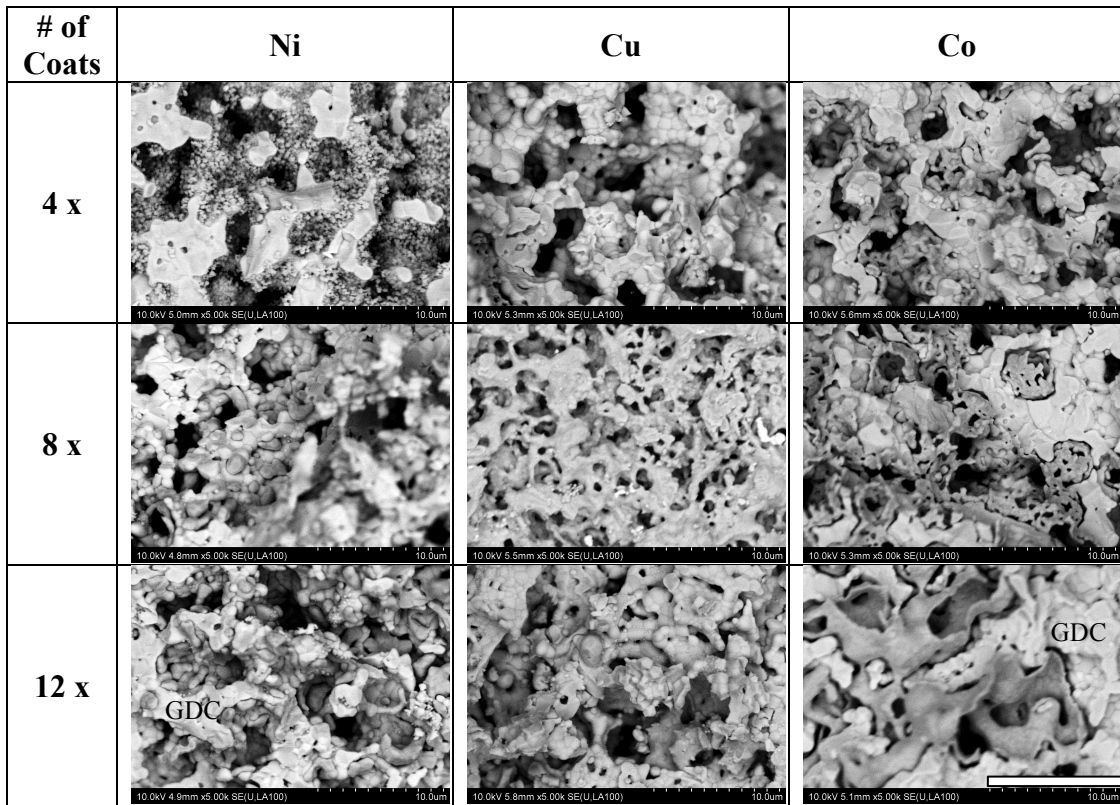


Figure 5.9: SEM micrographs of the metal-infiltrated GDC scaffolds after 4, 8, and 12 infiltrations showing the distribution of metal (darker deposits) on the GDC (lighter scaffold) after reduction in 10% H₂/N₂. Scale bar is 10 μm.

The specific electronic conductance of the infiltrated scaffolds is affected by the microstructure of the completed electrode, as documented in Figure 5.10a. The volume percent loading of metal and specific conductance are given in Table 5.2. The resistance of each reduced sample at room temperature after 4 infiltrations is > 1MΩ, indicating that none of the metals form a percolated conductive network within 4 infiltration steps (6.2-7.8 vol% metal). All metals contributed measurable conductivity after 8 infiltrations, however, corresponding to 9.6- 12.1 vol% metal loading. Copper infiltrated electrodes have the highest specific conductance overall due to the higher

intrinsic conductivity of Cu. The Ni infiltrated anodes have lower specific conductance than either Cu or Co.

Table 5.2: Electronic Conductance of Reduced, Infiltrated GDC Electrodes at Room Temperature

Infiltrated Metal	# Infiltrations	Resulting Vol% Metal	Specific Conductance (S/cm)
Ni	4	6.3	<1
	8	9.6	140
	12	12.9	310
Cu	4	6.2	<1
	8	10.1	810
	12	12.6	1600
Co	4	7.8	<1
	8	12.1	480
	12	13.5	770

To understand how well the metal networks in each scaffold are percolated, the measured conductance is normalized to the intrinsic conductivity of each metal in Figure 5.10b. Literature values for the conductivity of bulk Ni, Cu, and Co metal from 0 - 650 °C are plotted in Figure 5.1. The resulting ratio gives insight into the effect of microstructure on anode conductance. The Co infiltrated GDC has the highest ratio, thus the best percolation. This effect indicates that the enhanced conformality of the Co network observed in Figure 5.9 is a geometry that is less tortuous with fewer resistive necking points than the overlapping islands of deposited Cu or Ni, thus the conductance is improved for the same volume of metal within the anode.

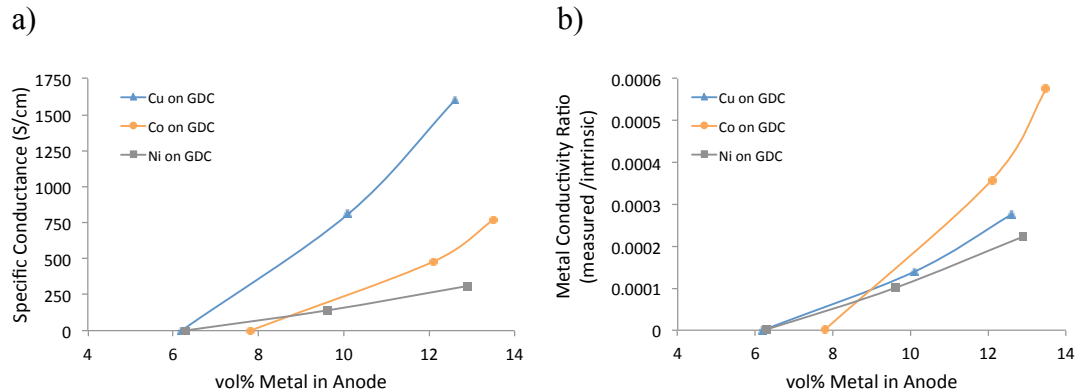


Figure 5.10: a) Specific conductance of infiltrated GDC vs. volume percent loading of metal. b) Ratio of measured conductance to intrinsic conductivity for each metal vs. volume percent metal. Solid lines are a guide to the eye.

5.5.3 Calculated Reoxidation during SOFC Operation

The anode gas environment must remain at a PO_2 lower than the PO_2 of the metal-metal oxide equilibrium in the anode to prevent its reoxidation. Calculated values are presented in Table 5.3. Even at the increased PO_2 in the anode environment at 99% fuel utilization, Ni and Cu remain as reduced metals for both H_2 and CH_4 fueling conditions. There will be a driving force for Co to reoxidize at each temperature, however, at 99% fuel utilization for both fuels and at >50% fuel utilization at 300 °C in CH_4 . The electrical conductivity of CoO is 10 orders of magnitude lower than metallic Co, thus reoxidation will cause a catastrophic increase in anode Ohmic resistance. This evidence supports the use of Cu or Ni as current collector and catalyst materials, and indicates that Co should be avoided for operation between 300-700 °C. This is an important realization because Co and metals with even lower equilibrium PO_2 such as Fe or Sn have been used in SOFC anodes to prevent coke formation [28, 45, 75-77], but

these anodes will not be stable in an SOFC with the high fuel utilization necessary for high efficiency.

Table 5.3: Equilibrium PO_2 below which the metals stay reduced compared to the calculated equivalent PO_2 of SOFC fuels at 50% and 99% fuel utilization (FU).

Temp. (°C)	$2\text{Cu} + \text{O} \leftrightarrow \text{Cu}_2\text{O}$	$\text{Ni} + \text{O} \leftrightarrow \text{NiO}$	$\text{Co} + \text{O} \leftrightarrow \text{CoO}$	H ₂ Equivalent PO_2		CH ₄ Equivalent PO_2	
	Equilibrium PO_2 log(atm)	Equilibrium PO_2 log(atm)	Equilibrium PO_2 log(atm)	$U_f=50\%$ log(atm)	$U_f=99\%$ log(atm)	$U_f=50\%$ log(atm)	$U_f=99\%$ log(atm)
300	-23.3	-34.0	-36.7	-39.3	-35.3	-36.7	-35.5
500	-15.3	-22.8	-24.9	-27.7	-23.7	-27.4	-24.2
700	-10.6	-16.3	-18.2	-20.8	-16.8	-21.5	-17.2

5.6 Conclusions

The mechanical strength of porous GDC10, YSZ8, and YSZ3 was studied, and the electrical and morphological properties of porous GDC infiltrated with different metallic conductors were characterized. The burnout of PMMA spheres gives highly-predictable pore volume, with each material having a characteristic ratio of retained pore volume to starting PMMA volume. The strength of each material decreases to 10-15% of its dense value when 40 vol% porosity is introduced. GDC10 has the lowest n value, thus is least affected by porosity, while YSZ8 has the highest. Pores from 5 μm PMMA spheres give the strongest anode; larger or smaller pore sizes weaken the scaffolds. Tape casting significantly improves the strength of GDC compared to uniaxial pressing. Together, these trends demonstrate that the processing and microstructure of porous ceramic anodes can have greater impact than material choice.

All metals required more than 4 infiltration steps to create a conductive network through 51% porous GDC scaffolds. Ni and Cu infiltrations exhibit a similar

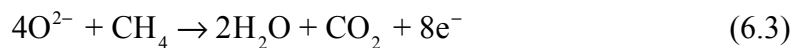
microstructure, but the Cu infiltrated electrode has ~4x higher electronic conductivity, matching its intrinsic conductivity compared to Ni. Co deposits in a more conformal layer in the anode, giving it twice the conductivity of Ni at similar metal loading, despite having the same intrinsic conductivity. Unfortunately, the conformal Co coating lowers the SSA of the electrode to only 30% of that of the original scaffold, so fewer catalytic sites are created compared to Cu and Ni deposition which increase the SSA by 170% and 190%, respectively. Thermodynamic analysis of the reoxidation of the conductive metals used in the anodes reveals that Ni and Cu remain reduced, even at 99% fuel utilization, in both H₂ and CH₄ fueling conditions, while Co will reoxidize under several conditions and should be avoided.

Chapter 6: Performance of Ceramic Anode Supported SOFCs

6.1 Introduction:

Solid oxide fuel cells (SOFCs) have attracted significant interest as efficient energy conversion devices, especially amidst abundant natural gas supplies in conjunction with an increased concern over CO₂ emission and its effects on climate change [78-80]. With the greater efficiency of these solid-state devices over conventional turbine-based natural gas plants that suffer from Carnot efficiency limitations and require moving parts, SOFCs release less CO₂ per kilowatt of electricity generated than traditional energy conversion technologies. Furthermore, their eminently scalable nature makes them ideal for strategic distributed generation of kW to MW-range power plants for a more robust, secure, and adaptive electricity grid, while typical natural gas plants must be > 10 MW to achieve acceptable efficiency.

SOFCs combine oxygen ions reduced from air at a cathode (6.1) with a supplied fuel at the triple phase boundary (TPB) between the anode, electrolyte, and gaseous fuel. Both hydrogen (6.2) and hydrocarbons such as methane (6.3) can be used.



Significant progress has been made in lowering the operating temperature of SOFCs from 900 °C to \leq 600 °C by developing more conductive electrolytes [1, 81-83]. The low operating temperature has the benefit of extending cell lifetime and reducing the balance-of-plant cost. Concurrently, there has been significant development of SOFCs for operating on hydrocarbon fuels that are already widely available: natural gas, gasoline, and diesel. The primary challenge in hydrocarbon fueled SOFCs is to prevent solid carbon deposition, or coking, in the porous anode [29, 42, 43, 50]. Most development of hydrocarbon fueled SOFCs has been at high temperature (700-900°C) due to the low conductivity of the conventional yttria-stabilized zirconia (YSZ) electrolytes used. Unfortunately, results of anode effectiveness in hydrocarbons above 700 °C are not relevant at lower temperatures, since the dominant coking reaction transitions from endothermic hydrocarbon cracking (6.4) to exothermic CO disproportionation (6.5) below that temperature. Anodes for hydrocarbon-fueled SOFCs operating at low temperatures have different requirements due to the different coking mechanism, and there are significantly fewer studies that address these conditions. This work investigates SOFC anodes tailored for low-temperature operation on direct methane.

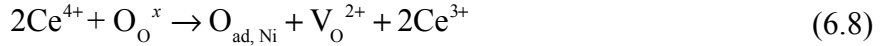


We previously demonstrated the feasibility of operating an SOFC with mixed Ni-GDC cermet anodes for over 500 hours on reformed liquid fuels at 550 °C, relying on

external reforming of the fuel via both steam reforming and partial oxidation with air to prevent coking, and resulting in only a 15% decrease in power density compared to using H₂ fuel [57]. Though these results are promising, the added equipment required for external reforming is undesirable due to its extra cost and size and the parasitic load required to heat and vaporize water used in steam reforming. Direct internal reforming is ideal, but difficult to achieve without forming deleterious solid carbon phases at Ni surfaces. Ni is the best catalyst for fuel oxidation in SOFCs according to experimental and density functional theory (DFT) results by Rossmieisl and Bessler [21] and is an exceptional electronic conductor at SOFC operating temperatures ($>10^5$ S/cm² at 650 °C [20]), so it is the most frequently used electronic conductor and catalyst in SOFC anodes. Unfortunately, it also catalyzes the formation of solid carbon. Alternative conductive metals such as Cu have been investigated in anodes, but fuel oxidation catalysis and carbon formation catalysis are both inhibited when using Cu, so stable performance comes at the cost of low power density [40, 84]. To achieve high power density and stable performance on hydrocarbons simultaneously, it is necessary to engineer electrodes that address the coking and oxidation pathways to prevent carbon deposition but encourage fuel oxidation.

Several oxidation pathways exist for hydrocarbon fuel oxidation in SOFCs. In the gas phase, partial oxidation (6.6) and water gas shift (6.7) reactions are responsible for internal reforming of the fuel in the anode. The surface of the material near TPBs also plays a vital role in fuel oxidation. At the TPB, oxygen spillover from the surface of the metal oxide to the metal promotes oxidation of the fuel. Oxygen spillover is enhanced when a metal like Ni is supported on a multivalent metal oxide like CeO₂ [85, 86]. The

Ce^{4+} cations can reduce to Ce^{3+} and form oxygen vacancies to compensate, which allows O^{2-} species at the surface of the CeO_2 to transfer onto the metal (6.8) where the fuel then adsorbs and is oxidized. Rossmeisl and Bessler find that oxygen spillover is the dominant reaction pathway for fuel oxidation in SOFCs [21]. Shin and McIntosh, using isotopically labeled H_2 , found that spillover on Ni supported on GDC is significantly faster than on Ni supported on YSZ, and surface exchange takes place only on the metal surface [84]. The enhanced rate of spillover for Ni on GDC suggests an ideal anode will consist of Ni particles constrained to a GDC surface to maximize the rate of fuel oxidation via oxygen spillover.



At the desired operation temperatures, $\leq 650^\circ\text{C}$, solid carbon deposits form when multiple CO species adsorb on the surface of metal in the anode and undergo disproportionation (6.5). CO adsorption is highly favorable on Ni surfaces [87], which leads to a faster rate of carbon deposition. Fu et al. find through Monte Carlo simulations that CO at Ni surfaces is oxidized only via oxygen spillover from a supporting metal oxide [88]. Promoting the oxygen spillover and coverage at Ni surfaces is likely help oxidize the CO or block sites where disproportionation can occur, preventing carbon deposition in the anode.

This work demonstrates an approach for enabling lower temperature operation of SOFCs on methane fuel by engineering triple phase boundaries capable of oxygen spillover and subsequent fuel oxygen throughout the bulk of the anode, while also maintaining adequate electronic conductivity and minimal pore tortuosity necessary for fuel diffusion. A scaffold of GDC is used to support the electrolyte, and a small amount of submicron particles of Ni are deposited within its pores to provide electronic conductivity and catalysis.

Similar studies by Gorte and colleagues have used transition metals on YSZ scaffolds [89, 90] which, as mentioned previously, have significantly less catalytic activity than Ni supported on GDC [84, 91, 92]. Studies using doped ceria scaffolds have been investigated, but often using thick electrolyte supported geometries that confine them to high temperature operation or very low O²⁻ current densities at temperatures \leq 650 °C [93-95]. Use of a YSZ electrolyte with GDC anodes, apart from requiring a higher operating temperature than a GDC electrolyte, causes interfacial issues due to thermal expansion coefficient (TEC) mismatch and the formation of a deleterious solid solution at the anode-electrolyte interface that increase Ohmic and charge transfer resistance [96]. An anode with a thickness of 100's of μm is fundamentally different from a thin anode from a reforming standpoint, since the steady-state concentration gradient of products and reactants in the anode changes, and can be useful for internal reforming of a hydrocarbon fuel [51, 97]. A thin GDC electrolyte supported on a Ni infiltrated GDC scaffold anode offers an ideal combination of having a large number of highly catalytic sites for hydrocarbon fuel reforming and oxidation, having low electrolyte resistance that enables lower temperature operation, and having perfect TEC

match at the anode-electrolyte interface. Cells of this type are used in this study to verify this hypothesis.

Many variables are encountered during SOFC processing, so it is often difficult to directly compare performance of anode types in literature if there are significant variations in electrolyte or cathode thickness, electronic contact pastes, or sintering treatments. To that end, this study standardizes the contact, electrolyte, and cathode materials and thicknesses to provide a more direct comparison of the anode properties in a full cell. While symmetric cells allow anode performance to be more completely isolated, they lack a continuous oxygen source, so studies in hydrocarbon fuels will inevitably suffer from carbon deposition. For this reason, full cells are required for long-term studies. No study to date, to our knowledge, has compared infiltrated anodes to cermets in anode-supported SOFCs this directly.

6.2 Experimental:

6.2.1 Fabrication

Porous GDC scaffolds were prepared by tape casting a slurry of GDC (Fuel Cell Materials) and PMMA spheres (Soken Chemical, Japan) as a sacrificial pore former using a tape caster (Pro-Cast, HED International). The slurry rheology was controlled using Menhaden fish oil (Tape Casting Warehouse) as a dispersant, polyvinyl butyral (Tape Casting Warehouse) as binder, benzyl butyl phthalate (Tape Casting Warehouse) and polyethylene glycol (Fisher Scientific) as plasticizers, and ethanol as solvent. Two final porosity values were targeted: a lower final porosity that will match the ~25%

porosity in a conventional Ni-GDC cermet, and a higher porosity to improve gas transport in the anode. The volume fraction of 5 μm diameter PMMA spheres relative to GDC was varied from 50 vol% to 60 vol% in order to control the porosity in the fired scaffold. The slurry was cast into flexible tapes with thicknesses of 300 μm . Discs were cut from the tape and fired at 1000 °C for 4 hours in order to burn off the binder and pore former polymers and loosely neck the GDC particles to form a green body that could be handled. A dense 20 μm electrolyte layer was deposited onto the porous substrate by colloidal deposition of GDC suspended in ethanol with 2 wt% PVB and firing at 1450 °C for 4 hours. Cathodes composed of an equal volume fraction of $\text{La}_{0.6}\text{Sr}_{0.4}\text{Co}_{0.2}\text{Fe}_{0.8}\text{O}_{3-\delta}$ (LSCF) (Praxair) and GDC (Fuel Cell Materials) were screen printed onto the electrolyte and fired at 1100 °C for 1 hour.

Nickel metal was infiltrated into the porous GDC anode supports to enhance electrical conductivity and oxidation catalysis. A warmed 4.5 M solution of nickel nitrate was deposited on the anode face until the pores were saturated. The cells were placed in a vacuum chamber to remove air trapped at the electrolyte interface, then subsequently heated to 400 °C to decompose the nitrate into NiO. This process was repeated to incorporate approximately 12 vol% Ni metal into the anode, calculated from the mass of NiO deposited.

SOFCS with 300 μm thick Ni-GDC cermet anodes were fabricated according to a procedure we have detailed previously [57]. The electrolyte and cathode are identical in processing and final thickness to those of the scaffold cells developed for this investigation so that their effect on performance is normalized. Any difference in cell performance can be attributed to the anode supports.

6.2.2 Cell Characterization

The open porosity of the anode supports after final sintering was measured using Archimedes method in ethanol to ensure full penetration of the porosity. A full description of the method is given in previous work [58]. Porosity measurements were normalized to the mass of the anode support by subtracting the electrolyte and cathode mass. The mass gain after each nickel nitrate decomposition step was recorded and the volume percent of the reduced nickel was calculated. The volume percent loading of NiO or Ni metal in the anodes was determined based on the measured NiO mass (W_{NiO}) gained by the anode and the initial porosity of the GDC scaffold (P_{GDC}), determined by Archimedes method, using Equations 6.9 & 6.10. Note that the pore volume has no mass, and the GDC mass (W_{GDC}) remains constant while NiO is added.

$$NiO \text{ vol\%} = \frac{W_{NiO}}{\rho_{NiO}} \cdot \frac{\rho_{GDC}}{W_{GDC}} \cdot (1 - P_{GDC}) \quad (6.9)$$

$$Ni \text{ vol\%} = \frac{W_{NiO}}{\rho_{Ni}} \cdot \frac{M_{Ni}}{M_{NiO}} \cdot \frac{\rho_{GDC}}{W_{GDC}} \cdot (1 - P_{GDC}) \quad (6.10)$$

Following many models in literature [98-100], the surface coverage and TPB length were estimated based on geometric measurements of the ceramic and metal phases. The surface coverage of GDC by Ni was calculated using Equation 6.11, using the surface area of the GDC (A_{GDC}) determined by BET, the volume of Ni infiltrated (V_{Ni}), and the volume (V_P) and interfacial area (A_P) of the Ni particles being deposited.

Roughly hemispherical Ni deposits with radius r_p , which is in agreement with the deposition observed, as well as being used by Sugihara et al for similar electrodes [98].

Assuming the overlap of Ni particles is minimal, the triple phase boundary (TPB) density can be estimated per volume of Ni (Equation 6.12) or per volume of anode (Equation 6.13). If surface coverage is too great, a majority of Ni deposits overlap and consequentially the TPB density will be diminished.

$$\lambda_{Ni/GDC} = \frac{A_p}{A_{GDC}} \cdot \frac{V_{Ni}}{V_p} \quad (6.11)$$

$$\rho_{TPB, Ni} = \frac{2\pi r_p}{V_p} \quad (6.12)$$

$$\rho_{TPB, Anode} = \frac{V_{Ni}}{V_p} \frac{2\pi r_p}{V_{GDC} + V_p} \quad (6.13)$$

A custom-built fuel cell testing chamber was used for electrochemical characterization of the SOFCs, as previously described [57]. Button cells 25 mm in diameter were attached to an alumina tube using Ceramabond 571 sealant (Aremco). Anode contacts were attached with silver paste (Fuel Cell Materials) and gold wire (Alfa Aesar) to ensure the catalytic activity of the anode current collector has negligible effect on the cell performance, and cathode contacts were attached with platinum paste (Heraeus) and gold wire. After reducing the NiO in the anode to Ni metal in flowing H₂ for several hours, electrochemical tests were performed using a Solartron 1470E galvanostat with attached Solartron 1455 FRA cards. Galvanic sweeps were performed at

a scan rate of 10 mA/s at 650 °C using 30 ccm 3% wet H₂ as a fuel and excess air at the cathode as oxidant. AC electrochemical impedance was measured at OCV with a 50 mV perturbation from 100 kHz to 10 mHz several minutes after each IV test. The resulting Nyquist and Bode plots were fit to a model circuit using ZSimpWin 3.5 (EChem Software). After reducing the temperature to 600 °C and stable performance was observed in H₂, long-term potentiostatic tests were performed at 0.4 V with 15 ccm 3% wet CH₄ fuel to determine the stability of the anodes in hydrocarbon fuel. A smaller fuel flowrate was used since one mole of CH₄ requires 4 times greater O²⁻ flux to fully oxidize than one mole of H₂, so less flow is required. Upon completion of a long-term test, the cell was rapidly cooled in N₂ to preserve the microstructure and any coke deposits that formed.

Scanning electron microscopy (SEM) and energy dispersive x-ray spectroscopy (EDS) analysis was performed on reduced cells before and after electrochemical testing to determine microstructure and extent of carbon deposition on the anodes. Cells were fractured to expose representative cross sections of active areas in the device. Distributions of the grain and pore sizes were measured from the collected micrographs using the image processing software FIJI [32].

6.2.3 Thermodynamic Equilibrium Calculations

The conditions for coke formation while using CH₄ as a fuel were calculated using Cantera, the chemical thermodynamics and kinetics package [36]. The thermodynamic parameters used for methane oxidation are from GRI Mech 3.0 [37], which contains 325 reactions among 53 species. Equilibrium concentrations of C(s) were

calculated as a function of temperature and fuel utilization. The parameters for graphite were used for all C(s) species because it is the most thermodynamically favorable species of solid carbon during SOFC operation at these temperatures. Amorphous carbon or carbon nanofibers are energetically unfavorable, as confirmed by both theory and experiments [47, 48].

6.3 Results & Discussion:

6.3.1 Microstructure

The NiO-GDC cermet anode had 4.7 vol% closed porosity and negligible accessible porosity after sintering, but formed 25.3 vol% open porosity upon reduction of NiO to Ni in H₂. After binder burnout and subsequent sintering of the electrolyte, the GDC scaffold anodes with 50 and 60 vol% PMMA in their slurry have a total porosity of 39.9 and 54.3 vol%, respectively, measured by Archimedes method before the NiO was infiltrated. These anodes will be identified as GS40 and GS54, respectively, in the following sections. Nearly all of the pores in the GDC were open to atmosphere; closed porosity accounted for <1 vol% of the total in each case. The spherical shape of the PMMA is well preserved in the resulting porosity, with an average pore diameter of 3.3 ± 0.3 μm in GS40 and 3.5 ± 0.3 μm in GS54.

The Ni impregnated into the pores in the GDC scaffolds amounted to 12.0 ± 0.3 vol%, calculated after reduction for both cells. An example of the weight percent and volume percent gain per infiltration step are given in Figure 6.1 for the GS40 anode. The cermet anodes consisted of 36.3 vol% Ni after reduction, over 300% more metal per

volume than in the scaffold anodes. The remaining porosity in GS40 after infiltration and reduction is similar to that in the cermet anode, so the influence of pore morphology on gas diffusion can be compared for a fixed porosity value. The remaining porosity of GS54 is >50% greater than that in GS40, which is likely to cause a difference in concentration polarization (R_{MT}) observed in those two anodes. A summary of the Ni, GDC, and pore phases in each anode is presented in Table 6.1.

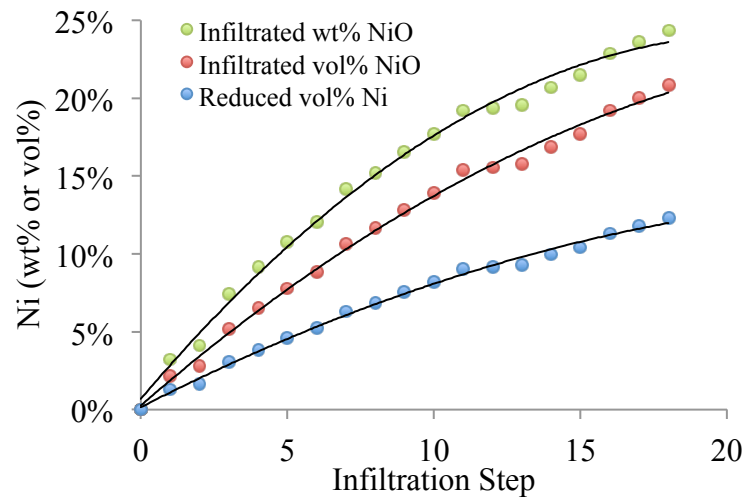


Figure 6.1: Volume percent Ni metal loading after each Ni nitrate infiltration into the porous GDC anode scaffold for GS54. Lines are to guide the eye.

Table 6.1: Volume fraction of Ni, GDC, and pore phases and GDC electrolyte thickness in reduced anodes

	GS40	GS54	Cermet
As Sintered Porosity (vol%)	39.9	54.3	4.7
Final Porosity (vol%)	27.6	42.6	25.3
Ni (vol%)	12.3	11.7	36.3
GDC (vol%)	60.1	45.7	38.4
Electrolyte Thickness (μm)	19.6 ± 1.5	20.4 ± 1.5	21.9 ± 0.9

A comparison of the cross section of the cells is shown in Figure 6.2. Despite the different anode supports used, the morphology and thickness of the electrolyte and cathode in each cell are similar, with the cermet, GS40, and GS40 anode cells having a $21.9 \pm .9 \mu\text{m}$, $20.4 \pm 1.5 \mu\text{m}$, and $19.6 \pm 0.5 \mu\text{m}$ thick GDC electrolyte, respectively. The electrolyte contribution to cell performance can be assumed to be nearly identical in each test. Differences in cell performance in this study can only be a result of the anodes and their interfaces with the electrolyte.

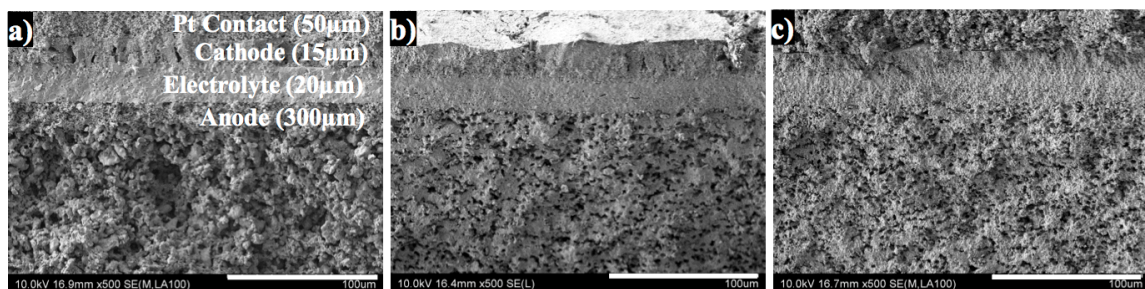


Figure 6.2. Comparative micrographs of SOFCs fabricated with identical GDC electrolytes and LSCF-GDC cathodes, but different anode supports: a) 50:50 vol% Ni-GDC cermet anode b) Ni infiltrated scaffold from 50:50 vol% GDC-PMMA (GS40) c) Ni infiltrated scaffold from 40:60 vol% GDC-PMMA (GS54).

The differences in structure of the anode supports are shown in greater detail in Figure 6.3. The Ni particles in the cermet anode are several microns in diameter and randomly intermixed with GDC particles, while GS40 and GS54 have visible continuity of the supporting GDC phase and have submicron Ni particles decorating the pore walls. A summary of the size of pores and Ni deposits in the anodes determined by image analysis is presented in Table 6.2. The larger diameter particles in the cermet inherently create less TPB length per volume of Ni metal than the smaller particles that are confined to the GDC surface in GS40 and GS54. A comparison of estimated TPB length is included in Table 6.2 indicating that the scaffolds may have >3000% as much TPB length

per Ni volume than a cermet anode. These values agree with TPB densities in comparable anodes measured directly using FIB-SEM or nanoCT [56, 101-104]. Furthermore, due to the conformal nature of the Ni deposits, the total Ni coverage of the GDC surface is calculated to be 42% for GS54 and 62% for GS40. These high surface coverage values indicate a well-percolated network of Ni is likely to form in the scaffold anodes, but the especially high degree of coverage in GS40 may be problematic if it eliminates TPB length as Ni deposits overlap.

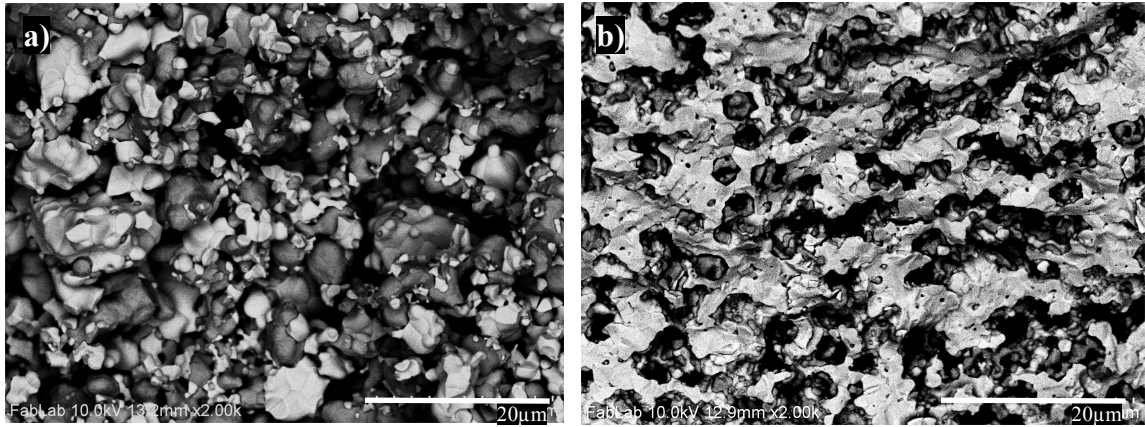


Figure 6.3: Backscattering electron images (2kx magnification) of reduced anode supports for a) cermet anode and b) GS54, a GDC (light phase) scaffold infiltrated with 11.7 vol% Ni (dark gray phase). Black areas are open porosity.

Table 6.2: Measured diameter of pores and Ni particles in each anode and calculated TPB density

	GS40	GS54	Cermet
Avg. Pore Diameter (μm)	3.3 ± 0.3	3.5 ± 0.3	4.8 ± 1.9
Avg. Ni Diameter (μm)	0.82 ± 0.23	0.90 ± 0.16	4.9 ± 2.0
Specific TPB ($\mu\text{m}/\mu\text{m}^3 \text{Ni}$)	17.8	14.8	0.5

6.3.2 Electrochemical Impedance

The measured data points were fit with an equivalent circuit (Figure 6.4a inset) that accounts for a total area-specific resistance (R_T) composed of Ohmic (R_O), electrode

(R_E) , charge transfer (R_{CT}), and mass transfer (R_{MT}) polarizations. Overall, $R_T = R_O + R_E$ and $R_E = R_{CT} + R_{MT}$. The resulting fittings are plotted as the continuous lines in Figure 6.5a and 3b. The electrochemical impedance spectroscopy data was fit using ZSimpWin 3.5 (Echem Software) to a circuit consisting of resistors and constant phase elements shown in the inset in Figure 6.4a. The overall χ^2 value for each fitting was $\sim 10^{-4}$, indicating a good fit. The components of the fits are presented in Table 6.3, and Nyquist plots with the fittings overlaid are shown in Figure 6.4. Nyquist and Bode plots of the EIS response and total fitting of each cell are overlaid in Figure 6.5.

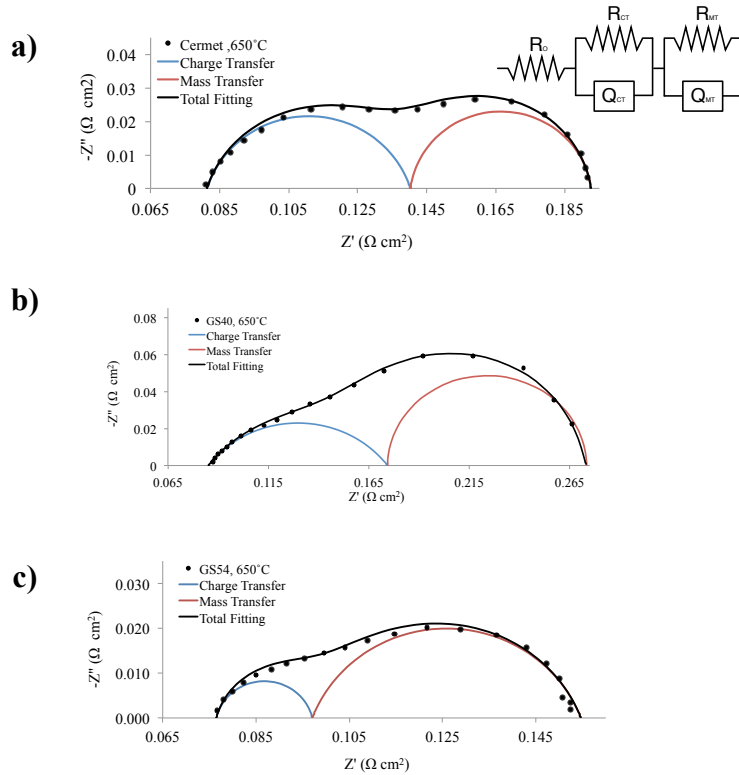


Figure 6.4: Fittings of charge transfer and mass transfer constant phase element (CPE) components to EIS data collected at 650 °C in H_2 for a) cermet, b) GS40 and c) GS54 anodes. Charge transfer fits are blue, mass transfer fits are red, total fits lines are black, and the experimental data points are marked.

Table 6.3: Model circuit component parameters determined by ZSimpWin 3.5 fittings.

Anode	R_o (Ωcm^2)	R_{CT} (Ωcm^2)	n_{CT}	$Y_{o,CT}$ (S/cm^2)	R_{MT} (Ωcm^2)	n_{MT}	$Y_{o,MT}$ (S/cm^2)	χ^2
Cermet	0.081	0.059	0.804	0.244	0.052	0.918	2.695	8.9 E-4
GS40	0.084	0.080	0.631	1.066	0.109	0.960	3.262	4.1 E-4
GS54	0.076	0.021	0.857	0.205	0.058	0.772	1.727	3.3 E-4

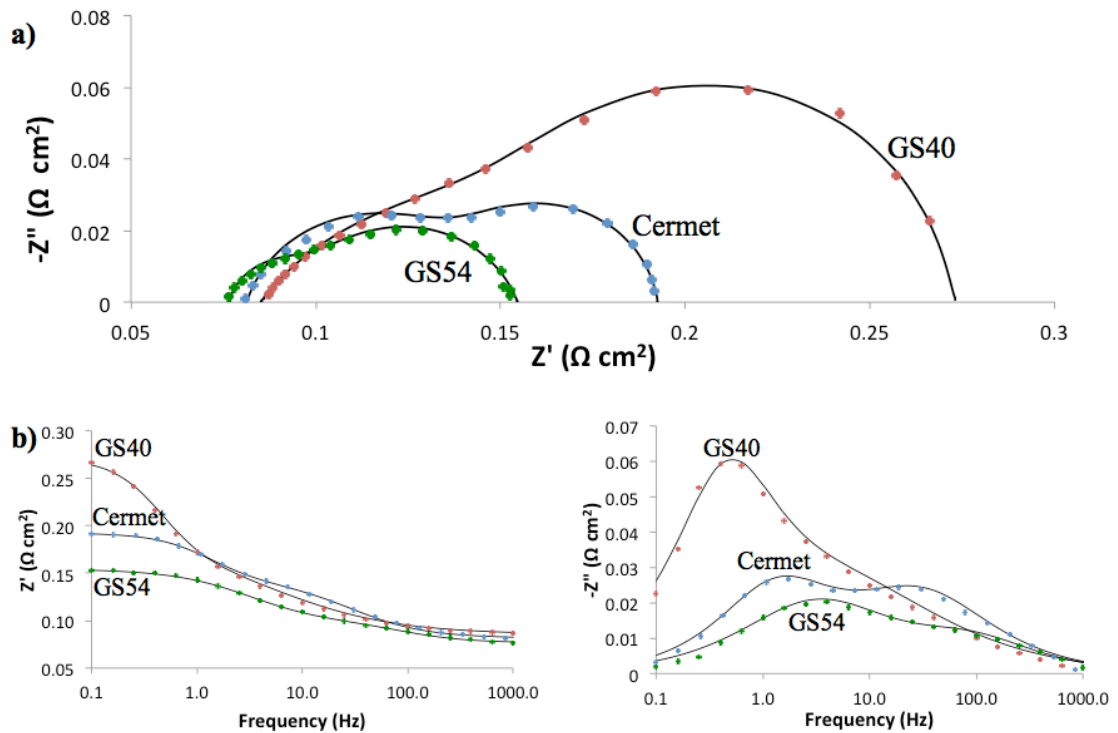


Figure 6.5. a) Nyquist and b) Bode plots of EIS response of the scaffold anode cells compared to the cermet anode cell at 650 °C in H₂. Data points are marked with circles, and the solid lines represent the results of the model circuit fitting.

The values for Ohmic and total electrode polarization are given in Table 6.4 and compared in Figure 6.6. The R_O is nearly identical for each cell, and matches the expected value for Ohmic ASR of $0.08 \Omega\text{cm}^2$ at 650°C for a $20 \mu\text{m}$ thick GDC electrolyte for the GDC powder used. This indicates that despite a low Ni loading (<12.5 vol%) of the scaffold anodes, their electrical resistance is negligible compared to that of the electrolyte and has no measurable contribution to Ohmic ASR, which confirms good percolation of the Ni network in each anode. The low frequency polarization R_{MT} , associated with transport of the gas phase, is 55% smaller in the cermet anode cell than in GS40 which had a similar volume fraction of porosity. This indicates that the tortuosity (τ) of the pores in GS40 is greater than in the cermet anode, where studies on similar anodes found $\tau \approx 2.0$ [56, 102, 104]. The R_{MT} of GS54 is similar to that of the cermet because its additional porosity helps to reduce the tortuosity of the gas diffusion path through the pores. Furthermore, the R_{CT} of the GS54 cell is drastically reduced by 67%. This is likely due to the orders of magnitude greater TPB length in GS54 that is created by the smaller Ni particles. More rigorous analysis of the microstructures that correlate to these polarizations could be performed using focused ion beam scanning electron microscopy (FIB-SEM) reconstruction to precisely quantify the tortuosity and TPB length in each anode [56, 101, 102] so anodes could be optimized to further lower their polarizations, but the observed correlations are highly promising.

Table 6.4: Real components of ASR for cells using each anode support at OCV (from EIS) and under polarization (from galvanic sweeps)

	GS40	GS54	Cermet
$R_O (\Omega \text{ cm}^2)$	0.08	0.08	0.08
$R_{CT} (\Omega \text{ cm}^2)$	0.08	0.02	0.06
$R_{MT} (\Omega \text{ cm}^2)$	0.11	0.06	0.05
$R_E (\Omega \text{ cm}^2)$	0.19	0.08	0.11
R_T at OCV ($\Omega \text{ cm}^2$)	0.27	0.16	0.19
R_T at 0.5 - 1.5 A/cm ² ($\Omega \text{ cm}^2$)	0.26	0.17	0.18
MPD (W/cm ²)	477	740	873
i_o (mA/cm ²)	315	659	483

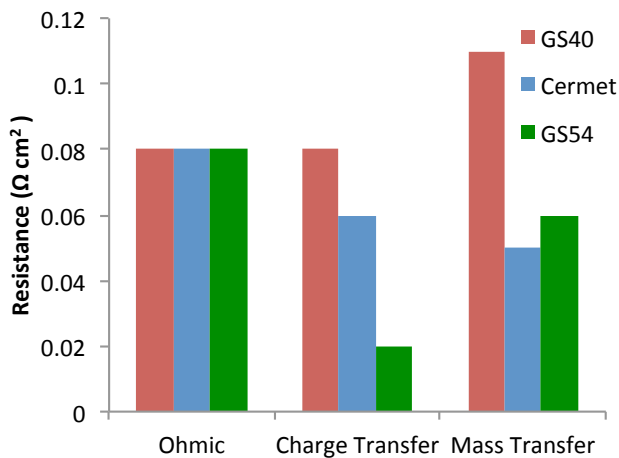


Figure 6.6. Ohmic, charge transfer, and mass transfer components of ASR for each cell, from EIS fittings at 650°C in H₂.

6.3.3 Galvanic Sweeps

The IV curves in Figure 6.7a indicate that the GS40 and GS54 anode cells exhibit slightly lower OCV than the cermet anode cell, but gas chromatography revealed no evidence of leakage in the exhaust. Furthermore, the OCV of the cells were independent of anode flow rate, indicating again that the electrolyte has no physical leaks. Reduced

ceria or GDC exhibits electronic conductivity through small polaron hopping. The observed decrease likely arises from exaggerated electronic leakage of reduced GDC due to the continuous network of reduced GDC that the electrolyte is supported on.

The power density vs. current density using 30 ccm H₂ as a fuel at 650°C is plotted in Figure 6.7b. The maximum power density (MPD) of the cermet, GS54, and GS40 anode cells are 873, 740, and 477 mW/cm², respectively. Despite containing 68% less Ni, the most porous GDC scaffold, GS54, achieved a power density only 15% less than the standard cermet anode. The slope of the IV curve was used to determine the R_{total} for each cell under polarization and added to Table 6.4. The current density range of 0.5 – 1.5 A/cm² was used to avoid activation polarization near OCV and concentration polarization at higher current density. The low R_T for GS54 compared to the other anodes indicates that it maintains high electrocatalytic activity despite low metal loading, even under polarization. Tafel plots of the electrode polarization were prepared following the method detailed by Lee et al. [55] and are presented in Figure 6.7c. The exchange current density, i_o, determined from the Tafel plots is presented in Table 6.4. The i_o is highest for the GS54 anode, again supporting a high catalytic activity due to enhanced TPB length.

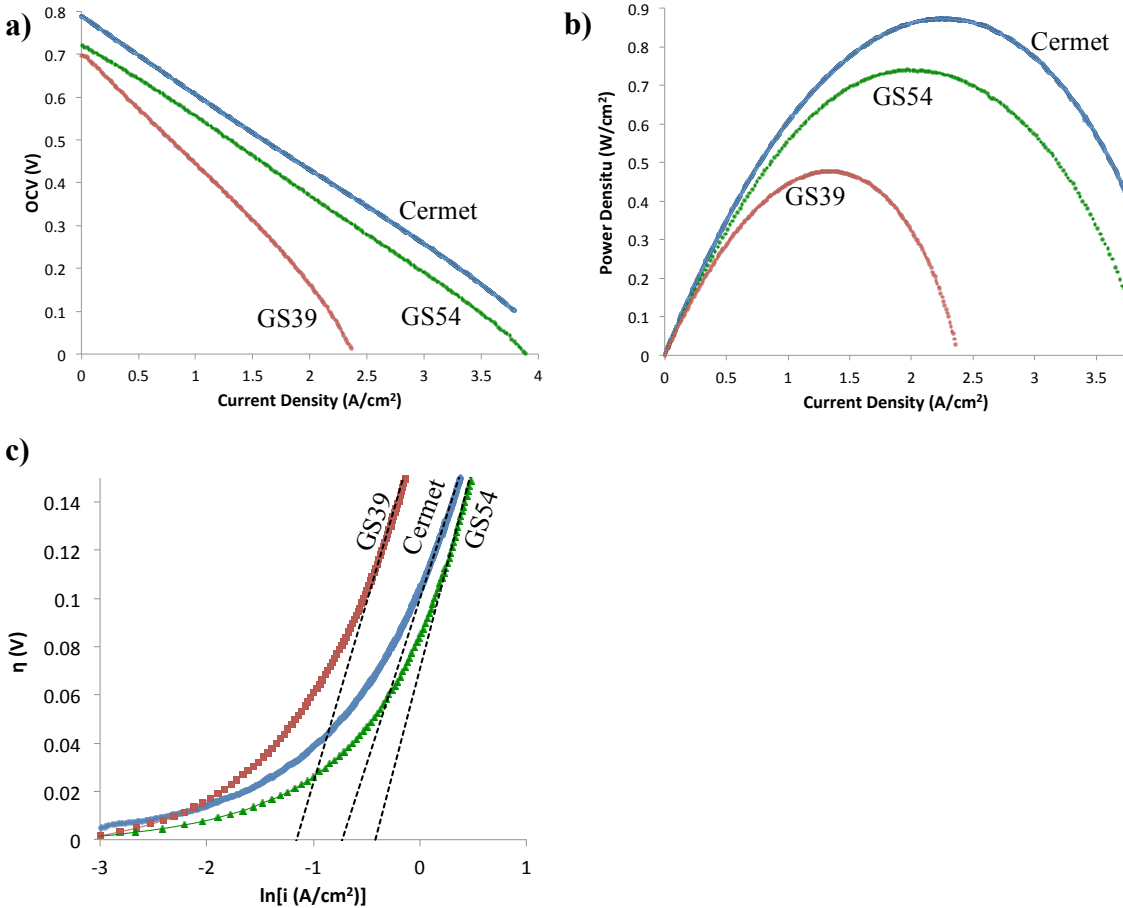


Figure 6.7. Galvanic sweep plots comparing SOFCs with the 3 anode types at 650 °C in H₂: a) Voltage vs. current density b) Power density vs. current density c) Tafel plot of the electrode overpotentials and extrapolated Tafel slope used to find exchange current density.

To ensure the attribution of the high frequency arc to charge transfer resistance is correct for each cell, the R_{CT} from the EIS fittings was cross referenced with the measured i_0 in Figure 6.8. The observed inverse relationship is expected [105, 106], and matches the slope determined at 650°C by the relationship $R_{CT} = \frac{RT}{zF i_0}$ [105, 106].

This matching linear relationship confirms that the observed high frequency arcs are related to charge transfer, and the drastic difference between each cell indicates that the

anode contribution is dominating the R_{CT} observed. Numerous reports have shown that i_o , and thus $1/R_{CT}$, is directly proportional to active TPB length, so the effectiveness of each microstructure can be correlated to changes in active TPB [56, 107].

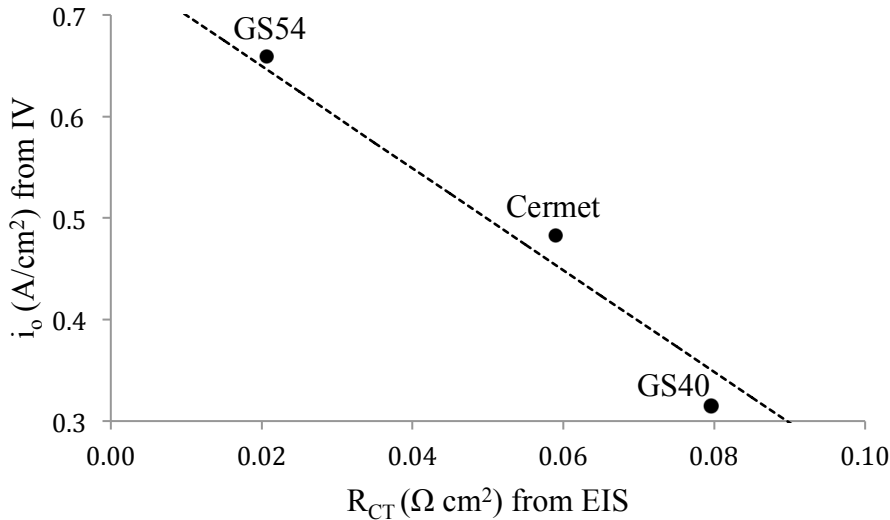


Figure 6.8: Exchange current density from galvanic sweep vs. charge transfer resistance determined by EIS fittings. Black circles are experimental data points, and the dashed line is the expected slope from the first principles relationship between R_{CT} and i_o .

6.3.4 Long term stability while utilizing CH₄

Tests in methane revealed additional differences between the GS54 and the cermet anode. Both cells were first conditioned by performing a potentiostatic test at 0.4 V at 600°C in 30 ccm H₂. The cell with the cermet anode exhibited a power density that plateaued at 422 mW/cm², and the GS54 anode cell was stable at 339 mW/cm². The fuel feed was then switched to 15 ccm CH₄ and the potentiostatic test was continued for 72 hours, with the power density vs. time of the two cells plotted in Figure 6.9a.

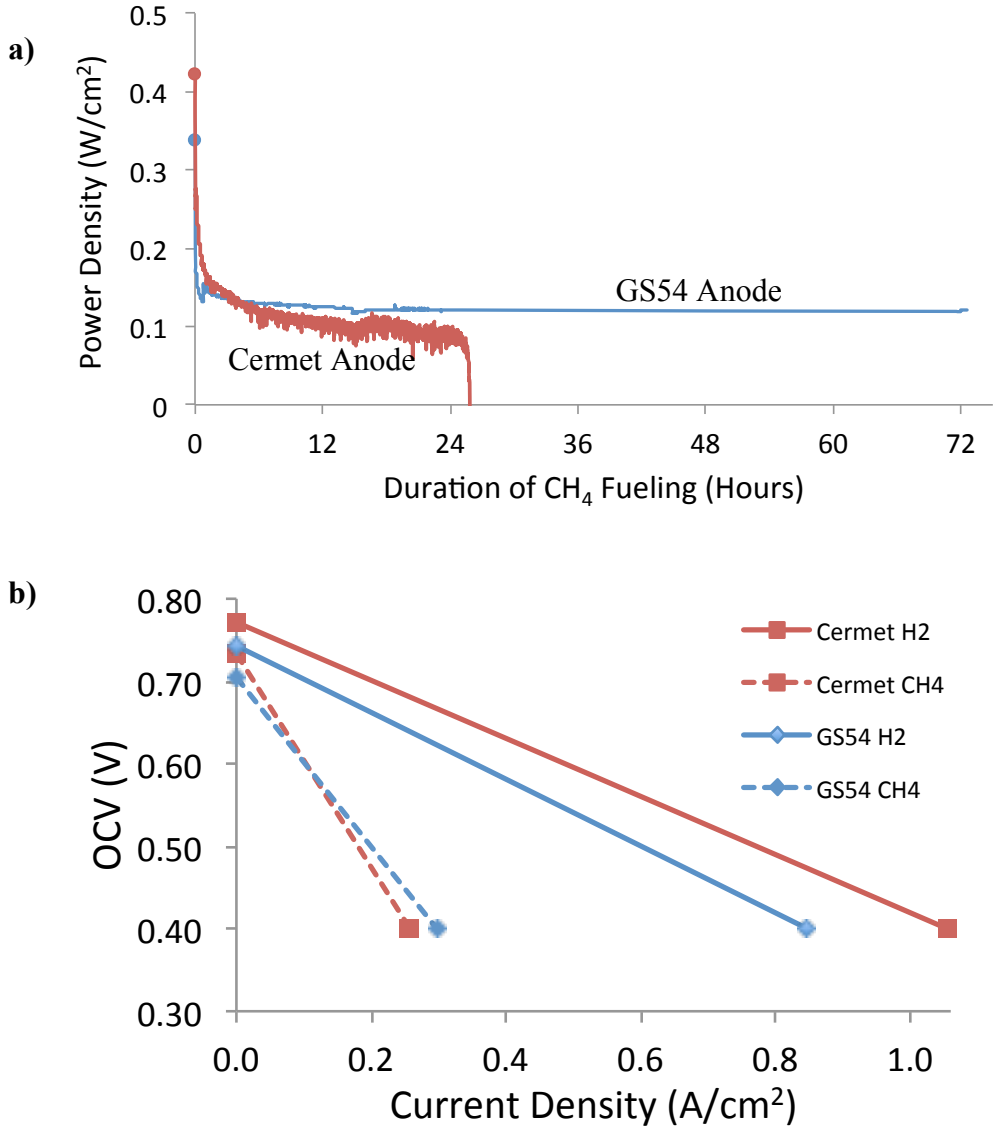


Figure 6.9. a) Long-term performance of cells after switching from 30 ccm H₂ to 15 ccm CH₄ fuel. b) Current-voltage relationships for H₂ (solid lines) and CH₄ (dashed lines) fueling.

The cell with the cermet anode showed a brief but noisy plateau in power density at 103 mW/cm², then decayed and finally dropped to nearly zero power after 24 h. The GS54 anode cell stabilized at 119 mW/cm² within 3 h, and exhibited stable power output for 72 h until the test was ended to inspect the anode *ex situ*. The lower power density of

both cells when using CH₄ is a result of the fuel's slow electrochemical oxidation kinetics compared to H₂. Interruption of the Faradaic O²⁻ flux may have initiated carbon deposition at OCV conditions [108], so no typical EIS measurements or galvanic sweeps were performed during the potentiostatic test. The additional electrode polarization in CH₄ compared to H₂ can be inferred from the steady state current observed at 0.4 V, assuming a linear IV response (Figure 6.9b). The R_T found this way is 1.51 Ω-cm² for the cermet anode and 1.08 Ω-cm² and for the GS54 anode. Subtracting the R_O associated with the electrolyte, the R_E increased 276% for GS54 and 468% for the cermet anode when compared to their value for hydrogen fueling at 600 °C. CH₄ oxidation is expected to be 2-10 times slower than H₂ oxidation [49], and these results fall within those bounds. Though the MPD of the cermet cell is higher in hydrogen, the scaffold cell, GS54, achieves higher power density in CH₄ at 600 °C via a 45% lower electrode polarization resistance. Furthermore, it is very stable.

SEM and EDS analysis reveal stark differences between the anodes after testing, as seen in Figure 6.10 and Table 6.5. The cermet anode is blocked with encapsulating carbon deposits filling the previously open porous volume observed in Figure 6.3a and covering all visible surface in the cross section, confirmed by a dominant C k_a signal at 0.277 eV that indicates 73 at% C in the anode. This significant carbon buildup is what caused cracks in the electrolyte that destroyed the cell. Both visually and using EDS spectra, it is determined that there is no carbon deposition in the GS54 anode. The 1.3 at% peak detected is a typical background signal for the C k_a line.

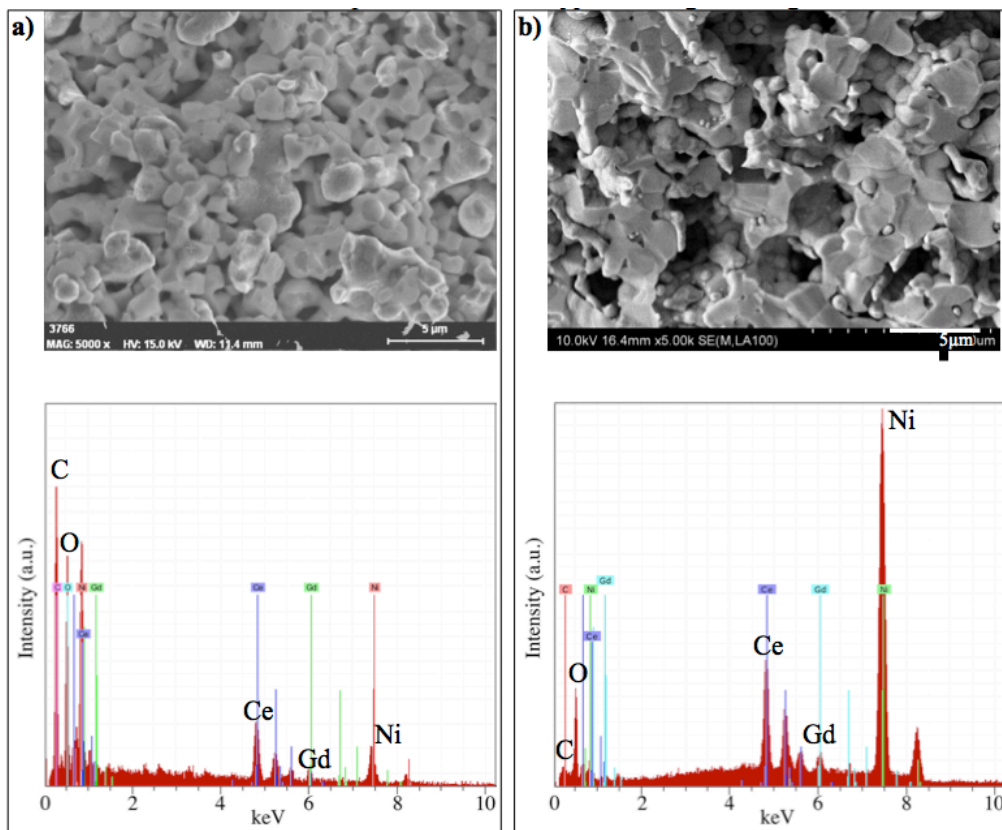


Figure 6.10. SEM micrograph and EDS spectrum of a) cermet anode with severe coking [>70 mol% C(s)] after 24 hours and b) GS54 anode with no carbon deposition after fueling with methane for 72 hours.

Table 6.5: EDS analysis of deposited carbon on anodes after long-term CH₄ fueling

Cermet	Series	Atom %	Error %
Ni	K α	18.4	1.0
Ce	L α	7.3	1.3
Gd	L α	1.3	1.7
C	K α	73.0	2.8

GS54	Series	Atom %	Error %
Ni	K α	84.4	4.5
Ce	L α	10.0	2.1
Gd	L α	4.3	1.8
C	K α	1.3	0.1

Thermodynamic calculations presented in Figure 6.11 for the conditions in both anodes predicts carbon formation, however, so there must be a kinetic mechanism keeping the GS54 anode free of carbon deposits. At 600 °C, the PO₂ required to prevent C(s) formation is equivalent to ≥ 1.86 O²⁻ ions per molecule of CH₄, and to achieve that ratio in the gas phase would require >6 times the steady state current densities used in the

potentiostatic test. Solid carbon can only deposit on solid surfaces, particularly on Ni surfaces that catalyze carbon forming reactions, so the availability of oxygen ions at the Ni surfaces is of primary importance to prevention of C(s) formation.

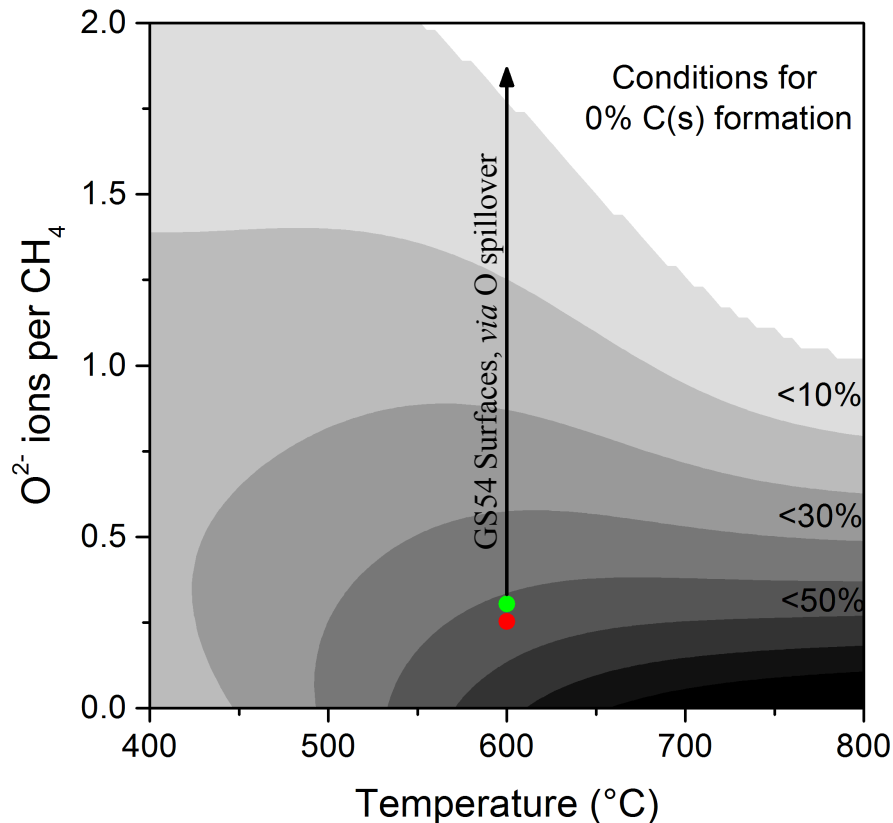


Figure 6.11. Calculated mol% of C(s) in the reaction products of CH_4 in the anode vs. temperature and available O^{2-} ions at the reaction site. The grayscale gradient is in 10 mol% increments. Red and green points show the calculated $\text{O}^{2-}:\text{CH}_4$ ratio in the cermet and GS54 anode atmosphere, respectively.

Oxygen spillover from ceria or GDC has been demonstrated to reoxidize solid carbon species on Ni films even when the PO_2 of the gas phase is low because the active O^{2-} ions are constrained to the Ni surface. The submicron particle size of the Ni deposited in the GS54 cell gives oxygen ions a short path length on the Ni surface when saturating it via oxygen spillover. The much larger Ni particles in the cermet have longer

diffusion path lengths, and plausibly cannot deliver oxygen ions rapidly enough to sites where CH_4 is reforming in order to prevent carbon deposition. Furthermore, the oxygen ions that saturate the Ni particles must originate from the electrolyte, and there is no continuous path of O^{2-} conducting material in many regions of the randomly mixed cermet anode. The GS54 anode has percolation of GDC, the O^{2-} conducting phase, to every region of the anode because it is the continuous supporting phase that the Ni is deposited on. Figure 6.12 gives a schematic of the two effects that contribute to the prevention of carbon deposition in the GDC scaffold cell.

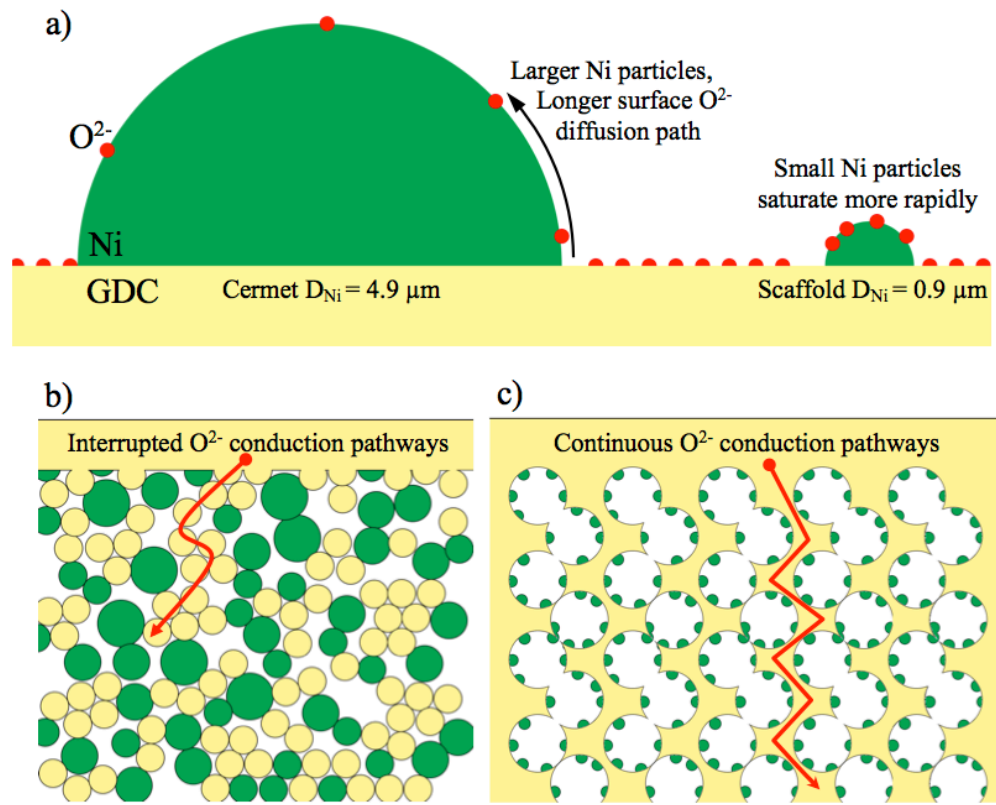


Figure 6.12. Schematic of the microstructural factors contributing to enhanced oxygen spillover in the GDC scaffold anode: a) smaller Ni particles have shorter surface diffusion paths for oxygen ions b) there is no continuity of ionic conductor from the electrolyte to many Ni surfaces of the cermet anode c) every Ni particle in the scaffold anodes is constrained on a continuous network of ionic conductor, providing a pathway for oxygen ions to be replenished from the electrolyte.

6.4 Conclusions:

SOFCs with standardized electrolyte and cathode thicknesses were fabricated with three types of anode: one made of a 50:50 vol% Ni-GDC cermet, and two made from porous GDC scaffolds impregnated with <12.5 vol% Ni as a catalyst and electronic conductor. The microstructure, electrochemical performance, and resistance to carbon deposition when using methane as a fuel were compared for each type of anode. Though the GDC scaffolds contain 68% less Ni than the cermet anode, they exhibited a total ASR under polarization that is 20% lower, indicating that they provide better oxidation catalysis. They also achieved comparable MPD, only 15% lower than that of the cermet anodes. Adequate porosity is required in the GDC scaffold, however, or the ASR increases significantly. The submicron particle size of the Ni in the GDC scaffold cells creates an order of magnitude more TPB length per volume of Ni than the larger particles in the cermet anode do, so less Ni is needed for good catalysis. When coupled with a continuous scaffold of GDC, the smaller Ni particles have the added benefit of preventing carbon deposition when operating on methane fuel for 72 hours at 600 °C by enhancing oxygen spillover from the GDC to the Ni surfaces. The conventional cermet anode was destroyed by solid carbon buildup under identical conditions, so the scaffold anodes have promising potential to be used in low temperature SOFCs operating on hydrocarbon fuels.

Chapter 7: Development of Mixed Conducting Barium Cerate Ceramics for Metal-Free Anodes

The contents of this chapter have been published as C. M. Gore, et al., *Effect of composition and microstructure on electrical properties and CO₂ stability of donor-doped, proton conducting BaCe_{1-(x+y)}Zr_xNb_yO₃*, J. Mater. Chem. A, 2, 2363 (2014).

- Reproduced by permission of The Royal Society of Chemistry. Some content has been added or modified.

7.1 Introduction

Well-known acceptor-doped perovskite-type cerates, e.g., AB_{1-x}M_xO_{3-δ} (0 < x < 0.3) (A = Sr, Ba; B = Zr, Ce; M = Y, La, Sm, Gd), are potential membranes or electrodes for numerous solid-state ionic devices including solid oxide fuel cells (SOFCs), H₂O electrolyzers, hydrogen pumps, and hydrogenators for renewable fuel synthesis [6, 7, 109-115]. These applications rely on the high proton conductivity of doped cerates in the presence of hydrogen-containing atmospheres at elevated temperatures. High temperature proton conductors (HT-PCs) are an alternative to standard polymer Nafion in proton-exchange membrane fuel cells (PEMFCs) and are anticipated to overcome several challenges, including CO poisoning of Pt catalysts from impure fuels and water management for high proton conductivity [1, 5, 116, 117]. Thus, attempts have been made to improve the proton conductivity of acceptor-doped perovskites at lower temperature by investigating the effect of doping and sintering temperature on conductivity.

Several researchers have studied chemical stability and proton conduction of acceptor-doped BaCeO₃ under CO₂ and H₂O as a function of temperature to evaluate their suitability for direct hydrocarbon fueled SOFCs [1, 5, 9, 10, 117-128]. Thermodynamic calculations and experimental studies show that BaCeO₃ forms BaCO₃ at < 1040°C and Ba(OH)₂ at < 403 °C [9, 119]. Zr-substitution for Ce improves the chemical stability under CO₂ and H₂O, but decreases proton conductivity [5, 10, 128]. Also, BaZrO₃ exhibits a large grain-boundary impedance and the preparation of a gas dense membrane is difficult due to the poor sinterability and highly refractory nature of zirconia based perovskites [1, 6, 7, 116].

Recently, Bhella et al. reported proton conduction in Zr and Nb–codoped BaCe_{0.9} _{$_x$} Zr _{x} Nb_{0.1}O_{3±δ} ($x = 0.1; 0.2$) which was found to be chemically stable in CO₂ at elevated temperatures at which highly conductive Y-doped BaCeO₃ was found to be chemically unstable [123]. Of the two members studied, a perovskite with nominal chemical composition of BaCe_{0.8}Zr_{0.1}Nb_{0.1}O_{3±δ} showed the bulk electrical conductivity of $\sim 10^{-3}$ Scm⁻¹ in wet H₂ at 500 °C with an activation energy of 0.69-0.73 eV which is comparable to that of Y-doped BaCeO₃. That preliminary work did not investigate the chemical stoichiometry of Zr and Nb in BaCeO₃ as a function of temperature or evolution of microstructure due to different sintering conditions, factors that commonly control the proton conductivity of doped perovskites. Furthermore, the necessity of co-sintering of electrolyte and electrodes for HT-PC device preparation motivates an understanding of how to control porosity and conductivity in the electrodes while maintaining a dense electrolyte. Here, we have performed a systematic investigation to understand the role of sintering temperature and composition on microstructure, porosity and electrical transport

properties of $\text{BaCe}_{1-x-y}\text{Zr}_x\text{Nb}_y\text{O}_3$ ($x = 0.05, 0.1, 0.15, 0.2$; $y = 0.05$, and 0.1). In addition, in-situ monitoring of carbonate formation was performed employing thermo-gravimetric analysis from RT to 1100°C in a 30% CO_2 atmosphere to investigate chemical stability.

7.2 *Experimental*

7.2.1 Preparation, Phase, and Microstructure Studies of $\text{BaCe}_{1-(x+y)}\text{Zr}_x\text{Nb}_y\text{O}_3$ ($x = 0.05, 0.1, 0.15, 0.2$; $y = 0.05$, and 0.1).

The perovskite oxides with nominal chemical formula $\text{BaCe}_{0.9}\text{Zr}_{0.05}\text{Nb}_{0.05}\text{O}_3$ (**I**), $\text{BaCe}_{0.8}\text{Zr}_{0.1}\text{Nb}_{0.1}\text{O}_3$ (**II**), $\text{BaCe}_{0.75}\text{Zr}_{0.15}\text{Nb}_{0.1}\text{O}_3$ (**III**) and $\text{BaCe}_{0.7}\text{Zr}_{0.2}\text{Nb}_{0.1}\text{O}_3$ (**IV**) were prepared in air by a conventional solid state reaction route using desired stoichiometric amounts of high purity (99.9%) precursors: $\text{Ba}(\text{NO}_3)_2$ (Alfa Aesar), CeO_2 (Alfa Aesar), Nb_2O_5 (Alfa Aesar), and ZrO_2 (Inframal). The reactant powders were milled for 24 h using a ball mill (US Stoneware) with 1 cm diameter zirconia milling media (Inframal). The powders were then dried in air and sintered in air at 900°C for 12 h in an alumina crucible. The resulting mixture was ball milled and pressed into pellets at 115 MPa in an isostatic press (Carver). Sets of the pressed pellets were sintered at 1450, 1500, 1550 and 1600°C for 6 h in air to understand the role of sintering temperature on phase formation and microstructure. Sample pellets were then ground into a powder for characterization by X-ray diffraction (XRD) using a Bruker D8 powder X-ray diffractometer ($\text{CuK}\alpha$, 40 kV; 40 mA). Scanning electron microscopy (SEM) of the investigated perovskite compounds was performed using a Hitachi SU-70 with field emission gun equipped with a Bruker XFlash silicon drift detector for EDS measurements. The samples were carbon

coated prior to analysis to provide electronic conductivity to eliminate any charging effect.

7.2.2 AC Impedance Characterizations.

2-point AC electrical conductivity measurements were performed using a Solartron 1260 frequency response analyzer with 100 mV perturbation from 1 MHz to 0.1 Hz in air. To ensure accurate electrode area, the sample surfaces were polished before applying the electrodes. Platinum paste (Heraeus) was applied to both sides of the sintered pellets and cured at 700 °C for 1 h in air to remove the organic binders. The conductivity of each sample was measured at the temperature range of 400-700 °C in air. Each sample was thermally equilibrated at constant temperature for 1 hour prior to each measurement.

7.2.3 Thermogravimetric Measurements.

Each sample was analyzed for CO₂ stability by thermogravimetric analysis (TGA). The pellets sintered at 1450 °C were ground into powder, loaded into a microbalance (Cahn TG 2141), and heated to 1100 °C at 2 °C/min in a 30% CO₂, balance N₂ atmosphere. The mass change was monitored to determine the extent of BaCO₃ formation in the samples.

XPS Studies. XPS spectra were acquired using a Kratos Axis 165 x-ray photoelectron spectrometer operating in the hybrid mode using Al K α radiation (1486.6 eV). The instrument was run in hybrid mode with a pass energy of 160 eV for survey spectra and a

pass energy of 20 eV for high-resolution spectra. Peak energies were calibrated to the adventitious carbon C 1s peak centered at 284.6 eV. Peak fittings were performed using CasaXPS software. It is vital to note that the Ce 3d spectra must be corrected for an overlapping Ba auger peak when examining BaCeO₃ based materials with an Al k_a x-ray source. Further peak calibration and characterization details are given in Supplementary Information

7.3 Results

7.3.1 PXRD Analysis.

Figure 7.1 shows powder XRD patterns of as-prepared BaCe_{0.9}Zr_{0.05}Nb_{0.05}O₃ (**I**), BaCe_{0.8}Zr_{0.1}Nb_{0.1}O₃ (**II**), BaCe_{0.75}Zr_{0.15}Nb_{0.1}O₃ (**III**), and BaCe_{0.7}Zr_{0.2}Nb_{0.1}O₃ (**IV**) at 1450-1600 °C in air for 4 h. The formation of a single-phase orthorhombic perovskite-type phase was observed for all the investigated BaCe_{1-(x+y)}Zr_xNb_yO₃ materials. Selected area PXRD of (040), (224), and (400) reflections between 59 and 61° 2θ is shown in Figure 2a for the samples prepared at 1600 °C, with undoped BaCeO₃ measured as a reference. The regular shifts of these reflections indicate that doping the B-site regularly occupied by tetravalent Ce or Zr cation with the smaller ionic radii pentavalent Nb in BaCe_{1-(x+y)}Zr_xNb_yO₃ shifts the Bragg peak to smaller 2θ values, confirming solid solution formation by Vegard's Law.

$$a_{BaMO_3(M = Ce, Zr, Nb)} \propto (1-x-y) \cdot r_{Ce^{4+}} + x \cdot r_{Zr^{4+}} + y \cdot r_{Nb^{5+}} \quad (7.1)$$

A similar result was observed for sintering at 1450, 1500, 1550 °C. All of the observed diffraction peaks could be indexed based on orthorhombic perovskite-type structure and

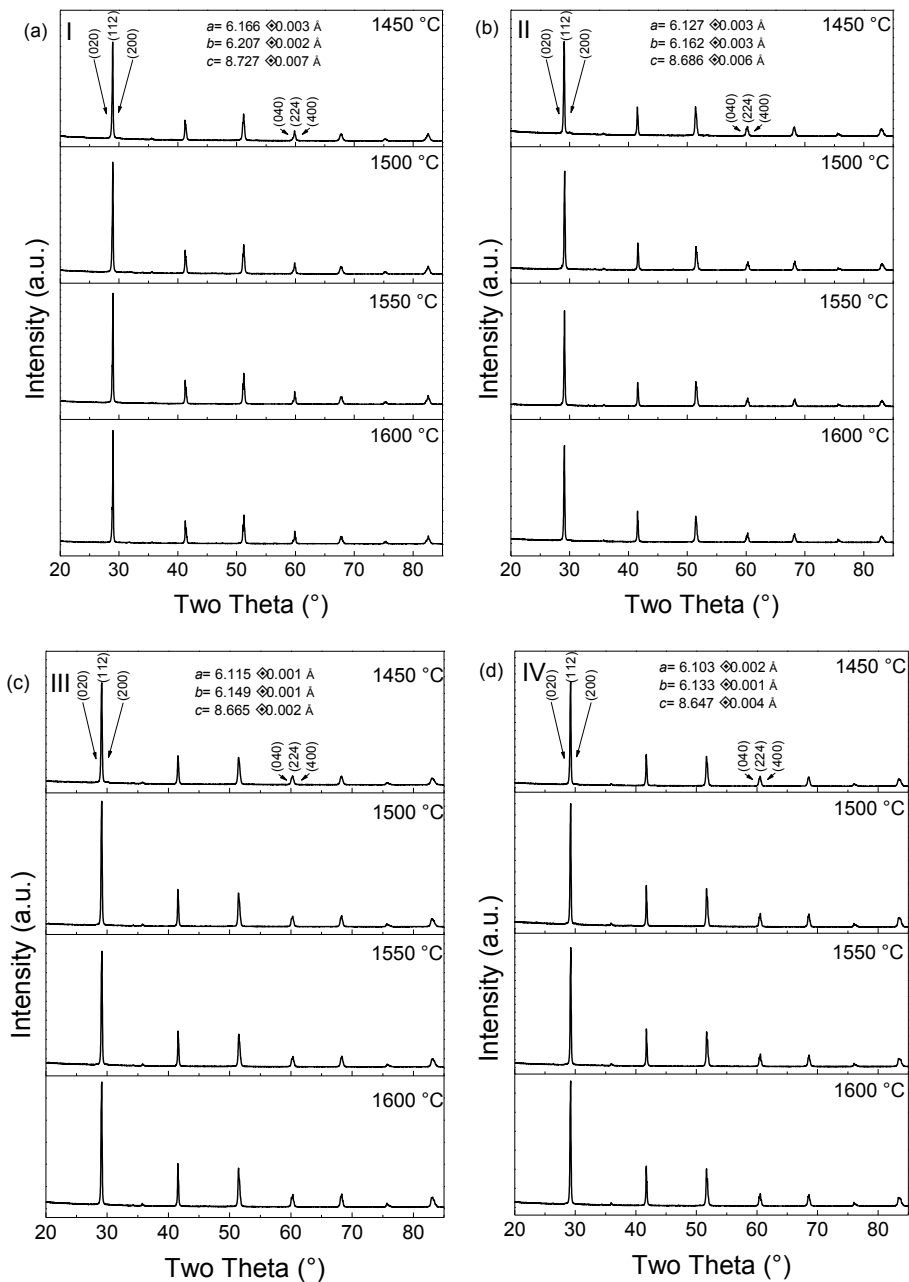


Figure 7.1 Powder XRD diffractograms and lattice parameters of as-prepared (a) BaCe_{0.9}Zr_{0.05}Nb_{0.05}O₃ (I), (b) BaCe_{0.8}Zr_{0.1}Nb_{0.1}O₃ (II), (c) BaCe_{0.75}Zr_{0.15}Nb_{0.1}O₃ (III) and (d) BaCe_{0.7}Zr_{0.2}Nb_{0.1}O₃ (IV) sintered at 1450-1600 °C in air. For clarity, only the reflections used to calculate the lattice parameters are indexed. The formation of a single-phase orthorhombic perovskite-type phase was observed for all the investigated compounds.

the resulting cell constants and lattice volumes are summarized in Figure 7.1 and 7.2b, respectively. The measured parameters are consistent with neutron diffraction data of orthorhombic BaCeO₃ by Jacobson et al. [129].

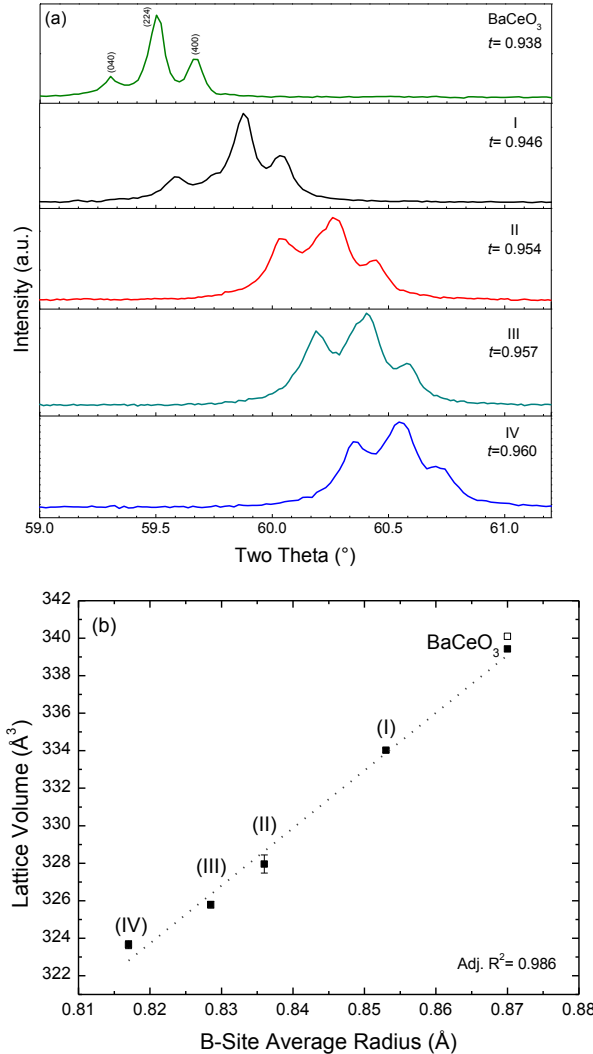


Figure 7.2 (a) Selected area powder XRD diffractograms showing the (040), (224), and (040) reflections and calculated tolerance factor of BaCe_{0.9}Zr_{0.05}Nb_{0.05}O₃ (**I**), BaCe_{0.8}Zr_{0.1}Nb_{0.1}O₃ (**II**), BaCe_{0.75}Zr_{0.15}Nb_{0.1}O₃ (**III**), BaCe_{0.7}Zr_{0.2}Nb_{0.1}O₃ (**IV**), and BaCeO₃ sintered at 1600 °C. (b) Variation of lattice volume as a function of B-site average ionic radius. A reference point for BaCeO₃ lattice volume by neutron diffraction (□) is given based on measurements by Jacobson et al²⁸. The linear shift in the diffraction peaks and decrease in cell volume versus B-site radius support Zr and Nb -cosubstitution for Ce in the perovskite-type structure, confirming solid solution. Note that most error bars are smaller than symbols.

7.3.2 AC Impedance Analysis:

The evolution of AC impedance in air for $\text{BaCe}_{1-(x+y)}\text{Zr}_x\text{Nb}_y\text{O}_3$ as a function of sintering temperature is shown in Figures 7.3-7.4 at 400 and 700 °C, respectively. The AC impedance data reveal the following facts:

- (i) Over the investigated temperature range (400-700°C), a clear low-frequency intercept to the real (Z') axis was observed for the samples, suggesting that the Pt electrode and sample interface is reversible (non-blocking for electrons and oxide ions). Hence, the low-frequency intercept could be considered as sum of both electronic and oxygen reduction resistance to total impedance in air [130].
- (ii) $\text{BaCe}_{1-(x+y)}\text{Zr}_x\text{Nb}_y\text{O}_3$ sintered at lower temperature shows a large low-frequency intercept to the real (Z') axis compared to the corresponding composition sintered at higher temperature (Figures 7.3a and 7.3b). Also, over the investigated range, only part of the high-frequency arc was observed since the frequency response analyzer shows artifacts as it switches internal circuits at 10^6 Hz, introducing discontinuities in the data above that frequency. The low-frequency impedance can be described using an equivalent circuit consisting of parallel resistance (R) and constant phase elements (CPE). The impedance of the CPE can be expressed as $Z_{CPE} = \frac{1}{Q(j\omega)^n}$ where Q is the pseudocapacitance of the CPE, ω is angular frequency and is equal to $2\pi f$ (f is the linear-frequency), j is equal to $\sqrt{-1}$, and n is the empirical constant, which can take a value between 0

and 1. For $n = 1$, the impedance of the CPE is a pure capacitance. The solid line passing through the data points represents the fitted model circuit data in Figures 7.3 and 7.4. We have shown the fitting for the typical members of the family investigated. The true capacitance can be estimated from CPE using the relationship [130-133]: $C = R^{\left(\frac{1-n}{n}\right)} Q^{\left(\frac{1}{n}\right)}$. Shown in Figure 7.5 is the capacitance of the low-frequency arc at 400-700 °C for $\text{BaCe}_{1-(x+y)}\text{Zr}_x\text{Nb}_y\text{O}_3$. The magnitude of the capacitance was found to be on the order of nanofarads, suggesting that the low-frequency arc could be attributed to grain-boundary impedance. The capacitance was found to be rather independent of temperature between 400-700 °C.

(iii) For all the investigated compositions, the low-frequency arc capacitance increases with increasing final sintering temperature (1450-1600 °C). In some cases, for e.g., $\text{BaCe}_{0.9}\text{Zr}_{0.05}\text{Nb}_{0.05}\text{O}_3$, it was found to be about an order of magnitude increase in capacitance at 1600 °C compared to that of 1450 °C. Generally, C_{gb} will increase when the surface area of the capacitive interfaces increase. Though the grain sizes increase with higher sintering temperatures, the sample density simultaneously increases. More capacitive area is gained by densification than is lost by grain growth, thus the capacitance increases, which agrees with ceramic sintering phenomena described by Irvine et al. [35]. There is a sharp increase in the capacitance of lower doped compositions at high sintering temperature, as can be seen in Figure 7.5a and 7.5b, and composition

$\text{BaCe}_{0.8}\text{Zr}_{0.1}\text{Nb}_{0.1}\text{O}_3$ is up to an order of magnitude more capacitive than the other compositions which correlates to its much larger grain sizes.

(iv) The capacitance for the high-frequency arc was determined to be on the order of picofarads, confirming a bulk conductivity contribution to the electrical properties. For any given composition in $\text{BaCe}_{1-(x+y)}\text{Zr}_x\text{Nb}_y\text{O}_3$, the total impedance, comprising of bulk and grain-boundary impedance, decreases with increasing final sintering temperature.

In this work, we have obtained the total conductivity using the low-frequency intercept to the real axis, bulk conductivity from the high-frequency intercept, and the difference between low and high frequency intercept gives grain-boundary impedance. This assignment was made based on the capacitance values [35]. Low frequency electrode effects were ruled out based on capacitance as well as $p\text{O}_2$ response of the samples revealing minimal contribution under the investigated conditions.

Figure 7.6 shows the Arrhenius plots for electrical conductivity of $\text{BaCe}_{1-(x+y)}\text{Zr}_x\text{Nb}_y\text{O}_3$. Table 1 lists the isothermal bulk, grain-boundary conductivity and their activation energies along with density of investigated compounds prepared at 1450-1600 °C. Note that since porosity is desired in electrodes, the conductivity values determined by EIS are not adjusted for the determined porosity of each sample. The 5 % Zr-doped $\text{BaCe}_{0.9}\text{Zr}_{0.05}\text{Nb}_{0.05}\text{O}_3$ exhibits the highest bulk conductivity of all the investigated temperatures, while the highest Zr-doped $\text{BaCe}_{0.7}\text{Zr}_{0.2}\text{Nb}_{0.1}\text{O}_3$ (IV) shows the lowest bulk, grain-boundary and total conductivity at 1450 °C. This result is consistent with literature trends where substitution of Zr for Ce in BaCeO_3 decreases the electrical conductivity for

materials with identical processing conditions [5, 6, 10]. The activation energy for electrical conduction in the bulk decreases with increasing B-site average ionic radius (Figure 7.7) with a very good fit ($\text{Adj. } R^2 > 0.999$) because the corresponding constriction of lattice volume impedes the motion of charge carriers in the lattice. An interesting effect of co-doping Nb with Zr is that the grain boundary resistance of the $\text{BaCe}_{0.8}\text{Zr}_{0.1}\text{Nb}_{0.1}\text{O}_3$ is smaller than the sample with lower Zr doping, $\text{BaCe}_{0.9}\text{Zr}_{0.05}\text{Nb}_{0.05}\text{O}_3$, leading to greater total conductivity when fired at 1500 °C (Figure 7.3a & 7.4a). This is likely due to an enhancement in grain size caused by the larger Nb doping, even though Nb doping alone has been shown to decrease total conductivity [123]. This is corroborated by a greater improvement in total conductivity in $\text{BaCe}_{0.9}\text{Zr}_{0.05}\text{Nb}_{0.05}\text{O}_3$ than in $\text{BaCe}_{0.8}\text{Zr}_{0.1}\text{Nb}_{0.1}\text{O}_3$ in the 1600 °C fired samples.

7.3.3 SEM Analyses.

Evolution of microstructure due to different sintering temperature is shown in Figure 7.8. As anticipated, crystallite size increases with increasing temperature. The samples prepared at 1600 °C exhibited very dense structure and the porosity determined using Archimedes method was found to be negligible, while samples processed at 1450 °C show up to 40% porosity (Table 7.1). Substitution of refractory zirconia for Ce in $\text{BaCe}_{1-(x+y)}\text{Zr}_x\text{Nb}_y\text{O}_3$ yields a less dense structure, while Nb-doping improves the density of the microstructure at all temperatures studied.

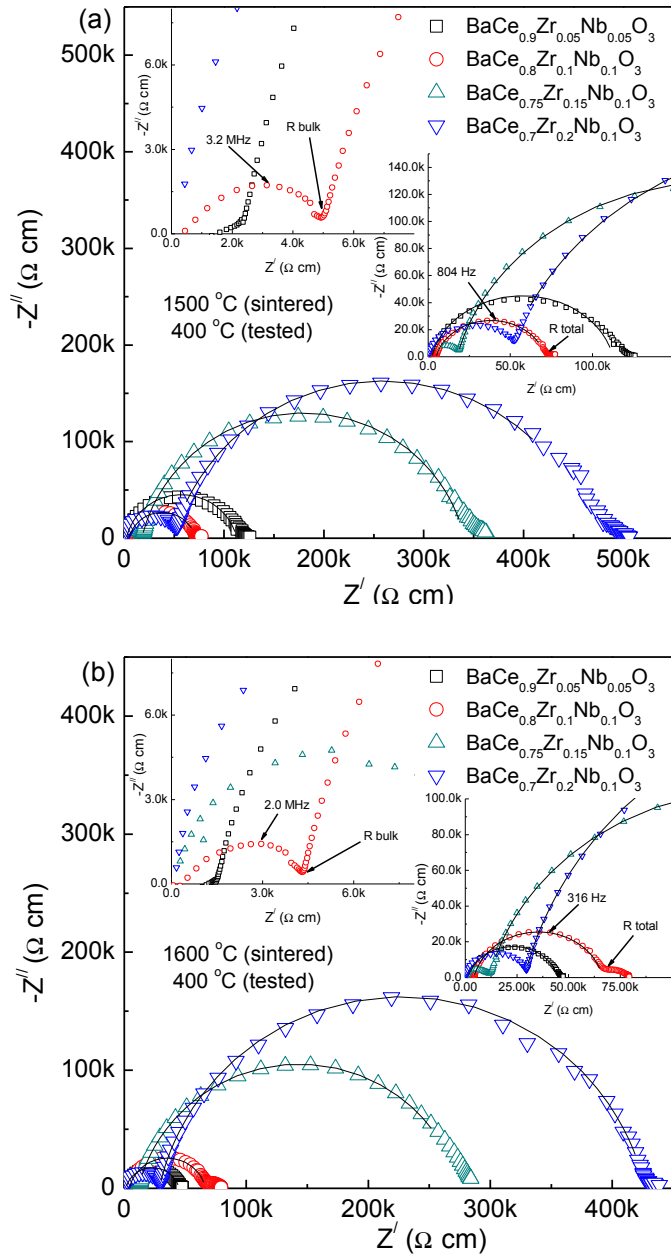


Figure 7.3 Typical AC impedance plots obtained at 400 °C in air, using Pt electrodes, for $\text{BaCe}_{0.9}\text{Zr}_{0.05}\text{Nb}_{0.05}\text{O}_3$, $\text{BaCe}_{0.8}\text{Zr}_{0.1}\text{Nb}_{0.1}\text{O}_3$, $\text{BaCe}_{0.75}\text{Zr}_{0.15}\text{Nb}_{0.1}\text{O}_3$, and $\text{BaCe}_{0.7}\text{Zr}_{0.2}\text{Nb}_{0.1}\text{O}_3$ (a) sintered 1500 °C and (b) sintered 1600 °C. An example of intercepts used for bulk and total resistance measurements and the characteristic peak frequency are indicated for $\text{BaCe}_{0.8}\text{Zr}_{0.1}\text{Nb}_{0.1}\text{O}_3$ (red circles) in each plot.

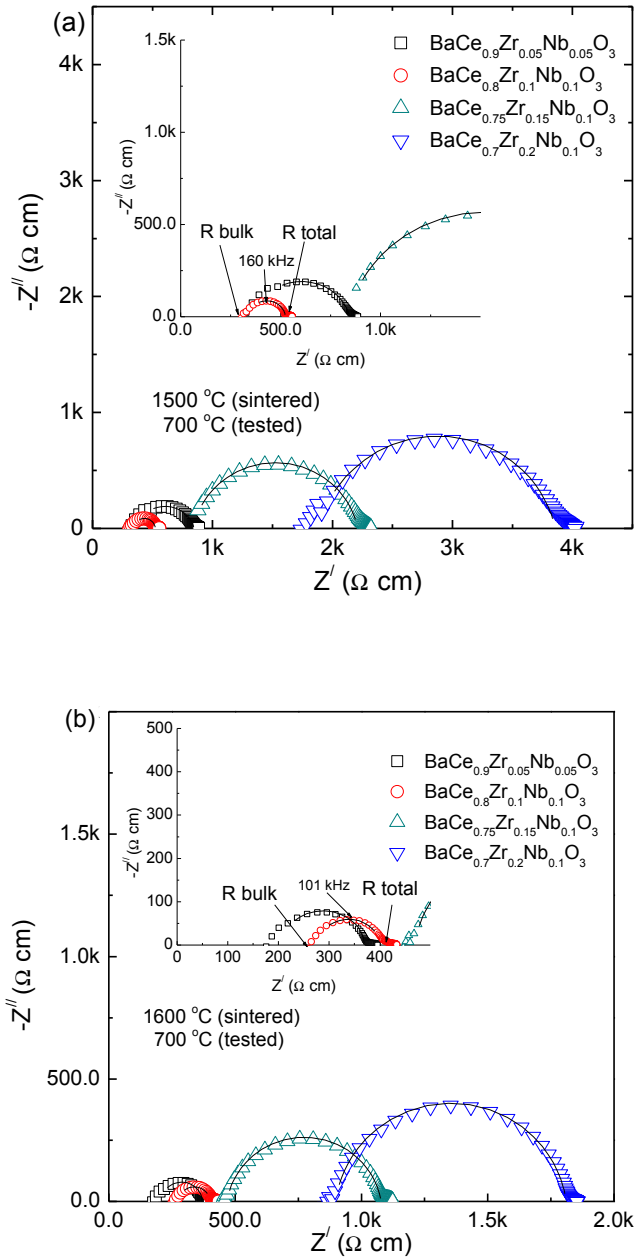


Figure 7.4 Typical AC impedance plots obtained at 700°C in air, using Pt electrodes, for $\text{BaCe}_{0.9}\text{Zr}_{0.05}\text{Nb}_{0.05}\text{O}_3$, $\text{BaCe}_{0.8}\text{Zr}_{0.1}\text{Nb}_{0.1}\text{O}_3$, $\text{BaCe}_{0.75}\text{Zr}_{0.15}\text{Nb}_{0.1}\text{O}_3$, and $\text{BaCe}_{0.7}\text{Zr}_{0.2}\text{Nb}_{0.1}\text{O}_3$ (a) sintered 1500°C and (b) sintered 1600°C . An example of intercepts used for bulk and total resistance measurements and the characteristic peak frequency are indicated for $\text{BaCe}_{0.8}\text{Zr}_{0.1}\text{Nb}_{0.1}\text{O}_3$ (red circles) in each plot.

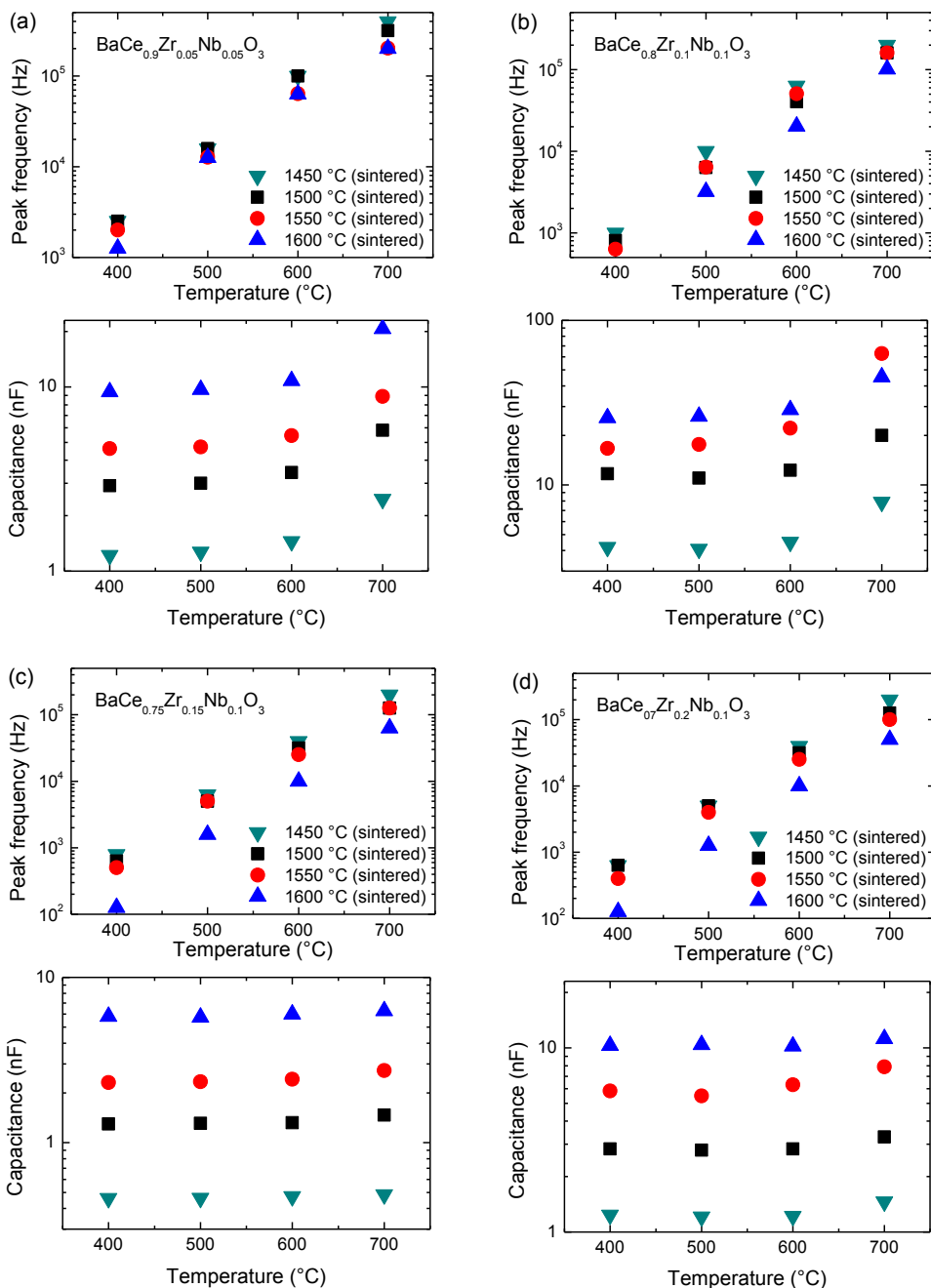
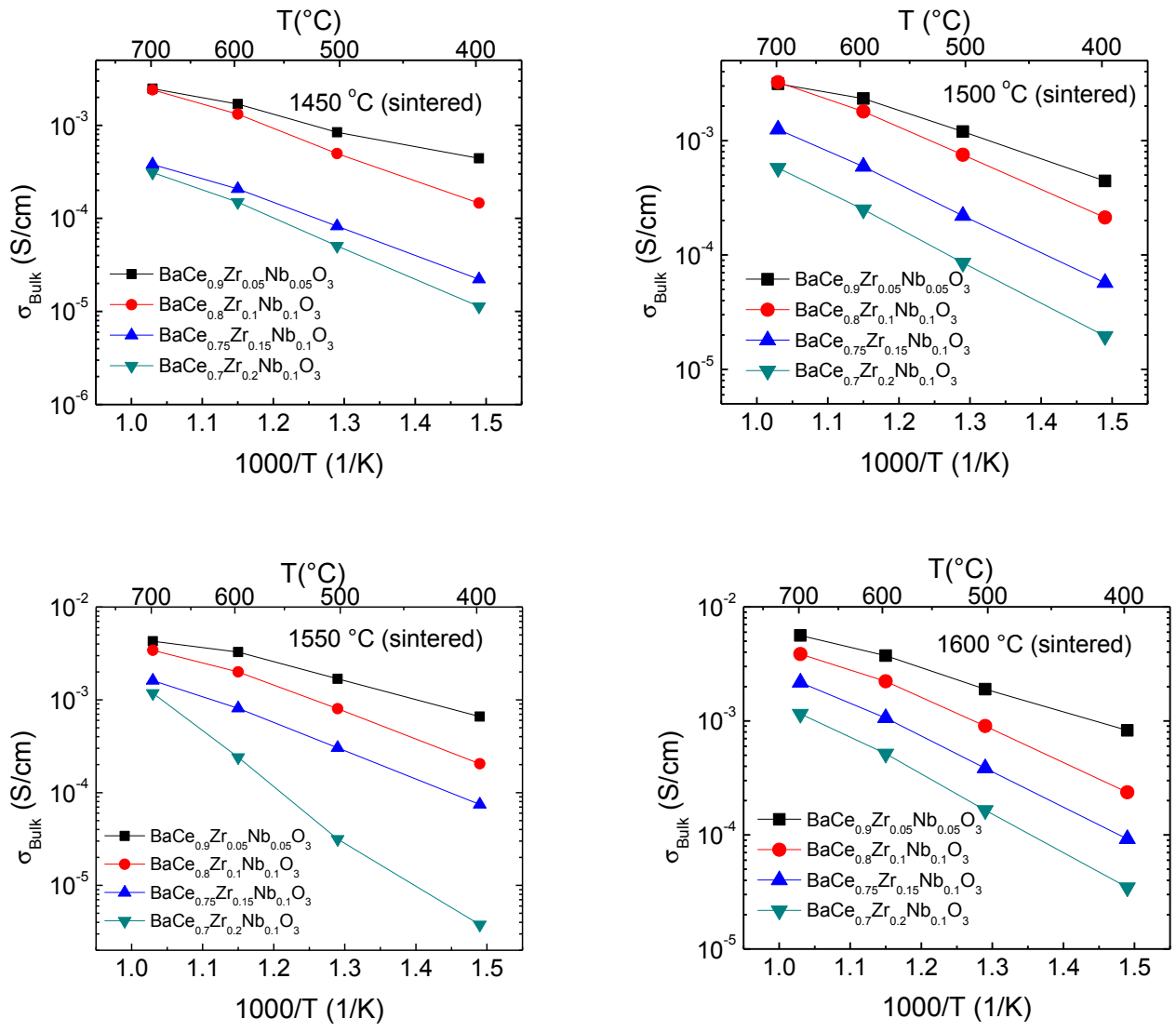
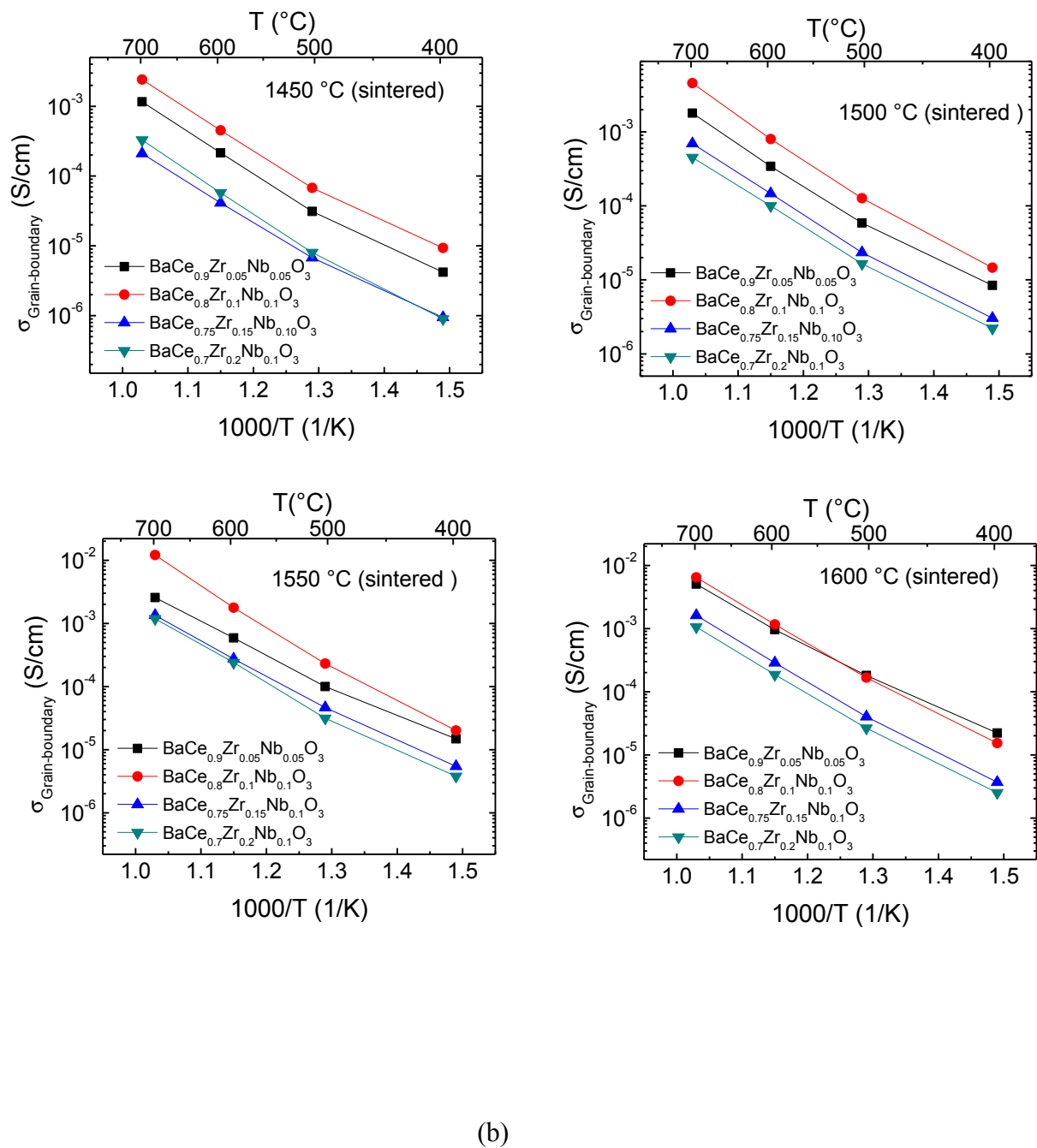


Figure 7.5 Grain-boundary real capacitance vs. temperature increases with sintering temperature, following an improvement in densification for all compositions. Nanofarad-range capacitances suggest grain boundary conduction processes.



(a)



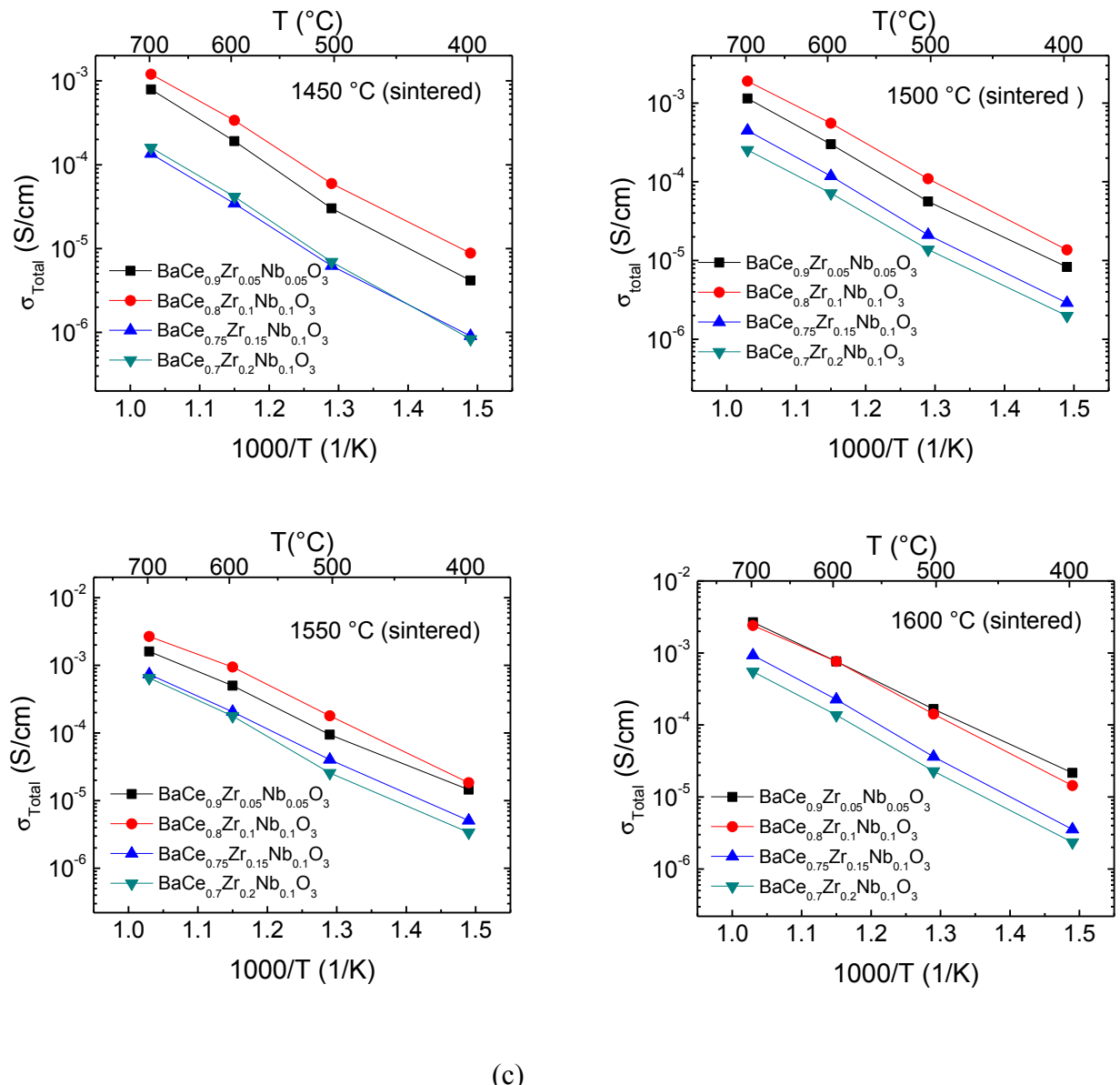


Figure 7.6 Arrhenius plots for (a) bulk, (b) grain-boundary, and (c) total conductivity of $\text{BaCe}_{0.9}\text{Zr}_{0.05}\text{Nb}_{0.05}\text{O}_3$, $\text{BaCe}_{0.8}\text{Zr}_{0.1}\text{Nb}_{0.1}\text{O}_3$, $\text{BaCe}_{0.75}\text{Zr}_{0.15}\text{Nb}_{0.1}\text{O}_3$, and $\text{BaCe}_{0.7}\text{Zr}_{0.2}\text{Nb}_{0.1}\text{O}_3$ sintered at 1450 °C, 1500 °C, 1550 °C and 1600 °C.

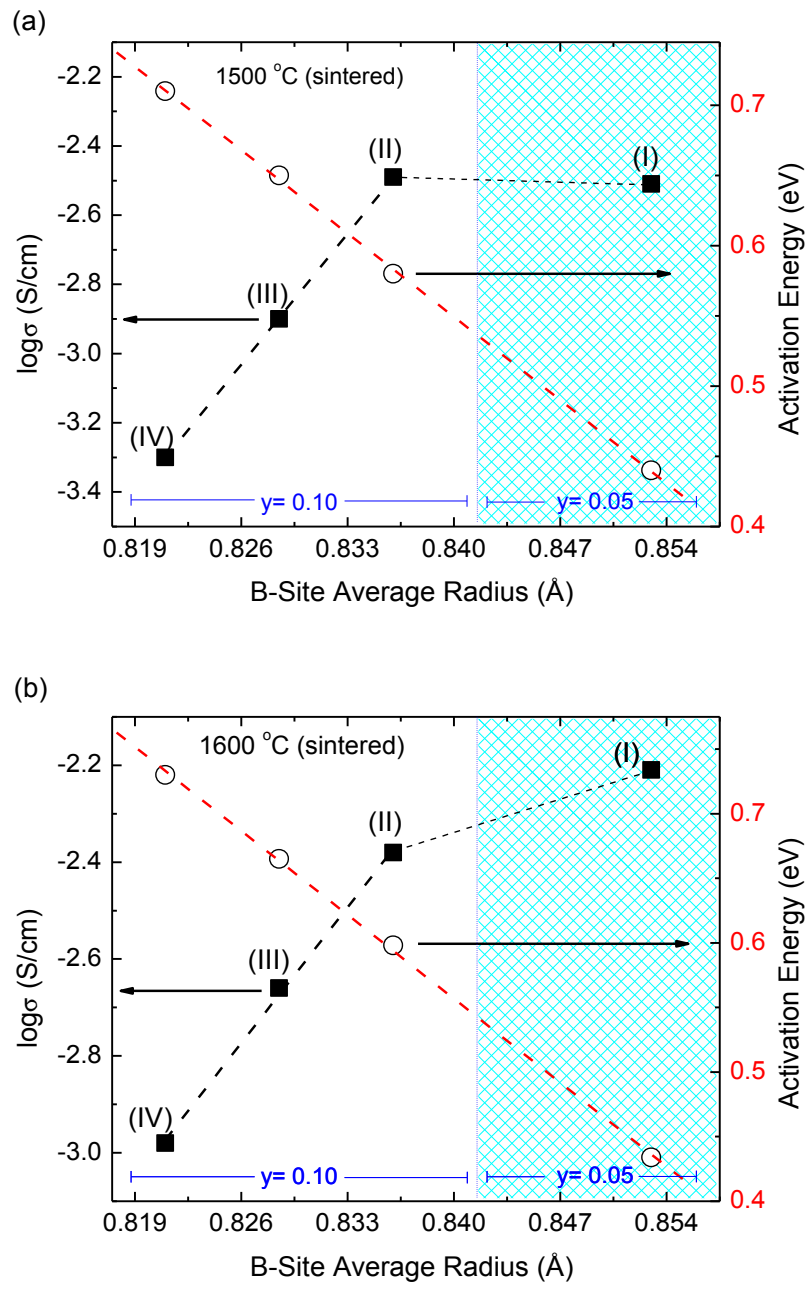


Figure 7.7 Variation of conductivity (■) and bulk activation energy (○) as a function of average B-site ionic radius for $\text{BaCe}_{0.9}\text{Zr}_{0.05}\text{Nb}_{0.05}\text{O}_3$ (I), $\text{BaCe}_{0.8}\text{Zr}_{0.1}\text{Nb}_{0.1}\text{O}_3$ (II), $\text{BaCe}_{0.75}\text{Zr}_{0.15}\text{Nb}_{0.1}\text{O}_3$ (III), $\text{BaCe}_{0.7}\text{Zr}_{0.2}\text{Nb}_{0.1}\text{O}_3$ (IV).

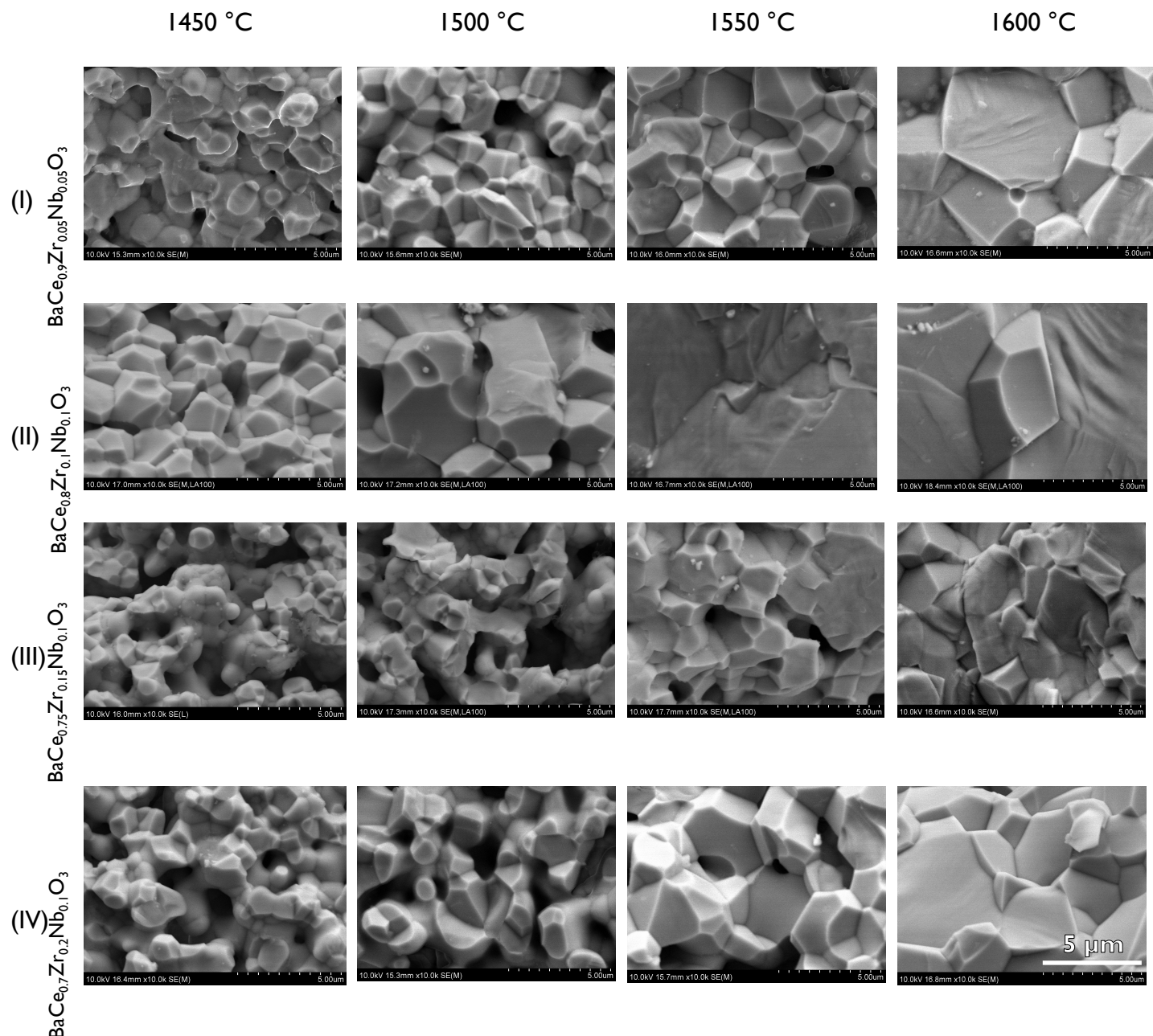


Figure 7.8 Representative 10 kx SEM images of $\text{BaCe}_{0.9}\text{Zr}_{0.05}\text{Nb}_{0.05}\text{O}_3$ (I), $\text{BaCe}_{0.8}\text{Zr}_{0.1}\text{Nb}_{0.1}\text{O}_3$ (II), $\text{BaCe}_{0.75}\text{Zr}_{0.15}\text{Nb}_{0.1}\text{O}_3$ (III) and $\text{BaCe}_{0.7}\text{Zr}_{0.2}\text{Nb}_{0.1}\text{O}_3$ (IV) sintered 1450, 1500, 1550 and 1600 °C.

Table 7.1 Physical and chemical properties of BaCe_{1-x-y}Zr_xNb_yO₃ (x = 0.05; 0.1; 0.15, 0.2; y = 0.05, and 0.1).

Nominal Composition				Sintering Temp. (°C)	Grain Size (μm)	Porosity (%)	Density (XRD; Arch.) (g/cm ³)	σ _B (400 °C) (S/cm)	Ea _(B) (eV)	σ _T (400°C) (S/cm)	σ _B / σ _{GB}	Ea _(T) (eV)	Ea _B /Ea _{GB}
Ba	Ce	Zr	Nb										
1	0.7	0.2	0.1	1450	1.1	38	6.38; 6.26	1.13 x 10 ⁻⁵	0.70	8.33 x 10 ⁻⁷	12.55	1.06	0.59
				1500	1.5	27	6.39; 6.17	1.95 x 10 ⁻⁵	0.71	1.98 x 10 ⁻⁶	8.84	0.98	0.66
				1550	2.1	15	6.39; 6.05	2.99 x 10 ⁻⁵	0.82	3.36 x 10 ⁻⁶	7.92	1.07	0.71
				1600	3.0	Neg.	6.38; 6.09	3.47 x 10 ⁻⁵	0.73	2.34 x 10 ⁻⁶	13.85	1.10	0.61
1	0.75	0.15	0.1	1450	1.4	34	6.39; 6.24	2.22 x 10 ⁻⁵	0.61	9.06 x 10 ⁻⁷	23.52	1.01	0.56
				1500	1.9	29	6.39; 6.12	5.71 x 10 ⁻⁵	0.65	2.88 x 10 ⁻⁶	18.87	1.02	0.60
				1550	3.8	6	6.40; 6.03	7.45 x 10 ⁻⁵	0.65	5.05 x 10 ⁻⁶	13.76	1.01	0.59
				1600	5.4	Neg.	6.39; 6.20	9.21 x 10 ⁻⁵	0.67	3.54 x 10 ⁻⁶	25.06	1.12	0.55
1	0.8	0.1	0.1	1450	1.3	8	6.39; 5.92	1.46 x 10 ⁻⁴	0.60	8.79 x 10 ⁻⁶	15.60	1.00	0.54
				1500	2.7	4	6.41; 5.98	2.12 x 10 ⁻⁴	0.58	1.36 x 10 ⁻⁵	14.58	1.00	0.51
				1550	7.3	2	6.40; 6.23	2.22 x 10 ⁻⁴	0.60	1.83 x 10 ⁻⁵	10.27	1.44	0.48
				1600	11.3	Neg.	6.40; 6.11	2.36 x 10 ⁻⁴	0.60	1.44 x 10 ⁻⁵	15.43	1.04	0.50
1	0.9	0.05	0.05	1450	1.0	29	6.38; 6.19	2.74 x 10 ⁻⁴	0.40	4.16 x 10 ⁻⁶	105.49	1.06	0.36
				1500	1.3	21	6.38; 6.17	4.44 x 10 ⁻⁴	0.44	8.26 x 10 ⁻⁶	52.78	1.00	0.41
				1550	2.0	11	6.38; 6.06	6.60 x 10 ⁻⁴	0.43	1.45 x 10 ⁻⁵	44.54	0.96	0.41
				1600	3.4	Neg.	6.38; 6.12	8.26 x 10 ⁻⁴	0.43	2.15 x 10 ⁻⁵	37.43	0.97	0.40

*Neg. = Negligible

7.3.4 Elemental analysis by EDS and XPS.

Elemental analysis by XPS and EDS is presented in Figure 7.9. EDS analysis (~1.4 um resolution for 20kV accelerating voltage and ~6.4g/cm³ sample density) reveals that the composition of the bulk pellets is stoichiometric at the intermediate compositions for all samples (**I-IV**) at all temperatures (1450-1600 °C) (Fig. 7.9). Surface analysis (~10 nm deep) by XPS, however, reveals departures from stoichiometric values at the surfaces of all samples (Fig. 7.9). The Ba remains stoichiometric at the surface of all compositions at 1450 °C, and in composition **I** at 1600 °C, is deficient in compositions **II-IV** at 1600 °C with up to about 40% Ba deficiency at the surface. Nb enrichment at the B site was found at the surface of all samples at 1600 °C despite only being doped at 5-10 % (Fig 7.9). Determination of oxidation state of multivalent cations reveals that Nb is entirely in the +5 state and Ce is primarily in the +4 state, despite Nb enrichment to nearly 50% of the Ce value which would reduce the Ce to the 3+ if it was the main compensation mechanism. The fixed-valence ions Zr, and O are in +2, +4, and -2 states, as expected. For all measured bulk and surface stoichiometries, the Goldschmidt tolerance factor (Table 7.2) calculated using Eq. 7.2 is 0.94-0.99, indicating a stable pseudocubic or orthorhombic perovskite phase in the bulk and at the surface of all samples.

$$t = \frac{r_A + r_O}{\sqrt{2(r_{B,\text{avg}} + r_O)}}$$

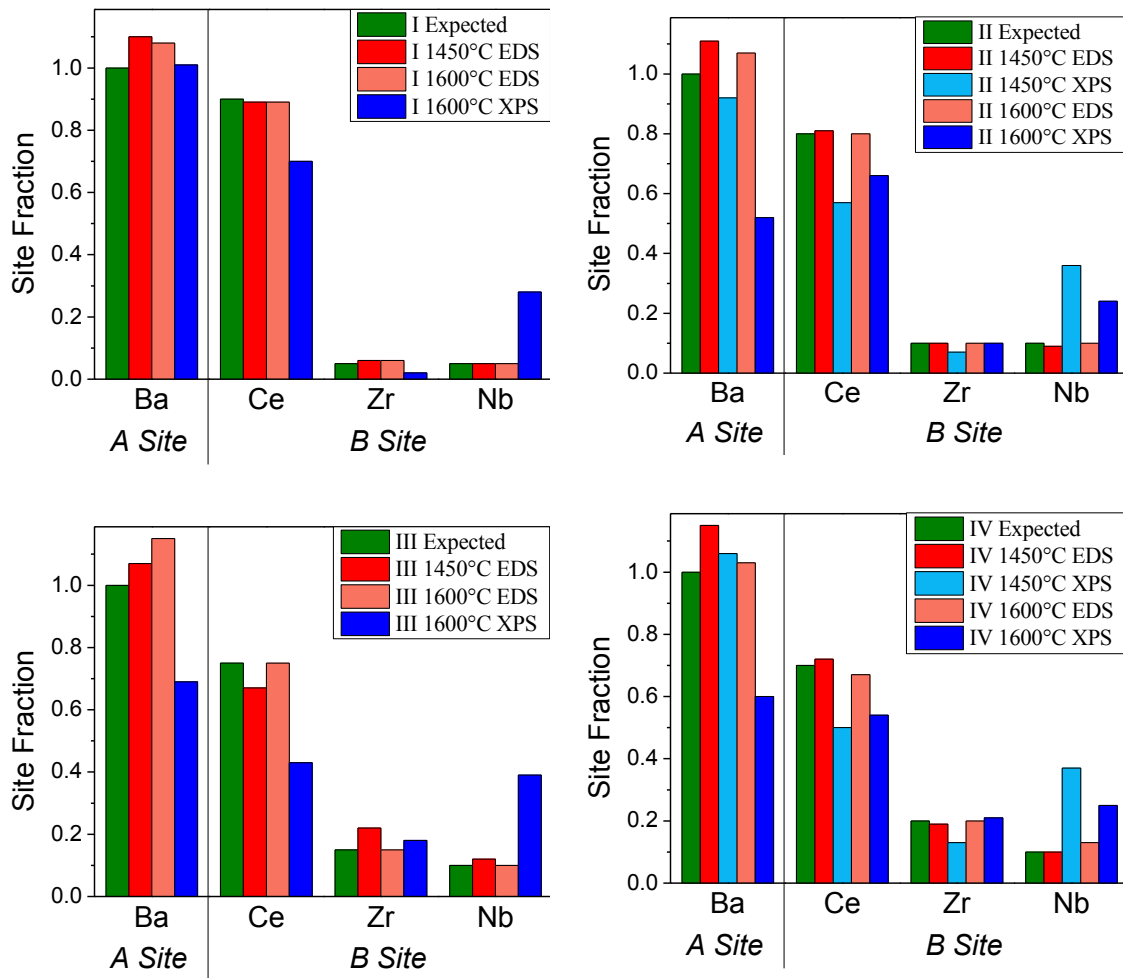


Figure 7.9 Expected stoichiometry of A and B site cations vs. bulk composition by EDS and surface composition by XPS.

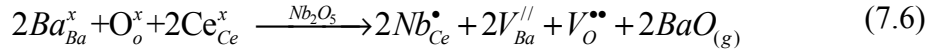
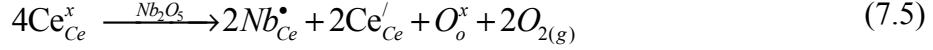
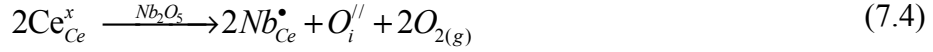
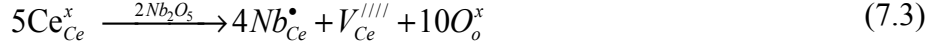
Table 7.2 Expected Stoichiometry vs. Composition Obtained from EDS and XPS Spectra of $\text{BaCe}_{0.9}\text{Zr}_{0.05}\text{Nb}_{0.05}\text{O}_3$ (I), $\text{BaCe}_{0.8}\text{Zr}_{0.1}\text{Nb}_{0.1}\text{O}_3$ (II), $\text{BaCe}_{0.7}\text{Zr}_{0.15}\text{Nb}_{0.15}\text{O}_3$ (III) and $\text{BaCe}_{0.7}\text{Zr}_{0.2}\text{Nb}_{0.1}\text{O}_3$ (IV)

	<u>A Site</u> Ba	Ce	<u>B Site</u> Zr	Nb
I Expected	1.00	0.90	0.05	0.05
I 1450 °C EDS	1.10	0.89	0.06	0.05
I 1600 °C EDS	1.08	0.89	0.06	0.05
I 1600 °C XPS	1.01	0.70	0.02	0.28
II Expected	1.00	0.80	0.1	0.10
II 1450 °C EDS	1.11	0.81	0.10	0.09
II 1450 °C XPS	0.92	0.57	0.07	0.36
II 1600 °C EDS	1.07	0.80	0.10	0.10
II 1600 °C XPS	0.52	0.66	0.10	0.24
III Expected	1.00	0.75	0.15	0.10
III 1450 °C EDS	1.07	0.67	0.22	0.12
III 1600 °C EDS	1.15	0.75	0.15	0.10
III 1600 °C XPS	0.69	0.43	0.18	0.39
IV Expected	1.00	0.70	0.2	0.10
IV 1450 °C EDS	1.15	0.72	0.19	0.10
IV 1450 °C XPS	1.06	0.50	0.13	0.37
IV 1600 °C EDS	1.03	0.67	0.20	0.13
IV 1600 °C XPS	0.60	0.54	0.21	0.25

7.4 Discussion

The cell constant increases linearly with increasing average B-site ionic radius in $\text{BaCe}_{1-(x+y)}\text{Zr}_x\text{Nb}_y\text{O}_3$ and sintering temperature does not affect the lattice constant (Fig. 7.2b). The octahedral ionic radius for Ce^{4+} , Zr^{4+} and Nb^{5+} are 0.87, 0.72 and 0.64 Å, respectively [134]. Increasing Nb and Zr content in $\text{BaCe}_{1-(x+y)}\text{Zr}_x\text{Nb}_y\text{O}_3$ decreases the perovskite-type unit cell volume suggesting Nb and Zr are soluble in the BaCeO_3 and is consistent with earlier report [123]. Also, the PXRD cell parameters suggest that there is likely no reduction of Ce^{4+} to Ce^{3+} since the latter has ionic radius of 1.01 Å for six-fold coordination which would give rise to a lattice volume change that was not observed in

the data [134]. Substitution of pentavalent Nb for tetravalent Ce can be described by the following possible defect reactions:



The formation of interstitial oxygen atoms are energetically unfavourable since oxygen anions are too large to fit on any interstitial site [135]. Furthermore, Ce-rich secondary phases were not observed in XRD or EDS, so their concentration is negligible under the present synthesis condition. Equations 7.4 or 7.5 must satisfy charge balance in these samples. In order to understand the potential Ce^{4+} reduction and Ba vacancy formation, we have performed XPS on as-prepared samples. Figure 9a shows the XPS spectra of $\text{BaCe}_{0.9}\text{Zr}_{0.05}\text{Nb}_{0.05}\text{O}_3$ (**I**), $\text{BaCe}_{0.8}\text{Zr}_{0.1}\text{Nb}_{0.1}\text{O}_3$ (**II**), $\text{BaCe}_{0.75}\text{Zr}_{0.15}\text{Nb}_{0.1}\text{O}_3$ (**III**) and $\text{BaCe}_{0.7}\text{Zr}_{0.2}\text{Nb}_{0.1}\text{O}_3$ (**IV**) sintered at 1450-1600 °C in air for 4 h. There is no significant evidence of Ce^{3+} observed using XPS, while oxidation states of Nb, Zr and Ba were found to be +5, +4 and +2, respectively. For reference, XPS analysis of commercial CeO_2 (99.99 % Alfa Asear) was performed to further confirm absence of Ce^{3+} in $\text{BaCe}_{1-(x+y)}\text{Zr}_x\text{Nb}_y\text{O}_3$.

The oxidation state data reveals that Ce^{4+} reduction cannot entirely explain the charge compensation for Nb^{5+} at the B-site. The Nb enrichment at the surface of the samples reaches values ~50% of that of the Ce concentration, so 50% of the Ce^{4+} would be expected to reduce to Ce^{3+} to compensate. No Ce^{3+} was detected within the resolution

of the XPS data, however, so the excess charge must be compensated for by another mechanism. The elemental analysis shows a variation in the Ba content relative to the nominal composition (Figure 7.9). Haile et al. proposed similar defect formation for Gd-BaCeO₃ prepared at 1550 C in air [136]. It is also important to mention that A-site vacancy (up to 100 %) is commonly reported for perovskite-related structures including ReO₃, La_{1/3}NbO₃ and La_{2/3}TiO₃. Therefore, we believe that Ba-vacancy at grain boundaries is the dominant defect in the donor-doped perovskites, as described in Equation 7.6.

For metal oxides, the electrical conduction observed in air may be considered as a sum of electronic and oxide ion conductivities. The bulk electrical conductivity decreases with increasing Zr content. At a fixed sintering temperature, a specific composition in BaCe_{1-(x+y)}Zr_xNb_yO₃, shows that bulk and total conductivity are on the same order of magnitude and variation is found to be rather small (Table 7.1). The density of the sample reached nearly theoretical density at higher temperatures while the ratio of bulk to grain-boundary conductivity decreases with increasing sintering temperature, as anticipated. The electrical conductivity in dry N₂ was found to be lower than that of air suggesting p-type electronic conduction in BaCe_{1-(x+y)}Zr_xNb_yO₃ and it can be expressed using the generic defect equilibrium reaction:



Therefore, the presence of oxide ion vacancies to balance the Ba vacancies is further supported by the electrical measurements.

The chemical stability of donor-doped $\text{BaCe}_{1-(x+y)}\text{Zr}_x\text{Nb}_y\text{O}_3$ under CO_2 at elevated temperature strongly depends on the B site substitution of Nb and Zr for Ce. The Pauling electronegativity of B-site cations Ce, Zr, and Nb are 1.12, 1.3, and 1.6, respectively, while the A-site cation Ba is 0.89. The more electronegative Zr is known to enhance stability of barium cerates [6, 10], and Nb may play a further role since it is even more electronegative than Zr. Clear evidence of deleterious barium carbonate formation was observed in the in-situ TGA analysis for composition I with the lowest doping level and minor reaction occurred for composition II, but composition III-IV are entirely stable (Figure 7.10). This implies that co-doping of >10% Zr with >10% Nb is required for bulk perovskite stability.

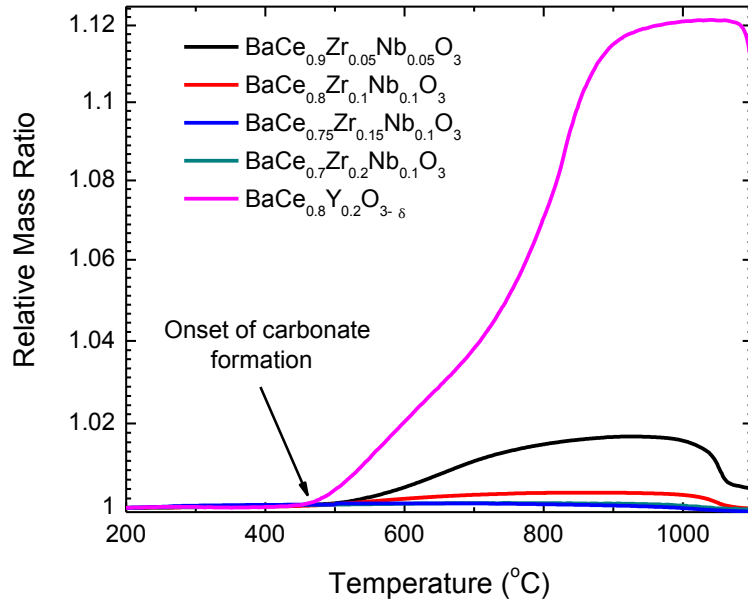


Figure 7.10 In-situ TGA analysis showing the chemical stability of $\text{BaCe}_{0.9}\text{Zr}_{0.05}\text{Nb}_{0.05}\text{O}_3$, $\text{BaCe}_{0.8}\text{Zr}_{0.1}\text{Nb}_{0.1}\text{O}_3$, $\text{BaCe}_{0.75}\text{Zr}_{0.15}\text{Nb}_{0.1}\text{O}_3$ and $\text{BaCe}_{0.7}\text{Zr}_{0.2}\text{Nb}_{0.1}\text{O}_3$ in 30 % CO_2 balanced by N_2 atmosphere. For comparison, chemical stability of benchmark high temperature proton conductor Y-doped BaCeO_3 is included. Carbonates are driven off >1040°C, in agreement with thermodynamic equilibrium calculations [10].

Unfortunately, at the high doping concentration required for stability of the bulk material, the bulk conductivity decreases by nearly an order of magnitude. This is an undesirable tradeoff, since high conductivity is required for the material to be a good anode or electrolyte. The surface enrichment of Nb observed by XPS gives a possible method of ameliorating this tradeoff. The surface of even the lowest doped material (Composition I) has a greater Nb concentration than the highest doped material in this study (Composition IV). The surface enrichment occurs during high temperature sintering, and is disrupted when grinding the material into powder for the TGA study. Comparing loose powder that has been fired to cause surface enrichment and requires no subsequent grinding to the bulk composition from a pellet ground into powder after firing in Figure 7.11 reveals that the surface enrichment renders the material as stable in CO₂ as the higher doped material.

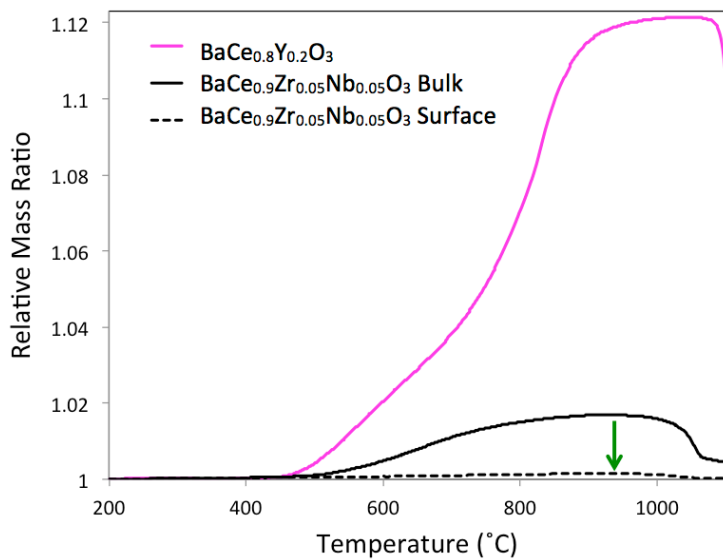


Figure 7.11 In-situ TGA plot showing the enhanced stability in CO₂ of the Nb enriched surface of BaCe_{0.9}Zr_{0.05}Nb_{0.05}O₃ (I) powder (dashed line, SSA = 0.56 m²/g) compared to a powder of its bulk composition (solid line, SSA = 0.51 m²/g).

This decrease in surface reactivity means that the bulk of the material can maintain high conductivity while the surface is stable to CO₂, thereby escaping the inherent tradeoff between bulk conductivity and bulk stability of doped BaCeO₃ materials.

7.5 Conclusions

The present study clearly shows that donor-doped BaCe_{1-(x+y)}Zr_xNb_yO₃ can be prepared by solid state reaction at 1450-1600°C in air, confirmed by the orthorhombic lattice volume decreasing with decreasing average B-site cation radii. The crystallite size increases with increasing sintering temperature and the highest sintering temperature of 1600 °C showed a dense structure with negligible porosity. The density of each sample was found to reach nearly the theoretical density for 1450 °C samples. The bulk and total electrical conductivities were found to change by an order of magnitude with chemical composition and also by up to half an order of magnitude due to sintering temperature. The total activation energy is only affected by composition and is inversely proportional with B-site radius with a very good fit, indicating that higher dopant concentrations cause decreased conductivity. The chemical stability of BaCe_{1-(x+y)}Zr_xNb_yO₃ is improved by higher electronegativity Zr and Nb substituting for Ce sites preventing formation of BaCO₃, and surface enrichment of Nb can be used to protect the bulk material.

Chapter 8: Conclusions

The work summarized in this dissertation focuses on developing and characterizing SOFC anodes for lower temperature operation on hydrocarbon fuels. A broad approach has been used, starting with an extensive thermodynamic analysis of the parameter space for hydrocarbon and reformate fueling, and concluding with development and characterization of a new anode scaffold and anode materials that limit coke formation.

Thermodynamic equilibria of the gaseous fuel under SOFC operating conditions highlight the differences between hydrogen and hydrocarbon fueling. Hydrocarbon fuels can deposit solid carbon in the anode through several reactions which limits their direct use in SOFCs, and the dominant mechanisms change between 650 -710 °C. This can be most effectively alleviated by a high fuel utilization or by steam reforming the fuel. The Nernst voltage for methane fueling is found to be more stable at temperatures below 650 °C than it is for H₂, with only a ~13% decrease in Nernst voltage at 95% fuel utilization.

Operating SOFCs with Ni-GDC cermet anodes on reformed hydrocarbons is found to be comparable in performance to operating on H₂ fuel under certain conditions. At temperatures \leq 600 °C, the MPD of an SOFC running on steam reformed CH₄ is within 5% of that of a H₂ fueled cell. At 650 °C, more severe concentration polarization is observed in all reformed fueling cases due to the greater current density through the electrolyte. The OCV of cells operating on reformed hydrocarbons deviates minimally from the value in H₂ fuel, which is unexpected based on the calculated changes in Nernst OCV of the cells. No carbon deposition is observed for the reformate compositions for

which no carbon formation is expected by thermodynamic equilibrium, confirming that the kinetics of carbon formation match the expected equilibria between 500 – 650 °C.

The mechanical strength of porous GDC and YSZ are extensively characterized. The porosity decreases the flexural strength of the ceramics following an empirical fitting parameter that is more strongly affected by material processing than by the material itself. The volume and morphology of pores are precisely controllable using pyrolyzable spherical pore formers that also assist with crack blunting in the ceramic. Metals infiltrated into the porous ceramic monolith increase its electronic conductance to > 1000 S/cm, the same order of magnitude as Ni-GDC cermets, at 70% less metal loading. Ni and Cu do not oxidize at any temperature or fuel utilization conditions studied, but Co oxidizes at high fuel utilizations and should be avoided in SOFC anodes.

SOFCS using GDC scaffold anodes infiltrated with Ni demonstrate a MPD within 15% of that of conventional cermet anode cells using hydrogen as a fuel at 650 °C. These GDC scaffold anode cells are stable when fueling with direct CH₄, whereas conventional cermet anodes are not. The difference in stability relates to the greater oxygen availability at the anode surfaces in the GDC scaffold anode.

Barium cerate is doped with Zr and Nb to introduce mixed protonic and electronic conductivity, as well as improve its chemical stability in CO₂. Co-doping with 10% Nb and >10% Zr on the B-site of the perovskite is required to prevent degradation of the bulk material in CO₂, which causes up to an order of magnitude decrease in total conductivity of the material. Surface enrichment of Nb promoted by elastic driving forces at high temperature, however, allows lower dopant concentrations of Zr and Nb to prevent degradation of the material in CO₂ by forming a protective surface layer.

8.1 Resulting Publications

C. M. Gore et al., Mechanical and Electrical Properties of Ceramic Electrodes for Solid Oxide Fuel Cells, ECS Trans., **64**, 65 (2014).

C.M. Gore et al., Effect of composition and microstructure on electrical properties and CO₂ stability of donor-doped, proton conducting BaCe_{1-(x+y)}Zr_xNb_yO₃. Journal of Materials Chemistry A, 2014. **2**(7): p. 2363-2373.

C.M. Gore et al., Effect of Composition and Atmosphere on Electrical Properties of Donor-doped BaCe_{1-(x+y)}Zr_xNb_yO₃. ECS Transactions, 2013. **58**(2): p. 147-152.

C.M. Gore et al., Porous GDC Scaffold Anodes for Lower Temperature, Hydrocarbon-Fueled Solid Oxide Fuel Cells. ECS Transactions, 2013. **50**(27): p. 53-62.

K.T. Lee, C.M. Gore, and E.D. Wachsman, Feasibility of low temperature solid oxide fuel cells operating on reformed hydrocarbon fuels. Journal of Materials Chemistry, 2012. **22**(42): p. 22405-22408.

Appendix A: Software and Programming Scripts Used for Thermodynamic Calculations

The thermodynamic calculations used in this study were performed using Python 2.7 scripts to utilize functions in Cantera 2.1.1, an open source chemical kinetics and thermodynamics package developed by the late David Goodwin [36]. The NASA polynomials for 325 reactions among 53 species related to methane oxidation are used from GRI Mech 3.0, developed by the Gas Research Institute at UC Berkeley, Stanford, and SRI. A custom script was developed in-house to iterate calculations of equilibrium concentrations for each species as well as the resulting Nernst voltage of a SOFC operating with excess air at small temperature and composition steps. The resulting data is plotted in Origin 8.5 as the contour maps presented in Chapter 3.

A sample of the code is given below:

```
"""
Equilibrium composition and PO2 for a fuel mixture
as a function of temperature, including formation of solid carbon.
written by Colin Gore, University of Maryland (colin.gore@gmail.com)
"""

import cantera as ct
import numpy as np
import sys
import csv
from datetime import datetime

#####
# Edit these parameters to change the temperature, the pressure,
# the phases in the mixture and the number of temperature and
# composition iterations.

Ti = 1273
P = ct.one_atm
ntemps = 17
mcomps=1
```

```

# phases
gas = ct.Solution('gri30.xml')
carbon = ct.Solution('graphite.xml')

# the phases that will be included in the calculation, and their
initial moles
mix_phases = [(gas, 1.0), (carbon, 0.0)]

#define mixture
mix = ct.Mixture(mix_phases)

# set start time and number of convergence errors
t_start = datetime.now()
errors = 0

#####
#####

csv_file = '75%H2-H2O OCV.csv'
with open(csv_file,'a') as csvfile:
    writer = csv.writer(csvfile)

    for m in range(mcomps):
        if m<1:
            c=0 # 0 species must be nonzero for OCV plots, or OCV ->
infinity
        else:
            c=5*m
        # composition values are integers, so must not use decimals
        CH4 = 0
        CO = 0
        CO2 = 0
        H2 = 25
        H2O = 75
        C3H8 = 0
        O2 = 0
        O = 0
        C = 0
        H = 0
        N2 = 0
        AR = 0

        writer.writerow(['T (degC)', 'PO2 (atm)', 'Nernst OCV', 'Mols
Exhaust/Mols Inlet', 'mols of:' + mix.species_names])
        print 'T      PO2          OCV'

        for n in range(ntemps):
            T = Ti - n*50

            gas.X = 'CH4:{0}, CO:{1}, CO2:{2}, H2:{3}, C3H8:{4}, H2O:{5}, O:{6},
N2:{7}, AR:{8}, O2:{9}, C:{10},
H:{11}'.format(CH4,CO,CO2,H2,C3H8,H2O,O,N2,AR,O2,C,H)

            # the phases that will be included in the calculation, and
their initial moles
            mix_phases = [(gas, 1.0), (carbon, 0.0)]

```

```

#define mixture
mix = ct.Mixture(mix_phases)

#write initial composition on first iteration of loop
before equilibrating
if n < 1:
    writer.writerow(['', '', '', '' , 'initial composition']
+ list(mix.species_moles))

# set the gas state
gas.TP = T, P

# create a mixture of 1 mole of gas, and 0 moles of solid
carbon.
mix = ct.Mixture(mix_phases)
mix.T = T
mix.P = ct.one_atm

# equilibrate the mixture at constant P and T
try:
    mols_in = np.sum(mix.species_moles)
    mix.equilibrated('TP', solver='gibbs', max_steps=100000)
    PO2 = gas['O2'].X
    mols_out = np.sum(mix.species_moles)
    nernst_OCV =
ct.gas_constant*T/(4*ct.faraday)*np.log(0.2095/PO2)
#RT/4F*ln(PO2_Hi/PO2_Lo)
    print T-273, PO2[0], nernst_OCV[0]
    exhaust_ratio = mols_out/mols_in

    #numpy creates 1x1 arrays for these, so you need to
call position '0' in that array to get a float
    writer.writerow([T-273 , PO2[0], nernst_OCV[0],
exhaust_ratio , '' ] + list(mix.species_moles))

except RuntimeError: #if equilibrate fails to converge
    errors += 1
    print "Errors = ", errors

writer.writerow('')

total_time = datetime.now() - t_start
print('Output written to {0}'.format(csv_file))
print "Completed in ", total_time.total_seconds(), "seconds with",
errors, "failed convergence value(s)"

```

Appendix B: Example Recipes for Ceramic Slurries

Solvents and binder systems were chosen for the tape casting slurry recipes based on their solubility and boiling point. The Hildebrand solubility parameter was used to ensure the solvent system would dissolve the binders, but not the PMMA pore formers [137]. The parameters and example recipes are given below:

Table B1: Solubility parameter, boiling point and density of binders and solvents

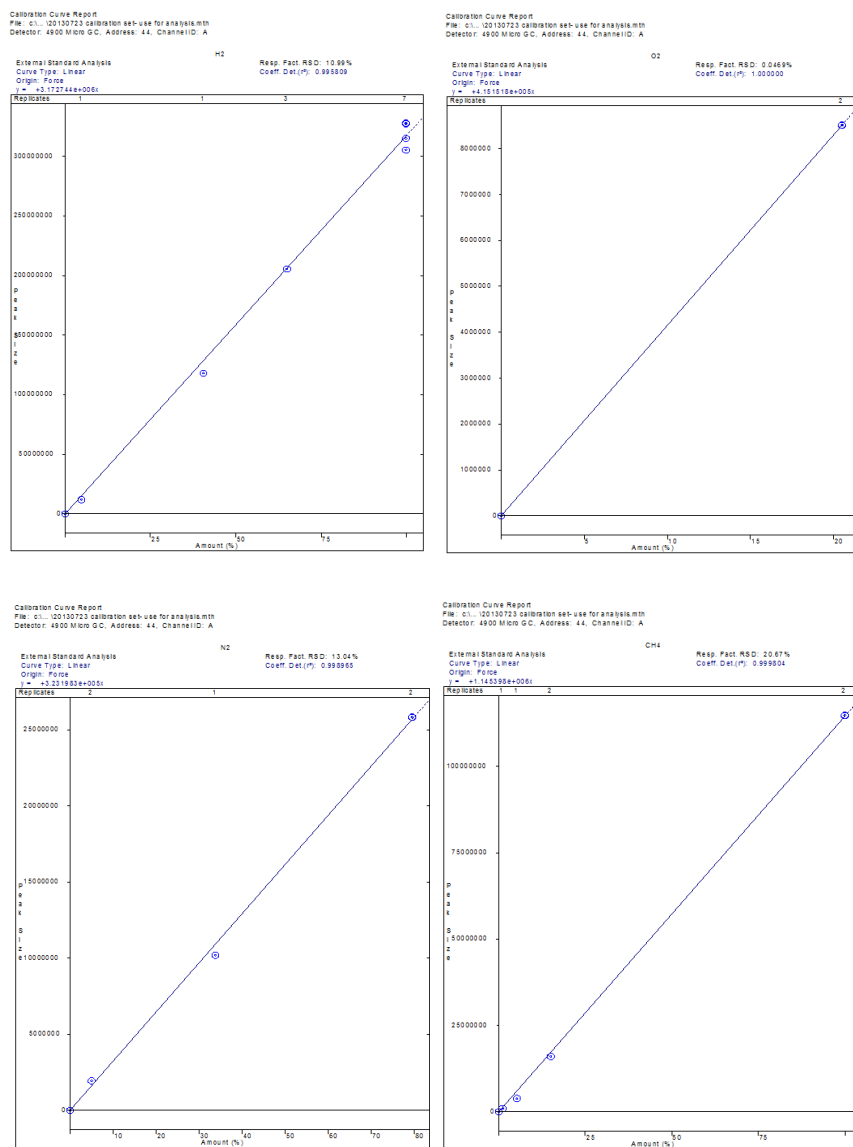
	Purpose	Hildebrand Solubility Parameter (MPa ^{0.5})	Boiling Point (°C)	Density (g/cc)
Ethanol	Solvent	26.2	78.4	0.789
Toluene	Solvent	18.3	110.6	0.866
Fish Oil	Dispersant			0.93
BBP	Plasticizer	20.2	370	1.1
PVB- B98	Binder (Dispersant)	21- 25.6		1.1
PEG 8000	Plasticizer	24	200	1.08
PMMA	Pore Former	18.5	200	1.18
Water	Solvent	48	100	1

Table B2: Sample recipes for porous ceramic scaffolds anodes

ID V	Solvent		Dispersant	Ceramic	Binder and Plasticizer			Pore Former				Viscosity (cP)
Batch #	Ethanol	Toluene	Fish Oil	GDC 10	PVB	BBP	PEG	MX2000	MX1000	MX500	MP300	
Material Density >	0.789 g/cm3	0.866 g/cm3	0.923 g/cm3	7.2g/cm3	1.08 g/cm3	1.10 g/cm3	1.09 g/cm3	1.18 g/cm3	1.18 g/cm3	1.18 g/cm3	1.18 g/cm3	
10	60	-	3	75	12	12	1.5	-		12.3g (50vol%)		
11	40	-	2	50				-	8.2g (50vol%)			
12	40g	-	2g	50g	6g	6g	0.8g	-	12.3g (60vol%)			8528
13	40g	-	2g	50g	6g	6g	0.8g	-	12.3g (60vol%)			
17	40g	-	2g	50g	6g	6g	0.75g	-	12.3g (60vol%)	-	-	
18	40g	-	2g	50g	6g	6g	0.75g	-	-	12.3g (60vol%)	-	-
19	40g	-	2g	50g	6g	6g	1g	-	-	8.2g (50vol%)	-	
20	40g	-	2g	50g	6g	6g	1g	-	-	6.6g	1.6g	8500
21	45.5g	11.0g	2g	50g	6g	6g	1g	-	8.2g (50vol%)	-	-	3500
22	40g	-	2g	50g	6g	6g	1g	-	-	19.1g (70vol%)	-	
24	40	-	2g	50	6	6	1	12.3 (60vol%)	-	-	-	
25	40g	-	2g	50g	6g	6g	1g		-	19.1g (70vol%)	-	
26	40g	-	2g	50g	6g	8g	1g			24.7g (75vol%)		

Appendix C: Gas Chromatograph Calibration

A Varian CP-4900 gas chromatograph was calibrated using Star Workstation software V 3.5. Porous layer open tubular and 5Å molecular sieve columns are used in parallel with used Ar and He carrier gases. Both columns use thermal conductivity detectors. The calibration report for the instrument is as follows for H₂, O₂, N₂, CH₄, CO, CO₂, H₂O, and H₂S.



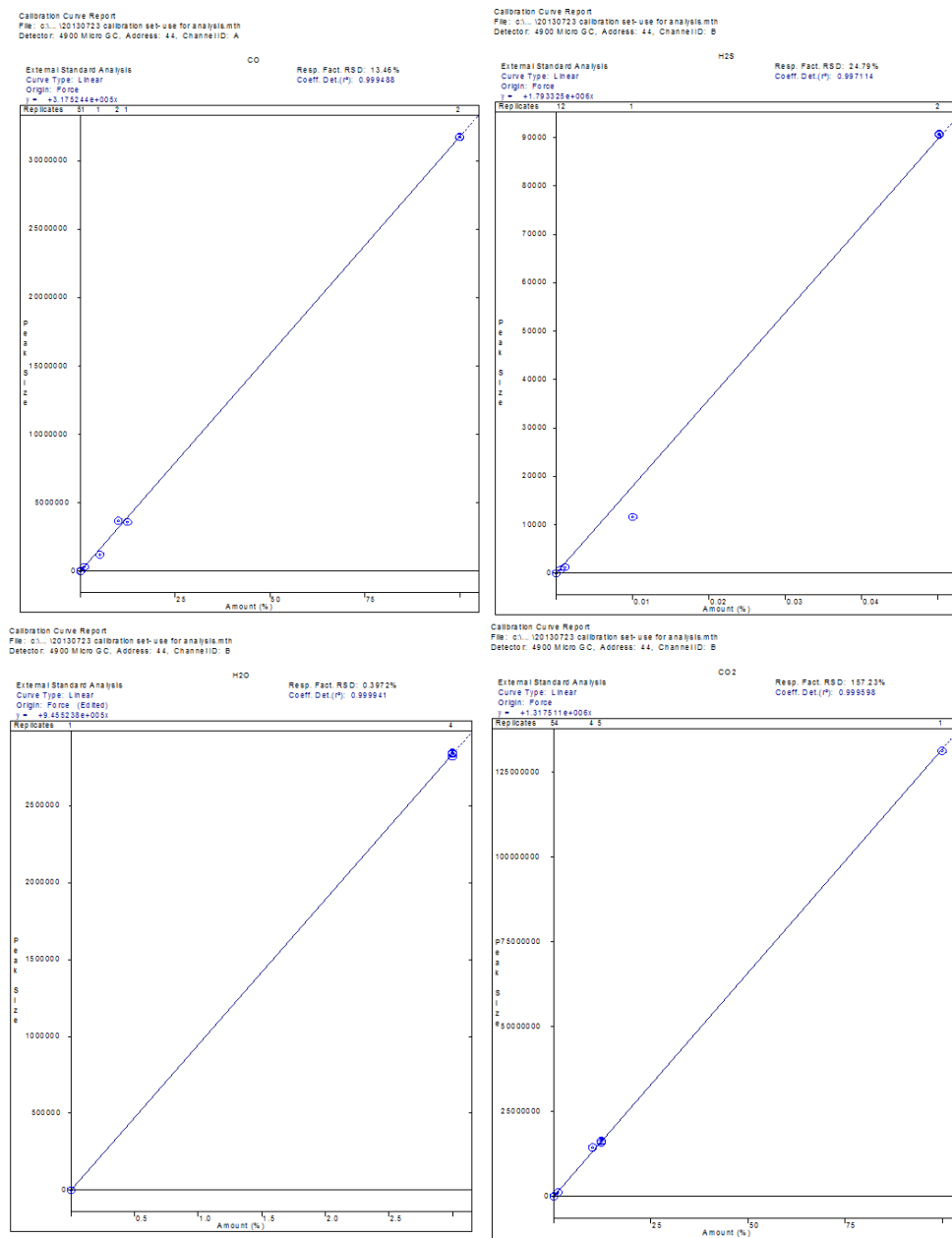


Figure C1: Calibration report showing peak area vs. concentration of species in the calibration gases used.

Appendix D: Diagnosing SOFC Testing Artifacts

The conditions under which SOFCs are tested can have a significant impact on the measured responses. SOFCs are heated as current flows through them, both because hydrogen oxidation is exothermic and due to Joule heating from the resistance of the electrodes and electrolyte. The heating of the SOFC affects the response of the cell during galvanic sweep measurements, as observed in Figure D1. Slower current ramp rates lead to greater heating, which causes a lower measured ASR at current density $>3.5 \text{ A/cm}^2$. For a clean measurement, it is important to select a ramp rate that is fast enough to avoid SOFC heating, but slow enough to ensure equilibrium is reached at the electrodes. In Figure D1, the effect is minimal at current densities $<3.5 \text{ A/cm}^2$.

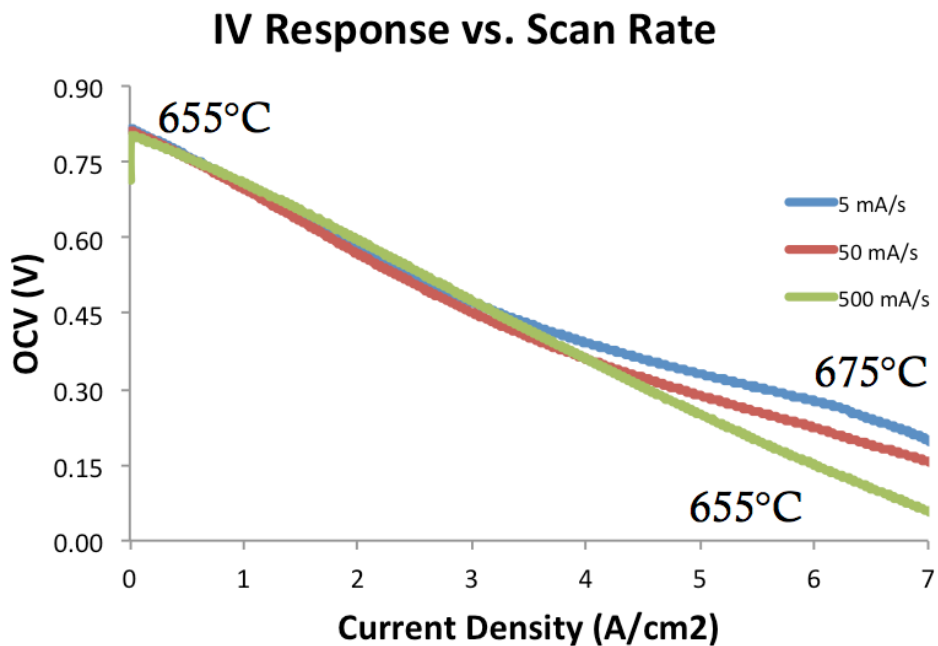


Figure D1: Change in current-voltage response and SOFC temperature resulting from different galvanic sweep rates in H_2 fuel at 650°C .

An artifact of testing SOFCs on reformed fuels is the noise in voltage or current measurements (Figure D2) caused by the introduction of steam to the anode atmosphere. The noise makes low frequency EIS measurements difficult to resolve, so the total ASR of an SOFC operating on steam-reformed fuels must often be determined by the slope of the current-voltage plot using Ohm's law.

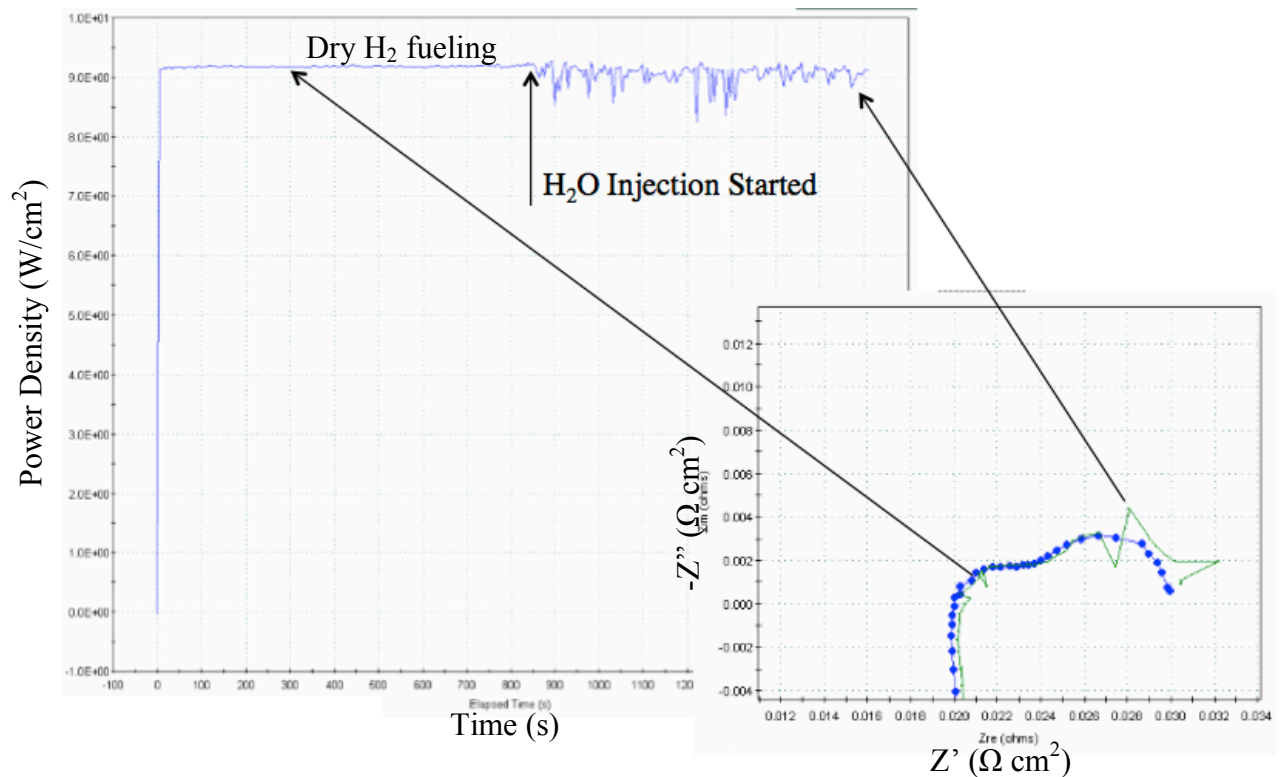
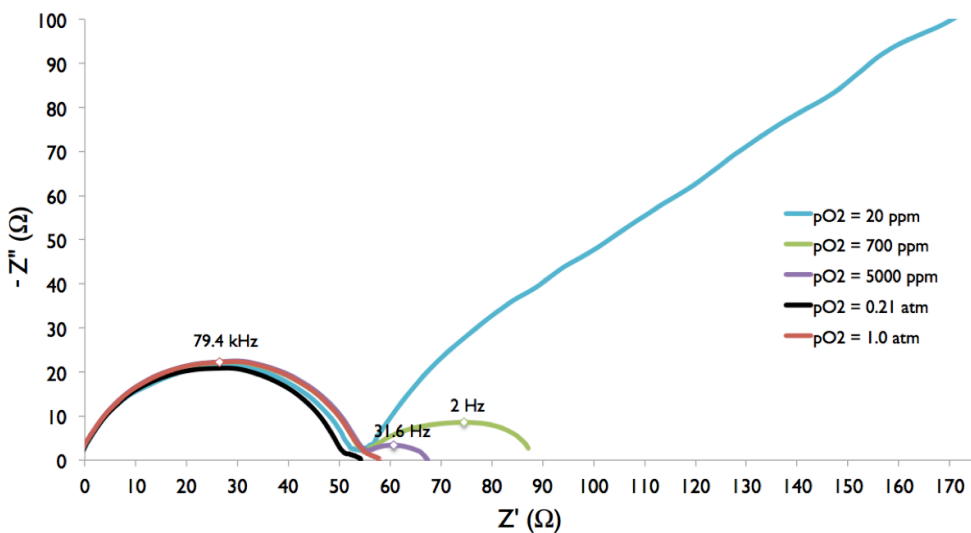


Figure D2: Noise in power density measurement caused by the introduction of steam to the fuel of an SOFC operating at 650 °C.

Appendix E: Determining Pt Electrode Contributions to Electrochemical Impedance Spectroscopy Measurements of Material Properties

For material data measured in Chapter 7, EIS in atmospheres from a PO₂ of 20 ppm (ultra high purity N₂) to a pO₂ of 1.0 (ultra high purity oxygen) had been conducted at the beginning of the study to ensure electrode effects are accounted for. Sample data is shown below for a BaCe_{0.8}Zr_{0.1}Nb_{0.1}O₃ pellet at 700 °C, 100 mV AC oscillation from 10⁶ to 10⁻¹ Hz. Note that bulk resistance was subtracted in this particular figure to compare the semicircles. The PO₂ was confirmed using a YSZ sensor (Zirox SGM5).



The study reveals an additional low-frequency electrode process (semicircle with capacitance of $\sim 10^{-4}$ to 10^{-5} F, in agreement with electrode capacitance in literature) at $PO_2 << 0.21$, becoming a Warburg element at 20 ppm. That electrode effect is too small to be resolved at $PO_2=0.21$ when compared to $pO_2=1.0$, so we are confidant that the

electrode process does not impact our presented data significantly. The minor shifts in the GB semicircle response result from the different flowrates of gases at each PO₂ causing minor temperature inhomogeneity between the thermocouple next to the sample and the sample itself, but all data used in the paper is collected in still air so is not subject to that additional error. Characteristic frequencies for each semicircle have been added to figures 7.3 & 7.4 that clearly show high frequency processes with nanofarad capacitances, thus the electrode effect can be ruled out as a major contributor to the calculated conductivities.

Appendix F: Correcting Peak Overlaps in BaCeO₃ XPS Spectra

Dr. Karen Gaskell at the University of Maryland Surface Analysis Center did the majority of the development of this deconvolution method for XPS measurements of BaCeO₃ materials. For both Mg K α and Al K α sources, overlaps between Ba and Ce photoemission and Auger emission lines convolute the interpretation of peak intensities. Standards were used to develop a correction method. No other XPS results from BaCeO₃ based materials in literature mention a similar correction factor, thus they may be significantly overestimating Ce concentration.

XPS Analysis Details:

XPS spectra were acquired using a Kratos Axis 165 x-ray photoelectron spectrometer operating in the hybrid mode using Al K α radiation (1486.6 eV) at 280W (14kV 20mA). The ceramic samples were run using a charge neutralization of 2.5V. The instrument was run in hybrid mode with a pass energy of 160 eV for survey spectra (Figure F1 & F3) and a pass energy of 20 eV for high-resolution spectra (F2 & F4). Peak energies were calibrated to the adventitious carbon C 1s peak centered at 284.8 eV. Peak fittings were performed using CasaXPS software.

Measured spin-orbit split peak doublet areas from high resolution scans from each cation's 3d spectra were fit ensuring a proper 2:3 area ratio between the 3d_{3/2} and 3d_{5/2} peaks and proper peak separation energy (15.4 eV for Ba, 18.3 eV for Ce, 2.4 eV for Zr, and 2.8 eV for Nb) [138]. Shirley backgrounds were applied to all but Ce, which required

a linear background as is common in literature [139]. The areas were modified by the appropriate relative sensitivity factor for each element from the Kratos library (0.278 for C, 0.780 for O, 7.469 for Ba, 8.808 for Ce, 2.576 for Zr, and 2.921 for Nb), and the resulting atomic percent for each were calculated.

Correction for Ba auger contribution to measured Ce 3d peaks:

Ba has auger peaks that overlap with Ce 3d peaks when using an Al K α source. Reference samples of CeO₂ and BaCeO₃ were used to correct for the overlap. BaCeO₃ and CeO₂ both contain Ce entirely in the 4+ oxidation state and the Ce to Ba ratio in BaCeO₃ is 1:1, so the Ce 3d peak envelope from the CeO₂ spectra was scaled appropriately to fit the peak intensity at 916 eV in the Ce 3d high resolution scan of BaCeO₃, then subtracted from the BaCeO₃ Ce 3d peak envelope to leave only the Ba auger peak contribution (Figure F4). A correction factor for the Ce peak area was derived using this data. The overlapping Ba auger peak area was found to scale proportionally as 0.893 of the Ba 3d peak area, thus can be subtracted using:

$$I_{\text{Ce 3d, corrected}} = I_{\text{Ce 3d, measured}} - I_{\text{Ba 3d}} * 0.893$$

All measured Ce peak areas have been corrected using this method before calculating stoichiometry. Since B-site cations are not volatile, B-site deficiency was not feasible via any defect equilibria, and since B-site cations are too small to occupy an A-site position, the sum of Ce, Zr, and Nb were safely assumed to add to an occupancy of 1 on the B-site. The Ba stoichiometry was then found by the A:B site ratio (proportion of Ba cations to Ce+Zr+Nb cations), revealing Ba deficiency in many cases.

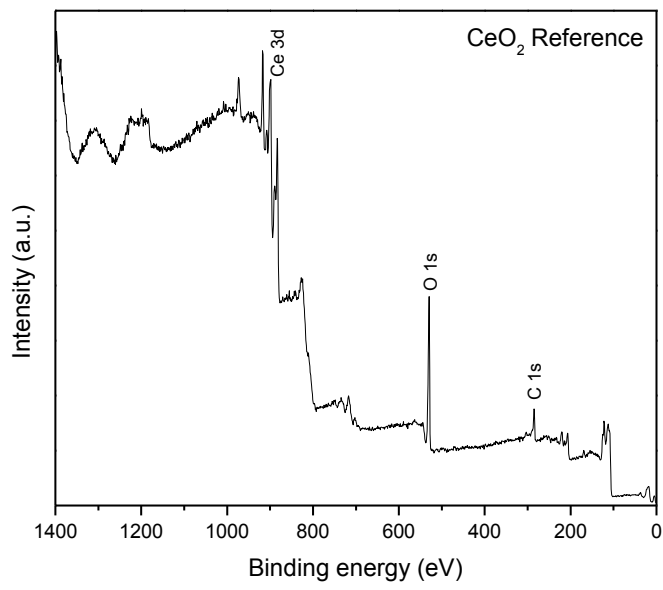


Figure F1: CeO₂ Survey Spectrum

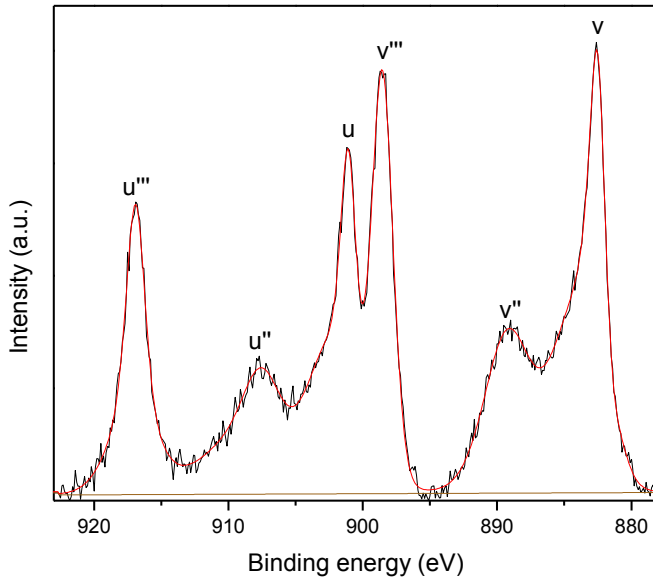


Figure F2: CeO₂ 3d peaks and satellite peaks. Envelope used in Fig. S4 is highlighted in red.

Ceria gives a complex set of satellite peaks around its 3d peaks associated with shake-up/shake-down. Each pair of satellite peak pairs (u'' & v'' , u''' & v''') have the same 18.3 eV separation and 2:3 peak area ratio as the main 3d peaks. The sharp u''' peak at ~916 eV is only associated with the Ce⁴⁺ oxidation state, and is useful in characterizing the oxidation state of the Ce in doped samples[140].

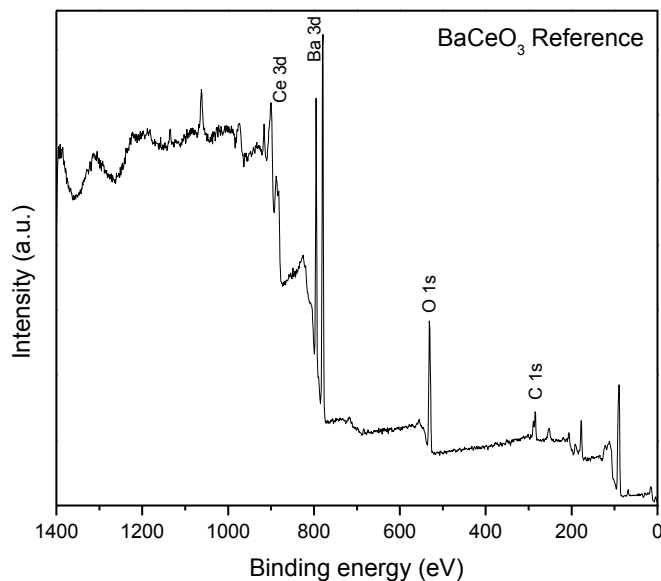


Figure F3: BaCeO₃ Survey Spectrum

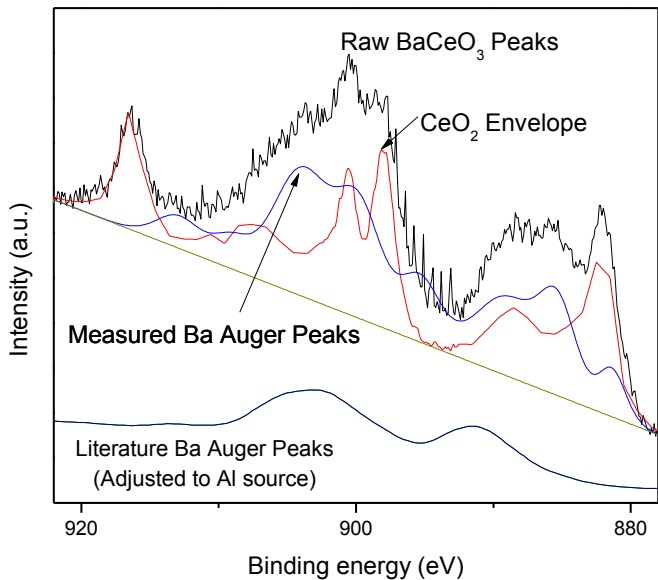


Figure F4: High resolution scan of CeO_2 peaks in BaCeO_3 .

In Figure F4, the CeO_2 peak envelope from Figure F2 is subtracted from the raw peak data. This yields the peak shape attributed to the Ba auger peaks, which is confirmed to fit the expected peak energies of 901.7 eV and 888.9 eV calculated from the Ba auger peak data in Figure F5. Minor irregularity stems from different background types.

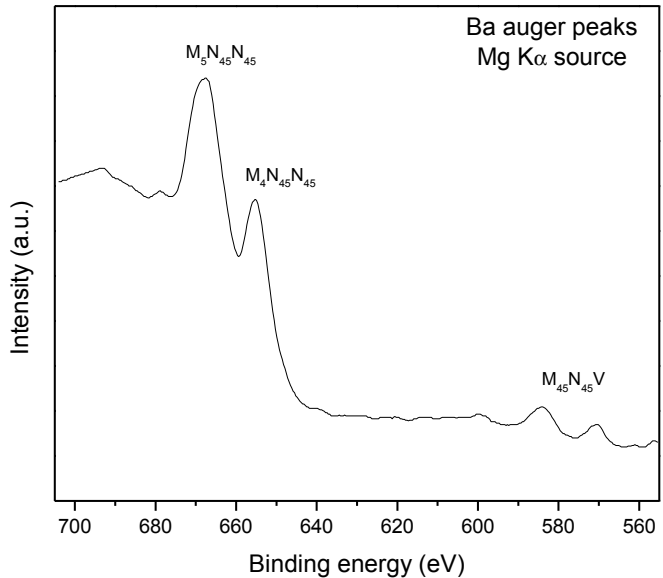


Figure F5: Measured Ba auger peaks using a Mg K α source (from [138])

Reference spectra for Ba auger peaks are available from a Mg K α x-ray source (1253.7 eV), shown in Figure F5. Auger peaks from an Al K α x-ray source will be at 233 eV higher peak energies due to the higher energy source. Energy-adjusted Ba auger peaks from F5 are plotted in F4 for comparison to measured auger peaks, revealing good agreement in position and peak shape.

Bibliography

1. E. D. Wachsman and K. T. Lee, *Lowering the Temperature of Solid Oxide Fuel Cells*, *Science*, **334**, 935 (2011).
2. S. C. Singhal and K. Kendall, *High temperature solid oxide fuel cells: fundamentals, design, and applications*, Elsevier (2003).
3. J. Larminie and A. Dicks, *Fuel Cell Systems Explained* (2nd Edition), in, John Wiley & Sons.
4. E. G. Services, *2004 Fuel Cell Handbook*, U.S. Department of Energy, Office of Fossil Energy, National Energy Technology Laboratory (2004).
5. E. Fabbri, et al., *Materials challenges toward proton-conducting oxide fuel cells: a critical review*, *Chem. Soc. Rev.*, **39**, 4355 (2010).
6. K. D. Kreuer, *Proton-conducting oxides*, *Annu. Rev. Mater. Res.*, **33**, 333 (2003).
7. K. D. Kreuer, *Proton conductivity: materials and applications*, *Chem. Mater.*, **8**, 610 (1996).
8. S. Tao and J. T. Irvine, *A Stable, Easily Sintered Proton-Conducting Oxide Electrolyte for Moderate-Temperature Fuel Cells and Electrolyzers*, *Adv. Mater.*, **18**, 1581 (2006).
9. H. Matsumoto, et al., *Relation between electrical conductivity and chemical stability of BaCeO₃-based proton conductors with different trivalent dopants*, *Electrochem. Solid-State Lett.*, **10**, B77 (2007).
10. K. H. Ryu and S. M. Haile, *Chemical stability and proton conductivity of doped BaCeO₃-BaZrO₃ solid solutions*, *Solid State Ionics*, **125**, 355 (1999).
11. E. D. Wachsman, et al., *Role of solid oxide fuel cells in a balanced energy strategy*, *Energy & Environmental Science* (2012).
12. C. Xia and M. Liu, *Microstructures, conductivities, and electrochemical properties of Ce0.9Gd0.1O₂ and GDC–Ni anodes for low-temperature SOFCs*, *Solid State Ionics*, **152-153**, 423 (2002).
13. P.-C. Su, et al., *Solid Oxide Fuel Cell with Corrugated Thin Film Electrolyte*, *Nano Lett.*, **8**, 2289 (2008).
14. J. S. Ahn, et al., *High-performance bilayered electrolyte intermediate temperature solid oxide fuel cells*, *Electrochim. Commun.*, **11**, 1504 (2009).
15. C. Lu, et al., *Development of intermediate-temperature solid oxide fuel cells for direct utilization of hydrocarbon fuels*, *Solid State Ionics*, **175**, 47 (2004).
16. J. W. Fergus, *Electrolytes for solid oxide fuel cells*, *J. Power Sources*, **162**, 30 (2006).
17. B. C. H. Steele and A. Heinzel, *Materials for fuel-cell technologies*, *Nature*, **414**, 345 (2001).
18. P. I. Cowin, et al., *Recent progress in the development of anode materials for solid oxide fuel cells*, *Advanced Energy Materials*, **1**, 314 (2011).
19. N. Q. Minh, *Ceramic fuel cells*, *J. Am. Ceram. Soc.*, **76**, 563 (1993).
20. W. M. Haynes, et al., *CRC Handbook of Chemistry and Physics*, CRC Press (2012).
21. J. Rossmeisl and W. G. Bessler, *Trends in catalytic activity for SOFC anode materials*, *Solid State Ionics*, **178**, 1694 (2008).

22. A. Faes, et al., *A Review of RedOx Cycling of Solid Oxide Fuel Cells Anode*, *Membranes*, **2**, 585 (2012).
23. S. Tao and J. T. S. Irvine, *A redox-stable efficient anode for solid-oxide fuel cells*, *Nat. Mater.*, **2**, 320 (2003).
24. C. D. Savaniu and J. T. S. Irvine, *La-doped SrTiO₃ as anode material for IT-SOFC*, *Solid State Ionics*, **192**, 491 (2011).
25. E. Lay, et al., *Ce-substituted LSCM as new anode material for SOFC operating in dry methane*, *Solid State Ionics*, **179**, 1562 (2008).
26. S. W. Tao, et al., *Methane oxidation at redox stable fuel cell electrode La0.75Sr0.25Cr0.5Mn0.5O₃-delta*, *J. Phys. Chem. B*, **110**, 21771 (2006).
27. P. Holtappels, et al., *Electrochemical characterization of ceramic SOFC anodes*, *J. Electrochem. Soc.*, **148**, A923 (2001).
28. C. Sun and U. Stimming, *Recent anode advances in solid oxide fuel cells*, *J. Power Sources*, **171**, 247 (2007).
29. M. D. Gross, et al., *Recent progress in SOFC anodes for direct utilization of hydrocarbons*, *J. Mater. Chem.*, **17**, 3071 (2007).
30. T. Klemensø, et al., *Stability of Ni–yttria stabilized zirconia anodes based on Ni-impregnation*, *J. Power Sources*, **195**, 7295 (2010).
31. Advanced Ceramics, in, *Encyclopædia Britannica* (2014).
32. J. Schindelin, et al., *Fiji: an open-source platform for biological-image analysis*, *Nat Meth*, **9**, 676 (2012).
33. J. Goldstein, *Scanning electron microscopy and x-ray microanalysis*, 3rd ed., Springer (2003).
34. W. D. Callister and D. G. Rethwisch, *Materials science and engineering: an introduction*, Wiley New York (2007).
35. J. T. Irvine, et al., *Electroceramics: characterization by impedance spectroscopy*, *Adv. Mater.*, **2**, 132 (1990).
36. H. K. M. David G. Goodwin, and Raymond L. Speth, *Cantera: An object-oriented software toolkit for chemical kinetics, thermodynamics, and transport processes*. , in, Version 2.1.1 ed.
37. G. P. Smith, et al., *GRI-Mech 3.0*, URL: http://www.me.berkeley.edu/gri_mech (1999).
38. W. R. Smith and R. W. Missen, *Chemical reaction equilibrium analysis: theory and algorithms*, Wiley New York (1982).
39. D. R. Gaskell, *Introduction to the Thermodynamics of Materials*, CRC Press (2008).
40. X.-M. Ge, et al., *Solid Oxide Fuel Cell Anode Materials for Direct Hydrocarbon Utilization*, *Advanced Energy Materials*, **2**, 1156 (2012).
41. V. Alzate-Restrepo and J. M. Hill, *Effect of anodic polarization on carbon deposition on Ni/YSZ anodes exposed to methane*, *Applied Catalysis A: General*, **342**, 49 (2008).
42. R. J. Kee, et al., *Solid-oxide fuel cells with hydrocarbon fuels*, *Proceedings of the Combustion Institute*, **30**, 2379 (2005).
43. S. McIntosh and R. J. Gorte, *Direct Hydrocarbon Solid Oxide Fuel Cells*, *Chem. Rev.*, **104**, 4845 (2004).

44. R. J. Gorte and J. M. Vohs, *Catalysis in Solid Oxide Fuel Cells*, *Annual Review of Chemical and Biomolecular Engineering*, **2**, 9 (2011).
45. A. Atkinson, et al., *Advanced anodes for high-temperature fuel cells*, *Nat. Mater.*, **3**, 17 (2004).
46. C. H. Bartholomew, *Carbon Deposition in Steam Reforming and Methanation*, *Catal. Rev.*, **24**, 67 (1982).
47. W. Y. Lee, et al., *On the Predictions of Carbon Deposition on the Nickel Anode of a SOFC and Its Impact on Open-Circuit Conditions*, *J. Electrochem. Soc.*, **160**, F94 (2013).
48. O. Demircan, *Electrochemica Oxidation Kinetics of Hydrogen and Higher Hydrocarbons on Solid Oxide Fuel Cells*, in *Department of Chemistry and Biochemistry*, University of Maryland, College Park, MD (2007).
49. A. M. Sukeshini, et al., *Electrochemical Oxidation of H₂, CO, and CO/H₂ Mixtures on Patterned Ni Anodes on YSZ Electrolytes*, *J. Electrochem. Soc.*, **153**, A705 (2006).
50. M. Cimenti and J. Hill, *Direct Utilization of Liquid Fuels in SOFC for Portable Applications: Challenges for the Selection of Alternative Anodes*, *Energies*, **2**, 377 (2009).
51. Y. Lin, et al., *Direct operation of solid oxide fuel cells with methane fuel*, *Solid State Ionics*, **176**, 1827 (2005).
52. A. Bieberle, et al., *The electrochemistry of Ni pattern anodes used as solid oxide fuel cell model electrodes*, *J. Electrochem. Soc.*, **148**, A646 (2001).
53. A. Bieberle and L. Gauckler, *Reaction mechanism of Ni pattern anodes for solid oxide fuel cells*, *Solid State Ionics*, **135**, 337 (2000).
54. J. Mizusaki, et al., *Kinetic studies of the reaction at the nickel pattern electrode on YSZ in H₂-H₂O atmospheres*, *Solid State Ionics*, **70**, 52 (1994).
55. K. Taek Lee, et al., *Bimodally integrated anode functional layer for lower temperature solid oxide fuel cells*, *J. Mater. Chem.*, **22**, 17113 (2012).
56. K. T. Lee, et al., *Comprehensive quantification of Ni-Gd_{0.1}Ce_{0.9}O_{1.95} anode functional layer microstructures by three-dimensional reconstruction using a FIB/SEM dual beam system*, *J. Power Sources*, **228**, 220 (2013).
57. K. T. Lee, et al., *Feasibility of low temperature solid oxide fuel cells operating on reformed hydrocarbon fuels*, *J. Mater. Chem.*, **22**, 22405 (2012).
58. C. M. Gore, et al., *Effect of composition and microstructure on electrical properties and CO₂ stability of donor-doped, proton conducting BaCe_{1-(x+y)}ZrxNb_yO₃*, *J. Mater. Chem. A*, **2**, 2363 (2014).
59. C. M. Gore, et al., *Porous GDC Scaffold Anodes for Lower Temperature, Hydrocarbon-Fueled Solid Oxide Fuel Cells*, *ECS Trans.*, **50**, 53 (2013).
60. C. M. Gore, et al., *Effect of Composition and Atmosphere on Electrical Properties of Donor-doped BaCe_{1-(x+y)}ZrxNb_yO₃*, *ECS Trans.*, **58**, 147 (2013).
61. H. T. Kalmus and C. Harper, *Physical Properties of the Metal Cobalt*, *Journal of Industrial & Engineering Chemistry*, **7**, 6 (1915).
62. X. F. Fan, et al., *Room temperature elastic properties of gadolinia-doped ceria as a function of porosity*, *Ceram. Int.*, **39**, 6877 (2013).

63. A. Nakajo, et al., *Compilation of mechanical properties for the structural analysis of solid oxide fuel cell stacks. Constitutive materials of anode-supported cells*, *Ceram. Int.*, **38**, 3907 (2012).
64. Y. Wang, et al., *The effect of oxygen vacancy concentration on the elastic modulus of fluorite-structured oxides*, *Solid State Ionics*, **178**, 53 (2007).
65. R. Clemmer and S. Corbin, *Influence of porous composite microstructure on the processing and properties of solid oxide fuel cell anodes*, *Solid State Ionics*, **166**, 251 (2004).
66. A. Atkinson and A. Selçuk, *Mechanical behaviour of ceramic oxygen ion-conducting membranes*, *Solid State Ionics*, **134**, 59 (2000).
67. S. F. Corbin, et al., *Influence of Green Formulation and Pyrolyzable Particulates on the Porous Microstructure and Sintering Characteristics of Tape Cast Ceramics*, *J. Am. Ceram. Soc.*, **84**, 41 (2001).
68. M. W. Barsoum, *Fundamentals of ceramics*, CRC Press (2002).
69. A. A. Hassan, et al., *Effect of CuO addition on the sintering behavior and electrical conductivity of 3Y-TZP*, *J. Mater. Sci. Technol.*, **23**, 131 (2007).
70. R. E. Mistler and E. R. Twiname, *Tape casting: theory and practice*, American Ceramic Society (2000).
71. C. V. Thompson, *Solid-State Dewetting of Thin Films*, *Annu. Rev. Mater. Res.*, **42**, 399 (2012).
72. T. A. Roth, *The surface and grain boundary energies of iron, cobalt and nickel*, *Materials Science and Engineering*, **18**, 183 (1975).
73. P. A. Dowben and A. Miller, *Surface Segregation Phenomena*, CRC Press (1990).
74. N. Baumann, et al., *Porous model type electrodes by induced dewetting of thin Pt films on YSZ substrates*, *Solid State Ionics*, **181**, 7 (2010).
75. D. Yoon and A. Manthiram, *Hydrocarbon-fueled solid oxide fuel cells with surface-modified, hydroxylated Sn/Ni-Ce0.8Gd0.2O1.9 heterogeneous catalyst anode*, *J. Mater. Chem. A* (2014).
76. L. Ortega-San-Martín, et al., *Redox behaviour and ageing of GDC-Co cermets: A comparison between lamellar and conventional cermets*, *Solid State Ionics*, **226**, 30 (2012).
77. M. Andersson, et al., *Review of catalyst materials and catalytic steam reforming reactions in SOFC anodes*, *International Journal of Energy Research*, **35**, 1340 (2011).
78. E. D. Wachsman, et al., *Role of solid oxide fuel cells in a balanced energy strategy*, *Energy & Environmental Science*, **5**, 5498 (2012).
79. A. Choudhury, et al., *Application of solid oxide fuel cell technology for power generation—A review*, *Renewable and Sustainable Energy Reviews*, **20**, 430 (2013).
80. W. Wang, et al., *Progress in Solid Oxide Fuel Cells with Nickel-Based Anodes Operating on Methane and Related Fuels*, *Chem. Rev.*, **113**, 8104 (2013).
81. Y. B. Kim, et al., *Surface-Modified Low-Temperature Solid Oxide Fuel Cell*, *Adv. Funct. Mater.*, **21**, 4684 (2011).
82. E. Fabbri, et al., *Towards the Next Generation of Solid Oxide Fuel Cells Operating Below 600 °C with Chemically Stable Proton-Conducting Electrolytes*, *Adv. Mater.*, **24**, 195 (2012).
83. X. Meng, et al., *Low-temperature ceria-electrolyte solid oxide fuel cells for efficient methanol oxidation*, *J. Power Sources*, **196**, 9961 (2011).

84. H. H. Shin and S. McIntosh, *Insights into Hydrogen Oxidation on SOFC Anode Materials by Isotopic Exchange*, *ECS Electrochemistry Letters*, **2**, F88 (2013).
85. T. Takeguchi, et al., *Hydrogen Spillover from NiO to the Large Surface Area CeO₂-ZrO₂ Solid Solutions and Activity of the NiO/CeO₂-ZrO₂ Catalysts for Partial Oxidation of Methane*, *J. Catal.*, **202**, 14 (2001).
86. A. Trovarelli and P. Fornasiero, *Catalysis by ceria and related materials*, World Scientific (2013).
87. D. L. Trimm, *Coke formation and minimisation during steam reforming reactions*, *Catal. Today*, **37**, 233 (1997).
88. Z. Fu, et al., *Importance of oxygen spillover for fuel oxidation on Ni/YSZ anodes in solid oxide fuel cells*, *Phys. Chem. Chem. Phys.*, **16**, 8536 (2014).
89. R. J. Gorte, et al., *Anodes for Direct Oxidation of Dry Hydrocarbons in a Solid-Oxide Fuel Cell*, *Adv. Mater.*, **12**, 1465 (2000).
90. R. J. Gorte and J. M. Vohs, *Nanostructured anodes for solid oxide fuel cells*, *Current Opinion in Colloid & Interface Science*, **14**, 236 (2009).
91. W. C. Chueh, et al., *High electrochemical activity of the oxide phase in model ceria-Pt and ceria-Ni composite anodes*, *Nat. Mater.*, **11**, 155 (2012).
92. A. Trovarelli, *Catalytic properties of ceria and CeO₂-containing materials*, *Catal. Rev.*, **38**, 439 (1996).
93. O. A. Marina, et al., *A solid oxide fuel cell with a gadolinia-doped ceria anode: preparation and performance*, *Solid State Ionics*, **123**, 199 (1999).
94. S. He, et al., *Preparation and characterization of Cu-SDC anodes for low-temperature solid oxide fuel cell*, *J. Alloys Compd.* (2013).
95. Y. Lin, et al., *A new symmetric solid oxide fuel cell with a samaria-doped ceria framework and a silver-infiltrated electrocatalyst*, *J. Power Sources*, **197**, 57 (2012).
96. M. Lomberg, et al., *Characterization of Ni-Infiltrated GDC Electrodes for Solid Oxide Cell Applications*, *J. Electrochem. Soc.*, **161**, F899 (2014).
97. Z. Zhan and S. A. Barnett, *Use of a catalyst layer for propane partial oxidation in solid oxide fuel cells*, *Solid State Ionics*, **176**, 871 (2005).
98. K. Sugihara, et al., *A quantitative analysis of influence of Ni particle size of SDC-supported anode on SOFC performance: Effect of particle size of SDC support*, *Solid State Ionics*, **262**, 433 (2014).
99. W. Zhu, et al., *Enhancement in Three-Phase Boundary of SOFC Electrodes by an Ion Impregnation Method: A Modeling Comparison*, *Electrochim. Solid-State Lett.*, **11**, B83 (2008).
100. P. Costamagna, et al., *Micro-modelling of solid oxide fuel cell electrodes*, *Electrochim. Acta*, **43**, 375 (1998).
101. M. Kishimoto, et al., *Enhanced triple-phase boundary density in infiltrated electrodes for solid oxide fuel cells demonstrated by high-resolution tomography*, *J. Power Sources*, **266**, 291 (2014).
102. G. Brus, et al., *Tortuosity of an SOFC anode estimated from saturation currents and a mass transport model in comparison with a real micro-structure*, *Solid State Ionics*, **265**, 13 (2014).
103. P. R. Shearing, et al., *X-ray nano computerised tomography of SOFC electrodes using a focused ion beam sample-preparation technique*, *J. Eur. Ceram. Soc.*, **30**, 1809 (2010).

104. J. R. Izzo, et al., *Nondestructive Reconstruction and Analysis of SOFC Anodes Using X-ray Computed Tomography at Sub-50 nm Resolution*, *J. Electrochem. Soc.*, **155**, B504 (2008).
105. G. Horvai, *Relationship between charge transfer resistance and exchange current density of ion transfer at the interface of two immiscible electrolyte solutions*, *Electroanalysis*, **3**, 673 (1991).
106. A. V. Virkar, et al., *The role of electrode microstructure on activation and concentration polarizations in solid oxide fuel cells*, *Solid State Ionics*, **131**, 189 (2000).
107. M. Ni, et al., *Parametric study of solid oxide fuel cell performance*, *Energy Convers. Manage.*, **48**, 1525 (2007).
108. D. Ding, et al., *An octane-fueled low temperature solid oxide fuel cell with Ru-free anodes*, *Electrochim. Commun.*, **10**, 1295 (2008).
109. H. Iwahara, *Proton conductors : solids, membranes, and gels--materials and devices*, Cambridge University Press, Cambridge; New York (1992).
110. E. Fabbri, et al., *High-performance composite cathodes with tailored mixed conductivity for intermediate temperature solid oxide fuel cells using proton conducting electrolytes*, *Energy & Environmental Science*, **4**, 4984 (2011).
111. D. Pergolesi, et al., *High proton conduction in grain-boundary-free yttrium-doped barium zirconate films grown by pulsed laser deposition*, *Nat. Mater.*, **9**, 846 (2010).
112. T. K. Oh, et al., *Effect of Eu dopant concentration in SrCe $1-x$ Eu x O $3-\delta$ on ambipolar conductivity*, *Solid State Ionics*, **180**, 1233 (2009).
113. J. Li, et al., *High temperature SrCe 0.9 Eu 0.1 O $3-\delta$ proton conducting membrane reactor for H₂ production using the water–gas shift reaction*, *Applied Catalysis B: Environmental*, **92**, 234 (2009).
114. T. Oh, et al., *Hydrogen permeation through thin supported SrZr 0.2 Ce $0.8-x$ Eu x O $3-\delta$ membranes*, *J. Membr. Sci.*, **345**, 1 (2009).
115. J. Li, et al., *SrCe 0.7 Zr 0.2 Eu 0.1 O 3 -based hydrogen transport water gas shift reactor*, *Int. J. Hydrogen Energy*, **37**, 16006 (2012).
116. K. D. Kreuer, *Aspects of the formation and mobility of protonic charge carriers and the stability of perovskite-type oxides*, *Solid State Ionics*, **125**, 285 (1999).
117. Q. Li, et al., *Approaches and recent development of polymer electrolyte membranes for fuel cells operating above 100 C*, *Chem. Mater.*, **15**, 4896 (2003).
118. R. Kannan, et al., *BaCe $0.85-x$ Zr x Sm 0.15 O $3-\delta$ ($0.01 < x < 0.3$) (BCZS): Effect of Zr Content in BCZS on Chemical Stability in CO₂ and H₂O Vapor, and Proton Conductivity*, *J. Electrochem. Soc.*, **160**, F18 (2013).
119. M. Talimi and V. Thangadurai, *Electrical conductivity and chemical stability of perovskite-type BaCe $0.8-x$ Ti x Y 0.2 O $3-\delta$* , *Ionics*, **17**, 195 (2011).
120. F. Trobec and V. Thangadurai, *Transformation of Proton-Conducting Perovskite-Type into Fluorite-Type Fast Oxide Ion Electrolytes Using a CO₂ Capture Technique and Their Electrical Properties*, *Inorg. Chem.*, **47**, 8972 (2008).
121. E. Fabbri, et al., *Tailoring the chemical stability of Ba (Ce 0.8– x Zr x) Y 0.2 O 3– δ protonic conductors for intermediate temperature solid oxide fuel cells (IT-SOFCs)*, *Solid State Ionics*, **179**, 558 (2008).
122. N. Zakowsky, et al., *Elaboration of CO₂ tolerance limits of BaCe 0.9 Y 0.1 O $3-\delta$ electrolytes for fuel cells and other applications*, *Solid State Ionics*, **176**, 3019 (2005).

123. S. S. Bhella, et al., *Synthesis, Structure, Chemical Stability, and Electrical Properties of Nb-, Zr-, and Nb-Codoped BaCeO₃ Perovskites*, *Inorg. Chem.*, **50**, 6493 (2011).
124. J. Dauter, et al., *Studies on Chemical Stability and Electrical Properties of Proton Conducting Perovskite-Like Doped BaCeO₃*, *J. Electrochem. Soc.*, **157**, B1413 (2010).
125. Z. M. Zhong, *Stability and conductivity study of the BaCe_{0.9-x}Zr_xY_{0.1}O_{2.95} systems*, *Solid State Ionics*, **178**, 213 (2007).
126. S. V. Bhide and A. V. Virkar, *Stability of BaCeO₃-Based Proton Conductors in Water-Containing Atmospheres*, *J. Electrochem. Soc.*, **146**, 2038 (1999).
127. C. W. Tanner and A. V. Virkar, *Instability of BaCeO₃ in H₂O-Containing Atmospheres*, *J. Electrochem. Soc.*, **143**, 1386 (1996).
128. K. Katahira, et al., *Protonic conduction in Zr-substituted BaCeO₃*, *Solid State Ionics*, **138**, 91 (2000).
129. A. J. Jacobson, et al., *The structures of BaCeO₃, BaPrO₃ and BaTbO₃ by neutron diffraction: lattice parameter relations and ionic radii in O-perovskites*, *Acta Crystallographica Section B: Structural Crystallography and Crystal Chemistry*, **28**, 956 (1972).
130. Q. Li and V. Thangadurai, *Synthesis, Structure and Electrical Properties of Mo-doped CeO₂-Materials for SOFCs, Fuel Cells*, **9**, 684 (2009).
131. Q. Li and V. Thangadurai, *A comparative 2 and 4-probe DC and 2-probe AC electrical conductivity of novel co-doped Ce_{0.9-x}RE_xMo_{0.1}O_{2.1-0.5x} (RE= Y, Sm, Gd; x= 0.2, 0.3)*, *J. Mater. Chem.*, **20**, 7970 (2010).
132. P. Hjalmarsson, et al., *Electrochemical behaviour of (La_{1-x}Sr_x)_sCo_{1-y}Ni_yO_{3-δ} as porous SOFC cathodes*, *Solid State Ionics*, **180**, 1395 (2009).
133. E. Chinarro, et al., *Bulk and grain boundary conductivity of Ca_{0.97}Ti_{1-x}FexO_{3-δ} materials*, *Solid State Ionics*, **160**, 161 (2003).
134. R. D. Shannon, *Revised effective ionic radii and systematic studies of interatomic distances in halides and chalcogenides*, *Acta Crystallographica Section A: Crystal Physics, Diffraction, Theoretical and General Crystallography*, **32**, 751 (1976).
135. M. Cherry, et al., *Oxygen Ion Migration in Perovskite-Type Oxides*, *J. Solid State Chem.*, **118**, 125 (1995).
136. S. M. Haile, et al., *The role of microstructure and processing on the proton conducting properties of gadolinium-doped barium cerate*, *J. Mater. Res.*, **13**, 1576 (1998).
137. A. F. Barton, *CRC handbook of polymer-liquid interaction parameter s and solubility parameters*, CRC press (1990).
138. C. D. Wagner and G. E. Muilenberg, *Handbook of x-ray photoelectron spectroscopy: a reference book of standard data for use in x-ray photoelectron spectroscopy*, Physical Electronics Division, Perkin-Elmer Corp. (1979).
139. W. C. Chueh, et al., *Highly Enhanced Concentration and Stability of Reactive Ce³⁺ on Doped CeO₂ Surface Revealed In Operando*, *Chem. Mater.*, **24**, 1876 (2012).
140. D. R. Mullins, et al., *Electron spectroscopy of single crystal and polycrystalline cerium oxide surfaces*, *Surf. Sci.*, **409**, 307 (1998).